Instrumentation for Molecular Electronics Device Research

by

Ashley Ann Kibel

A Dissertation Presented in Partial Fulfillment
of the Requirements for the Degree
Doctor of Philosophy

Approved November 2010 by the
Graduate Supervisory Committee:

Stuart Lindsay, Chair
Ralph Chamberlin
Thomas Moore
Sefika Ozkan
Otto Sankey

ARIZONA STATE UNIVERSITY

December 2010

ABSTRACT

This dissertation describes work on three projects concerning the design and implementation of instrumentation used to study potential organic electronic devices. The first section describes the conducting atomic force microscope (CAFM) in the study of the mechanical and electronic interactions between DNA bases and nucleosides. Previous STM data suggested that an STM tip could recognize single base pairs through an electronic interaction after a functionalized tip made contact with a self assembled monolayer then was retracted. The conducting AFM was employed in order to understand the mechanical interactions of such a system and how they were affecting electrical responses. The results from the conducting AFM showed that the scanning probe system was measuring multiple base-pair interactions, and thus did not have single base resolution. Further, results showed that the conductance between a single base-nucleoside pair is below the detection limit of a potential commercial sequencing device.

The second section describes the modifications of a scanning probe microscope in order to study the conductance of single organic molecules under illumination. Modifications to the scanning probe microscope are described as are the control and data analysis software for an experiment testing the single molecule conductance of an organic molecule under illumination. This instrument was then tested using a novel charge-separation molecule, which is being considered for its potential photovoltaic properties. The experiments

showed that the instrumentation is capable of detecting differences in conductance upon laser illumination of the molecule on a transparent conductive surface.

The third section describes measurements using the illuminated CAFM, as well as the design and construction of an illuminated mercury drop electrode apparatus. Both instruments were tested by attempting to observe photovoltaic behavior in a novel self-organized film of the charge-separation molecules mentioned in the previous paragraph. Results and calculations show that the conducting AFM is not a useful tool in the examination of these organic photovoltaics, while the mercury drop apparatus measured photovoltaic effects in the film. Although photovoltaic effects were measurable with the mercury drop electrode, it was found that the film exhibited very low photon-to-electron conversion efficiency (IPCE).

For my parents, Daniel and Kathleen,

and my husband, Jonathan

ACKNOWLEDGEMENTS

I must thank all those that have helped me over the years. In particular, I wish to thank my fellow graduate students, Shreya Bhattacharyya and James Bridgewater, who have been especially helpful with the organic photovoltaic parts of this project. Dr. Tomoyuki Morita taught me how to use the atomic force microscope and Dr. Iris Visoly-Fisher was a great lab teacher and mentor. Professor Devens Gust was always willing to sit down and discuss any challenges or results and Dr. Paul Lidell provided the molecules that were essential for my work. Finally, I must thank my advisor Stuart Lindsay. I was financially supported by the NSF IGERT program and an NSF NIRT grant.

TABLE OF CONTENTS

Page

CHAPTER Page

CHAPTER Page

CHAPTER Page

LIST OF TABLES

LIST OF FIGURES

Figure Page

Figure Page

1. INTRODUCTION

This chapter first describes the instrumentation utilized in molecular electronic research. Specifically, it examines the two main types of scanning probe microscopes, scanning tunneling and atomic force, and quickly reviews the use of mercury drop instrumentation. The second part of the chapter describes the theory of molecular electronics and experimental techniques used to measure the electronic properties of organic molecules.

1.1. Instrumentation utilized in molecular electronic research

Instrumentation is a key component in the ability to experimentally understand the electronic properties of organic molecules. The three main types of instrumentation that will be described in this dissertation are scanning tunneling microscopy, atomic force microscopy and mercury drop electrodes. Scanning tunneling microscopy and atomic force microscopy are both considered forms of scanning probe microscopy. Scanning probe microscopy, in particular, has paved the way for much of the experimental investigation into molecular electronics.

Part of the increased interest in the field of nanoscience and nanotechnology in the recent decade has been spurred on by the ability to image and interact with structures at the nanoscale. Scanning probe microscopy (SPM) has become a highly employed method to image and interact with nanoscale materials. The field of SPM has grown over the last 3 decades since the invention of the scanning tunneling microscope, and the applicability and versatility of these

machines has been greatly enhanced. The ability to simultaneously probe and image a sample with the same piece of equipment, in particular, has allowed many breakthroughs spanning a wide range of fields within nanoscience.

In terms of imaging capabilities, scanning probe microscopy is unique to other forms of microscopy in that a sharp probe interacts with the surface being imaged. The mechanism of interaction is different depending upon the type of microscopy and the imaging mode, but the generated signal is almost always highly correlated to features in the topography. This interaction produces a measurable signal that, again, is typically related to topographical features. While imaging, this probe is continuously modulated in order to keep this signal constant, and the degree of modulation of the probe can be recorded and, effectively, maps out the surface. The type of signal that is produced from the interaction between the probe and the surface determines what type of surfaces can be imaged and what the features in the image actually represent. The two major categories of scanning probe microscopy are scanning tunneling microscopy, which utilizes a tunneling current signal between probe and conductive surface, and atomic force microscopy, which utilizes the bending of a flexible cantilever as a surface sensor.

1.1.1. Scanning tunneling microscopy

The scanning tunneling microscope (STM) was invented in 1981 by Binnig and Rohrer, who won the Nobel prize for the invention in 1986.[1] The STM works by incorporating a very sharp metallic probe, which, ideally, has a

single atom at its point. This tip is then approached to a conductive surface until a predetermined tunneling current (typically in the nanoampere range) is achieved. On a bare metallic surface, like bare gold, this tunneling current can typically be achieved without hard contact with the surface. As is known from quantum mechanics, the wavefunction for a particle to tunnel through a one dimensional potential barrier is $\psi(x) = A\exp(-\sqrt{\frac{2m(V-E)}{\hbar^2}}x)$, where E is the energy of the particle and V is the potential of the barrier. Squaring this to get the probability of finding a particle at any given location in the one dimensional problem gives $\psi(x)^2 = A^2\exp(-2\sqrt{\frac{2m(V-E)}{\hbar^2}}x)$, meaning that the probability of finding the particle a distance x through a potential barrier falls off exponentially with x. While these formulas do not as accurately reflect the more complicated situation of an STM tip with electrons tunneling through a vacuum gap, it is clear to see the implications. As the tip is moved closer or further away from the surface, the current will drop off or increase exponentially. Adjusting the height of the STM probe to keep this current constant while scanning across a surface and accurately measuring the movement of the tip in response to these adjustments allows for very high resolution imaging of topography.

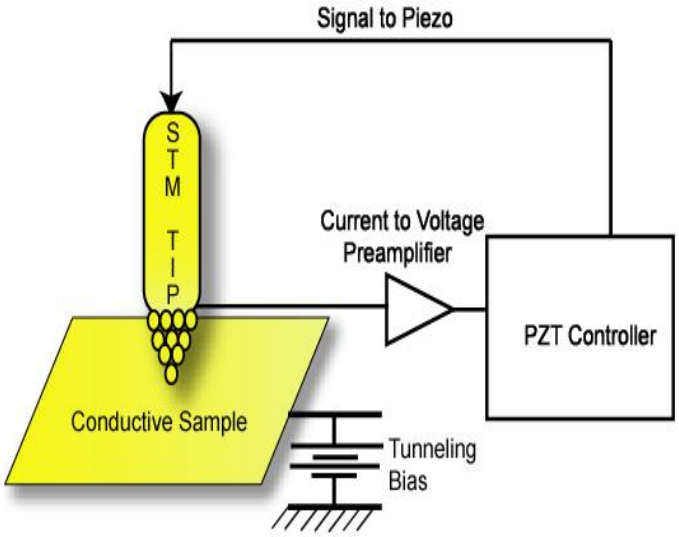

Figure 1.1 Schematic of typical STM operation. Tunneling current is connected to a current to voltage preamplifier, and this voltage is used to control distance between the tip and the sample

The actual instrumentation for the typical STM measurement is fairly simple (see Figure 1.1). An STM scanner allows for the insertion of a metal wire tip that has typically been electrochemically etched to be very sharp.[2,3] Electrically attached to this tip is a current to voltage preamplifier that converts nanoampere currents into more easily measurable and transferable voltages. This conversion can be obtained by simply connecting the tip to a operational amplifier (op-amp). The current lead from the tip is connected to the inverting input of the amplifier (see Figure 1.2). Since the other op-amp input is grounded, the inverting input also remains at zero potential, and thus the tip is grounded. Since no current flows through an ideal op-amp, the tunneling current runs through the

resistor connecting the inverting input to the output voltage. Using Ohm's law,

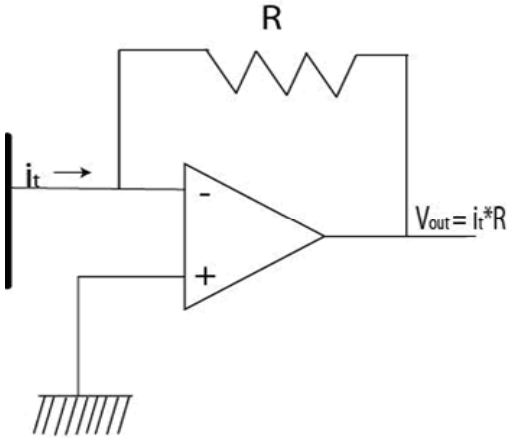

Figure 1.2. Schematic of current to voltage converter. Tunneling current is wired into the inverting input of an operational amplifier. Resulting voltage output is proportional to the tunneling current.

then, $i_{tunneling} = \frac{V_{out} - V_{in}}{R_1}$, but since V_{in} is grounded, this simplifies to $i_{tunneling} = \frac{V_{out}}{R_1}$, or $V_{out} = i_{tunneling} \cdot R_1$, meaning that the output voltage is proportional to the tunneling current. Typical preamplifiers range from 0.1 nA/V to 100 nA/V, and, in many scanners, are interchangeable depending upon the desired current range.

The tip is also in mechanical contact with an element that can control the height of the tip, and, typically, its x and y positions as well. This element has piezoelectric properties, which means that voltages applied to it translates in a reliable way to changes in the elements' dimensions. In almost all SPM scanners this element is made from lead zirconium titanate (PZT).[4] Typical PZT elements in an STM scanner are made into tube shapes with electrodes both inside and outside the tube (see Figure 1.3). The inside electrode is typically grounded so that changing the voltages on all the outer electrodes to a particular voltage causes the tube wall to either become thinner or thicker depending upon the sign of the applied voltage. This, in turn, causes the length of the tube to either grow or

contract, since the volume of the tube remains constant. Applying different voltages on the coupled sets of electrodes around the outside of the tube can cause the tube to bend in the x and y axes, allowing for motion in the x and y directions.

Typically, samples are manually positioned near the tip by the user and are then automatically approached closer through the use of stepper motors. Once the setpoint has been reached, the tunnel junction is kept stable by modulating the z axis of the piezo using a controller. To image a sample, either the tip can be raster scanned with the piezo to which it is attached while controlling tip height with the same piezo, or the sample can be raster scanned on a piezo stage while the height of the tip adjusts. The voltage that gets applied to the piezo then gets fed into whatever control software is being used, and converted into a topographical image by knowing the calibration values that convert voltage to distance on the piezo.

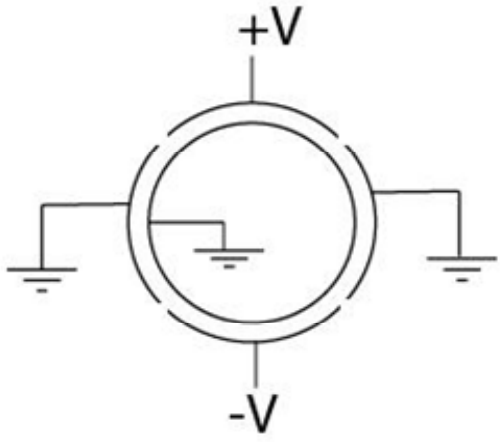

Figure 1.3. Top down schematic of PZT tube scanner.

One particular drawback to imaging with an STM is its inability to definitively distinguish electrical information from topographical information. All samples used with the STM must be somewhat conductive in order for a

tunnel junction to be maintained. For samples of highly homogenous conductivity on the nanoscale, the use of tunnel current as a determination of topography proves very accurate. In samples of heterogeneous conductivity, however, the distinction between a topographical feature and a feature of high or low conductivity becomes difficult to ascertain. The lack of ability to image non-conductive samples and the difficulty in analyzing images of heterogeneous conductivity have been major driving forces in the increased popularity of using the atomic force microscope.

1.1.2. Atomic force microscopy

As another form of scanning probe microscopy, the atomic force microscopy (AFM), (invented soon after the STM in 1986 by Binnig, Quate and Gerber)[5] shares many similar attributes with the scanning tunneling microscope. Unlike the STM, however, the AFM utilizes a flexible cantilever with a very sharp tip attached to it in order to probe and image surfaces. The interaction between the probe and the surface in AFM is not tunnel current like the STM, but, as the name implies, forces of attraction or repulsion between the two. This force is sensed by the bending of the cantilever, which is monitored by reflecting a laser off of the backside of the cantilever and recording the position on a photodiode detector. Any surface can interact with this cantilever, and this means that AFM measurements are not strictly limited to conductive samples.

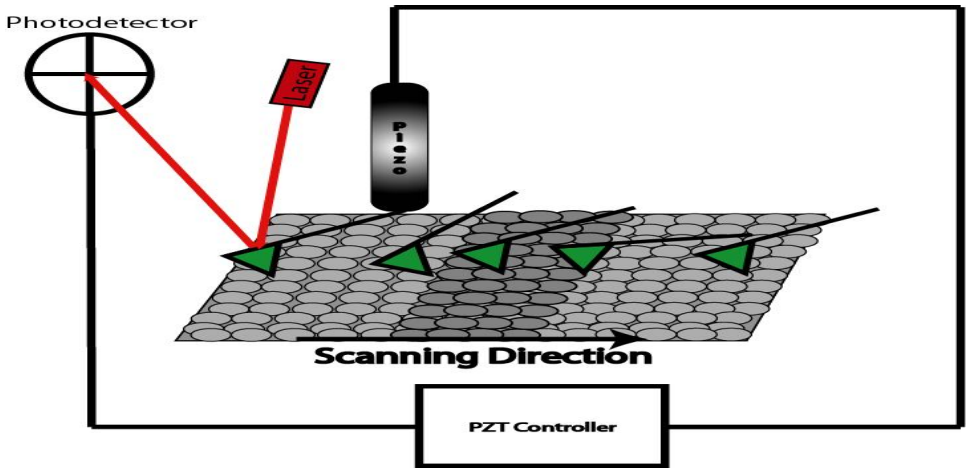

Figure 1.4. Schematic diagram of contact mode AFM. The bending of the cantilever is detected by a laser bounced of its back. This signal is recorded and then utilized in a feedback loop to control the contact force between the tip and the surface

One of the most basic AFM imaging modes is known as contact mode (see Figure 1.4). In this mode, an AFM tip/cantilever is approached to the surface until the cantilever registers a certain force, determined by a specific amount of bending of the cantilever upon contact. The cantilevers have an intrinsic spring constant, so bending of the cantilever directly converts into a force of contact. As discussed above, this bending is measured by recording the displacement of a laser beam bounced off of the back of the cantilever. This force/bending is then kept constant as the tip is scanned across the surface. When the tip hits a high or low feature on the surface, the instantaneous force between the tip and sample changes and is quickly corrected by applying a voltage to the piezo in mechanical contact with the cantilever which either lowers or raises the force to a value determined by the user. Thus, while mapping the surface, the force is kept constant.

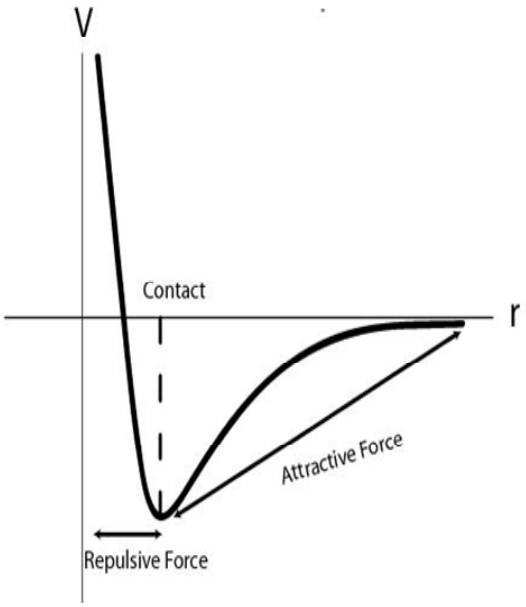

Figure 1.5. Graph of the Lennard-Jones potential.

Although it is a common imaging mode, Atomic force microscopy is not limited to contact mode operation. Interaction forces between tip and surface actual change considerably as the tip is approached to the surface. Figure 1.5 shows the interaction potential between the tip and the surface. The potential curve is a graphical representation of the Lennard-Jones potential, $V(r) = 4\varepsilon\left[\left(\frac{\sigma}{r}\right)^{12} - \left(\frac{\sigma}{r}\right)^{6}\right]$. As the tip gets closer to the surface, the 12^{th} power of the term, the repulsive term, dominates, but further away from the surface the attractive power to the 6^{th} term remains. The two different regimes give rise to the two types of dynamic force microscopy which are very popular for imaging in AFM.

In dynamic force microscopy, the tip is not simply approached to the surface until it hits with a certain force as in contact mode AFM. The most common form of dynamic force microscopy is referred to as amplitude

modulation atomic force microscopy (AM-AFM). Unlike in contact mode, the tip is vibrated at a frequency close to its resonance. The surface is then approached to the tip. As the distance between the tip and the sample decreases, the amplitude of the cantilever vibration will decrease as it interacts with the surface. Once the amplitude reaches a setpoint, it is held constant as the tip is scanned across the surface. The two main types of dynamic force microscopy are intermittent contact mode and noncontact mode. In intermittent contact, the cantilever operates in both the repulsive and attractive potential regimes, and as it vibrates and scans across a surface, it taps down, making contact with the atoms on the surface. For this reason, intermittent contact mode is oftentimes referred to as "tapping" mode. Intermittent contact is achieved by vibrating a tip just below the resonant frequency. Once the tip begins to tap down onto the surface, the amplitude of the vibration is reduced, and is held constant by the servo system. Changes in force are detected by changes in the amplitude, and the tip is pulled away from or towards the surface to maintain constant amplitude.

In AM-AFM non-contact mode, used mainly for biological and other softer samples, the cantilever operates in the attractive potential regime, achieved by vibrating the tip just above the resonant frequency. Upon approach to the surface, the amplitude of the tip vibration lowers due to the interaction with the attractive potential, but it does not make physical contact as it would in tapping mode. Typically this non-contact mode is used to image soft samples, such as biological materials, in liquids. Although this can be accomplished by utilizing

the vibrating piezo usually used in tapping mode, this piezo has difficulty vibrating the tip properly in a damped liquid environment. Furthermore, the piezo vibrates more than just the cantilever and can cause acoustic effects in the surrounding solution which can distort images. For this reason, many utilize a magnetic cantilever and an oscillating magnetic field either above or below the tip in order to oscillate just the cantilever and minimize interference. This is referred to as magnetic AC mode imaging, or MAC mode, and its use has led to high quality imaging and measurements of soft samples.[6-8]

Although not used as frequently, frequency modulation AFM (FM-AFM) has been shown to improve upon the bandwidth of dynamic force AFM. In amplitude modulation, a change in the force felt by the cantilever is followed by a shift in the amplitude of the cantilever oscillation. This shift in amplitude, however, is time dependent and is strongly correlated to the Q-factor of the particular cantilever. This amplitude change can be represented by

$$A^2(t) = A_0{}^2 + A_t{}^2 e^{-\omega_0 t/Q} + 2A_0 A_t e^{-\omega_0 t/2Q} \cos\left[(\omega_t - \omega_d)t + (\vartheta_t - \vartheta_0)\right] \qquad 1.1$$

Where A_0 is the new steady state amplitude after the change in force, ω_0 is the new resonant frequency of the cantilever, ω_t is the frequency of free oscillation, ω_d is the driving frequency, and θ_0 is the new phase.[9] θ_t and A_t are boundary condition fitting parameters. One can achieve a faster response time by lowering the Q factor of the cantilever. However, lowering the Q of the cantilever, lowers the sensitivity of the device in amplitude modulation. In FM-AFM, the tip is pulled up and down based upon shifts detected in frequency, instead of amplitude.

In this case, a high Q factor does not increase the response time of the system, but will increase the sensitive. For this reason FM-AFM can offer very high resolution imaging at faster scanning speeds.[9]

Although not originally designed to measure electrical properties of samples, changes to the typical instrumentation allow for various electrical measurements to be performed using the AFM. Conducting AFM, for instance, can be performed by coating the tip and cantilever with a conductive substance such as gold or platinum. A voltage applied to the sample and a current to voltage preamplifier in the scanning head allow for measurements of nanoscale currents performed without largely affecting the control of interaction forces. Although the STM can provide similar information, the separation of the conduction signal from the force modulation can provide the needed distinction between conductivity and topography that gets muddled when one images with the STM.

Figure 1.6 illustrates the usefulness of this separation. The image is of bare, clean fluorine doped tin oxide surface measured in a non-conductive solvent. The left image is the topography image, determined by scanning the tip across the image in contact mode, maintaining a constant force. The tip was coated with platinum and a bias was applied to the surface. The image on the right is the current flowing through the tip/sample junction as the scanning occurs. Both images were taken at the same time. It is clear from the images that certain features in the topography are not conductive, while others show a high amount of conductivity. In this way, nanoscale topography can be directly correlated with

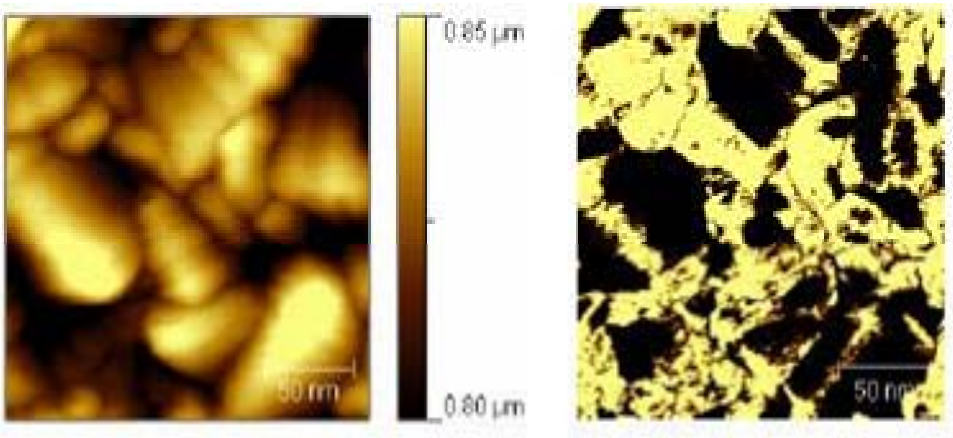

Figure 1.6. Conducting AFM images of fluorine doped tin oxide. The left image shows the topography of the surface and the image on the right shows the simultaneously acquired nanoscale conductance map. The area is the same for both images.

the nanoscale electronic properties of the material. This is a function lacking in the STM.

With conductive AFM probes and more complex instrumentation, more sophisticated electronic AFM measurements can be performed. One measurement mode that is gaining in popularity is Kelvin force microscopy (KFM) which allows for nanoscale surface potential measurements. This measurement is typically performed in tapping mode. In KFM an oscillating bias is applied to the tip at a different frequency than the frequency at which the tip is vibrated along with a servo controlled DC bias. If a surface potential exists, it will cause the tip to oscillate at the amplitude of the AC bias due to changes in electric fields produced between the tip and the sample. The amplitude of this oscillation is typically very small and needs to be measured with a separate lock-in amplifier. The amplitude is then negated by applying the appropriate DC bias

to the tip. This DC bias is then a quantitative measurement of the surface potential.[10]

Instrumentation for AFM is typically a little more complex than for STM, but is very similar. AFM cantilevers maintain constant force interactions by pulling into or away from the surface through a mechanical connection to a piezo element. Similarly, raster scanning can be achieved with the piezo in the AFM scanner (attached to the cantilever) or by scanning the sample stage. AFM scanning heads are equipped with laser and optical elements that allow for reflection off of the backside of the cantilever onto a four quadrant photodiode positioned somewhere above the tip. For imaging in amplitude modulation dynamic force mode, a lock in amplifier is necessary in order to measure very small changes in amplitude of cantilever oscillation at the vibrating frequency. A preamplifier in the scanning head is necessary for conducting AFM measurements, while a second lock-in amplifier is necessary for KFM measurements to track changes in amplitude due to the oscillating tip bias.

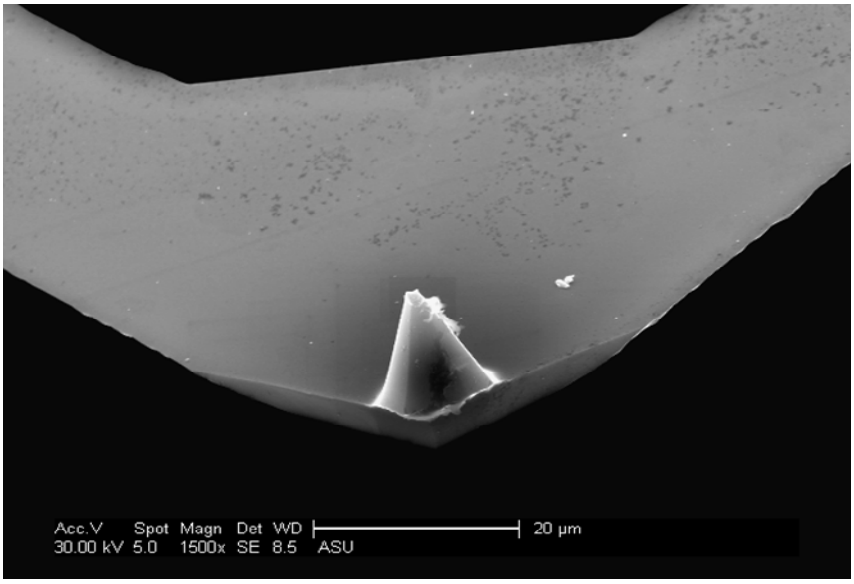

Figure 1.7. SEM image of an AFM tip. The tip is positioned at the end of a cantilever. In this case the cantilever is triangular in shape. This tip is coated with gold for use in CAFM experiments.

AFM cantilevers (See Figure 1.7) are typically made out of silicon using microfabrication techniques. Their size and shape determines their resonant frequency and spring constants. Resonant frequencies can range from a couple of kHz to several hundred kHz and spring constants range from fractions of N/m to 100 N/m. Low resonant frequency tips are useful for oscillating the tip in non-contact mode in liquids, while high resonant frequency tips are standard for intermittent contact mode. Low spring constants are useful when imaging in contact mode, as the lower forces do less damage to both the tip and the sample, while higher spring constant tips are usually used in intermittent contact mode. The tip at the end of the cantilever ranges in radius of curvature from several nanometers to several hundred nanometers depending upon fabrication method and coatings and is chosen based upon potential application. Electrical coatings

for cantilevers can be made by sputtering or ion beam coating materials like gold or platinum, while other conductive materials like boron doped diamond can be created by CVD.[11]

1.1.3. Mercury drop electrodes

Although perhaps not as sophisticated a technique as scanning tunneling or atomic force microscopy, mercury drop electrodes have proven to be efficient tools in studying the electrical properties of organic molecules. Mercury is an unusual element due to its very low melting temperature of 234.3 K[12] making it a liquid metal at room temperature. The liquid nature of the metal make it a versatile electrode for use in various electrical measurements. Mercury drop electrodes are commonly utilized in voltammetry experiments and are often utilized to contact organic layers for conductance experiments. Its cohesive nature and lack of adhesion to most materials make it well suited for forming very flat reproducible contacts. Furthermore, thiolated molecules are able to quickly form monolayers on a mercury surface due to interactions between mercury and sulfur, allowing for a functional group which can make a direct chemical contact to the electrode. This property is an important feature in high quality, reproducible molecular electronics measurements, as will be discussed more thoroughly in the following section.

1.2. Molecular electronics

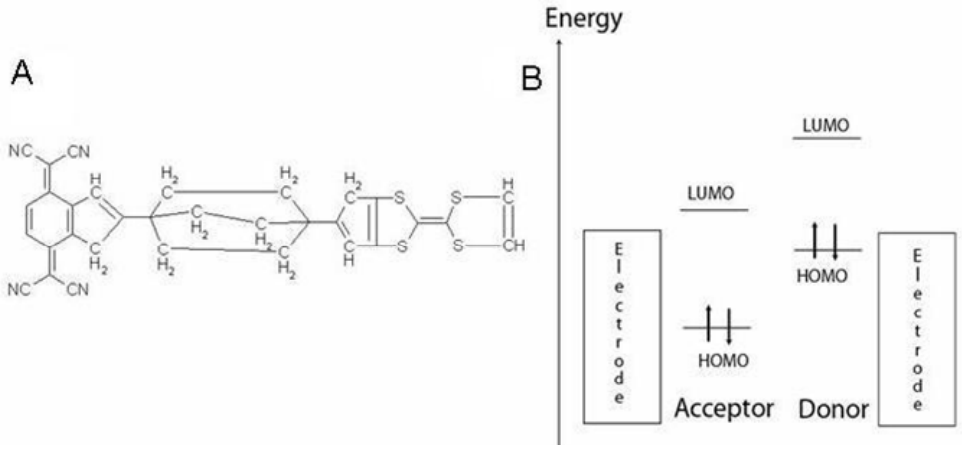

Figure 1.8. Aviram and Ratner molecular diode. A) Chemical structure of the Aviram/Ratner diode. B) Energy diagram of the wired diode.

In 1974 Avi Aviram and Mark Ratner published a paper outlining the design of an organic, single molecule rectifier.[13] Much like a solid state diode, this organic rectifier (see Figure 1.8) once properly connected would only be able to pass current when biased in one particular direction. The rectifier was cleverly designed using properties of organic chemistry. On the left side of the molecule is tetracyanoquinodimethane (TCNQ) which is an electron acceptor, meaning that it can accept another electron at relatively low potential into its lowest unoccupied molecular orbital (LUMO). On the right side of the molecule is a tetrathiofulvalene (TTF) group. This is a well known electron donor, giving up an electron at low potential from its highest occupied molecular orbital (HOMO). The two groups are connected by a single methylene bridge, so as to keep the orientation of the molecule stable. Figure 1.8 (B) shows the energy level diagram,

once properly wired, for this molecular rectifier. The donor should be able to transfer a molecule from its HOMO to the LUMO of the acceptor once the voltage reaches a certain threshold in one particular direction, but not when the bias is reversed. This means that the molecule should, theoretically, act in a similar manner to a solid state molecular diode.

There are several reasons why the ability to make organic molecules work in electronic devices is so intriguing. The versatility of organic chemistry, for instance, could lead to the ability to design molecules to give the exact electrical responses necessary for whatever device is being engineered. Simple rearrangements of organic molecules could lead to fine tuning of electrical devices at the most basic level. The potential of molecules as electronic components however, goes far beyond their application as simple replacements for current solid state electronic components. For instance, many molecules are able to recognize other molecules through chemical bonding, or change behavior upon changes in environment. This ability, coupled with the ability to electrically transduce these signals can lead to the development of highly sensitive electrical chemo-sensors. The device potential of molecular electronics is vast and specific examples will be elaborated upon in later chapters.

1.2.1. Energy levels of electrons in organic molecules

The molecular diode that Aviram and Ratner created in their seminal paper sparked much interest in the field of molecular electronics. What other molecular devices could be created and what would their electronic behavior be

like? As the energy diagram in Figure 1.8 (B) indicates, the location of electron energy levels in molecules is an important component to understanding how molecules might conduct electricity. There are several theoretical approaches, ranging from simple calculations to calculations that require intense computer processing power that can give estimates on molecular energy levels.

Going back to quantum mechanics, the stationary state electronic energy levels for a quantum system can be represented by

$$E = \frac{\langle \psi | H | \psi \rangle}{\langle \psi | \psi \rangle} \qquad 1.2$$

Where ψ is the wavefunction and H is the stationary state Hamiltonian. One method to determine electronic energy states is to use a "trial" wavefunction in the equation for energy. The accuracy of the determined energy will be dependent upon the trial function chosen. To illustrate this idea, the wavefunction is written as a combination of basis functions

$$\psi = \sum_i c_i f_i \qquad 1.3$$

And this trial function can be plugged into the equation for the energy, giving

$$E = \frac{c_1^2 \langle f_1 | H | f_1 \rangle + c_1 c_2 \langle f_1 | H | f_2 \rangle + c_2 c_1 \langle f_2 | H | f_1 \rangle + \ldots}{c_1^2 \langle f_1 | f_1 \rangle + c_1 c_2 \langle f_1 | f_2 \rangle + \ldots} \qquad 1.4$$

Making $H_{ij} = \langle f_i \left| H \right| f_j \rangle$, $S_{ij} = \langle f_i \left| f_j \right. \rangle$ and noting that H_{12}=H_{21} for functions that solve eigenvalue equations, equation 1.4 reduces to

$$E = \frac{c_1^2 H_{11} + 2c_1 c_2 H_{12} + \ldots}{c_1^2 S_{11} + 2c_1 c_2 S_{12} + \ldots} \qquad 1.5$$

With any set of given trial functions, the coefficients can be calculated by minimizing this steady state energy. This is accomplished by taking the derivative of the energy with respect to each consonant and setting that equal to zero. This in turn leads to a series of equations that can be represented with the following matrix determinant

$$\begin{vmatrix} H_{11} - E_\phi S_{11} & H_{12} - E_\phi S_{12} & \ldots \\ H_{12} - E_\phi S_{12} & H_{22} - E_\phi S_{22} & \ldots \\ \vdots & \vdots & \ddots \end{vmatrix} = 0 \qquad 1.6$$

Depending upon the number and types of basis states involved, finding exact solutions to this equation can be incredibly difficult.

A common method for determining energies of molecular orbitals is to use a linear combination of atomic orbitals (LCAO) as a trial function for the molecular orbital. One can determine the energy of the hydrogen molecular orbital, for instance, by combining the 1s orbital wavefunctions of the electrons in the two hydrogen atoms that combine to make the molecule. This combination could then be plugged into the above equations to determine exact coefficients, which eventually leads to the determination of two bonding orbitals with different energies corresponding to the bonding and antibonding states of the molecule.

This method becomes significantly more difficult with atoms that have higher valence.

For an atom such as carbon, molecular orbitals are produced by taking linear combinations of the atomic orbitals for the electrons in the outermost unfilled shell. For carbon this includes two 2s electrons, and two 2p electrons. A molecule like CH_4, however, makes four bonds that are equal in energy and symmetry. Thus, the combination of atomic orbitals for CH_4 will contain the hydrogen 1s wavefunction, as well as 2s and 2p wavefunctions from the carbon atom. This combination of both the s and p states of the carbon atom is referred to as molecular hybridization and the resulting orbitals are referred to as sp^3 molecular orbitals due to the use of all three p states (p_x, p_y, p_z) and the s states in the combination of atomic orbitals.

An unsaturated molecule like ethylene (C_2H_4) forms different bonds than a molecule like ethane (C_2H_6). Ethane contains carbon that is sp^3 hybridized like the example of methane in the previous paragraph. In ethylene, however, each carbon atom is bonded to two hydrogen atoms and contains a double bond to the other carbon atom. The two bonds to the hydrogen atoms and one of the bonds to the carbon are referred to as σ bonds, and are sp^2 molecular orbitals, because each orbital corresponds to mixing of the 2s carbon states and two of the 2p (p_x and p_y) carbon states. The double bond is formed by the combination of the 2 p_z states of the two carbon atoms and the orbital is referred to as a π molecular orbital. The two types of orbitals, σ and π, have different character. Figure 1.9 shows the

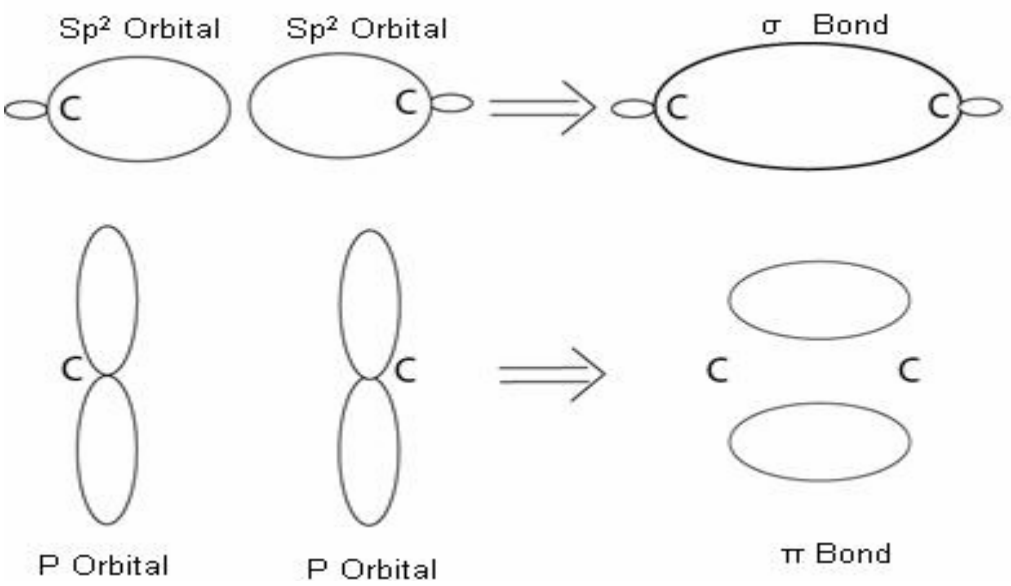

Figure 1.9. Orbital diagrams of sigma and pi bonding.

difference between the two types of bonding. In σ orbitals between carbon atoms, the main sp^2 orbital axis lie on the same line, and the σ bonding orbital is highly symmetric, lying in the plane of the molecule. In the creation of the π orbital, the p atomic orbitals have parallel axis, and overlap in a less symmetric way above and below the atomic plane of the molecule. The lack of symmetry of the π bond indicates that the carbon-carbon bond cannot be rotated, creating a more rigid structure than is seen in ethane.

One simple means of examining electronic states in π orbitals in unsaturated organic molecules, such as ethylene, is to make certain assumptions about the quantities shown in equation 1.6**.** Those assumptions are that the overlap integrals, S_{ij}, are zero except for when i=j, H_{ii} is the same constant (α) for all carbon atoms, and H_{ij} is zero for all but adjacent atoms for which it is equal to

β . These assumptions make up what is known as the Hückle model. For ethylene, the determinant in equation 1.6 reduces to

$$\begin{vmatrix} \alpha - E & \beta \\ \beta & \alpha - E \end{vmatrix} = 0 \qquad 1.7$$

Which leads to $E = \alpha \pm \beta$, with β being negative for an attractive potential. Plugging the value for energy back into the coefficient equations, gives the value of the coefficients for the wavefunctions of the π orbitals. This process is expanded for molecules with more carbon atoms, such as butadiene or benzene, but is essentially the same.

Obviously, calculating electronic energy states accurately can get complicated very quickly, even when certain terms are left out of the equation and trial wavefunctions are utilized. For this reason, another method to calculate energy states is often employed which does not rely on the use of wavefunctions. This method is referred to as Density Functional Theory and was first postulated as a method to determine energy levels and electron densities in materials by Hohenberg and Kohn in 1964.[14] In this theory an energy functional, E[n(r)],of the electron density function n(r) is implemented to calculate energy states. The value of this functional is determined at various states of the electron density until a minimum is realized. This, then, gives a good estimation of electron density in the ground state and ground state energy. Density functional theory is well utilized in molecular electronics to determine energy states for determination of electron transfer rates.[15,16]

1.2.2 Electron transfer

Electronic energy levels in organic molecules are only part of the story behind molecular electronics. How electrons transfer from one part of a molecule to another, or from molecule to molecule is of equal importance and questions about the rate of electronic transfer are not simply understood by reading an electronic energy diagram. For example, if there is a electron transfer reaction that has zero free energy difference, electrons still do not randomly transfer from one reactant to another as one would expect. The transfer must still be thermally activated due to environmental factors. When an electron is on one reactant, the solvent around that reactant is organized in a particular manner. In order to transfer the electron to the other reactant, the solvent must reorganize onto the other reactant; a process that requires energy not related to the electronic states of the molecule. For this reason, thermodynamics play a large role in electron transfer reactions.

Rudolph Marcus won the Nobel Prize in Chemistry in 1992 for his work on the thermodynamics of electron charge transfer in molecular systems which began in 1956 and is now known as Marcus theory.[17] In his theory, energies of the reactants and products of an electron transfer reaction were represented with a single reaction coordinate, q, which represents all the parameters involved in the electron transfer. Setting this value equal to zero when the electron is on the product, the energy of the product is equal to

$$E = \frac{1}{2}kq^2 \qquad 1.8$$

This is quadratic because the leading term of an energy expansion about the minimum is quadratic and higher order terms are ignored in this theory, assuming that perturbations are small. The minimum energy of the reactants, then, occurs at some other coordinate, q_R so that the energy of the reactants is equal to

$$E = \frac{1}{2}k(q - q_R)^2 + \Delta G^0 \qquad 1.9$$

Where, ΔG^0 is the difference in free energy between the products and reactants, and k is the same as in equation 1.8 in order to make the following math easier, noting that this is not typically the case for real systems.

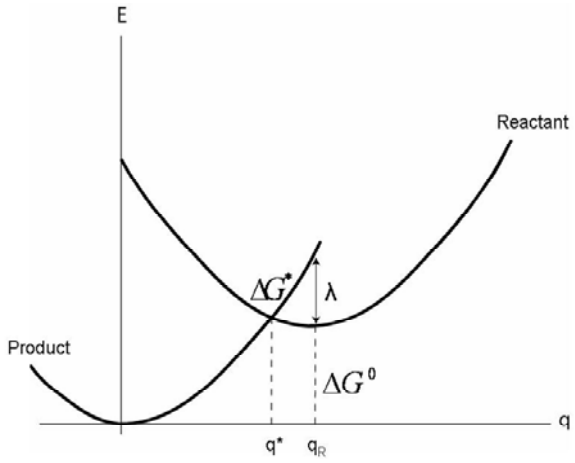

Figure 1.10. Marcus energy diagram.

This energy system is plotted in Figure 1.10. Clearly, at some point, q^*, the energies of the products and reactants are equal, and for closely coupled, adiabatic systems, once the reactant thermally fluctuates to that reaction coordinate, the electron will transfer to the product. In the absence of thermal energy, however, the energy needed to overcome solvation, the solvation energy, is λ. Solving for the point that allows for thermally activated electron transfer, q^*, gives

$$q^* = \frac{1}{kq_R}(\frac{1}{2}kq_R^2 + \Delta G^0) \quad 1.10$$

Leading to an effective activation energy of

$$\Delta G^* = \frac{1}{2}kq^{*2} = \frac{1}{2kq_R^2}(\frac{1}{2}kq_R^2 + \Delta G^0)^2 \quad 1.11$$

Noting from Figure 1.10 that the squared sum in the energy can be related to the solvation energy by

$$\lambda + \Delta G^0 = \frac{1}{2}kq_R^2 + \Delta G^0 \quad 1.12$$

The activation energy can be reduced to

$$\Delta G^* = \frac{(\lambda + \Delta G^0)^2}{4\lambda} \quad 1.13$$

Thus the rate of electron transfer is proportional to

$$P \propto \exp(-\frac{(\lambda + \Delta G^0)^2}{4\lambda k_B T}) \quad 1.14$$

This result clearly shows how, even if the free energy difference, ΔG^0, is zero, the rate of electron transfer is thermally activated due to the solvation energy, λ.

1.2.3. Experimental methods for molecular electronics research

The Aviram Ratner diode was a rather revolutionary idea. However, putting the idea into practice has proven difficult over the decades. Creating stable, reliable contacts to molecules is a challenge to the field of molecular electronics,[18] as is maintaining the chemical stability of the molecules themselves. The question of how to wire a single molecule to two electrodes for measurement purposes has been answered by a variety of different techniques. It is important

to note, however, that no experimental technique is a perfect method for examining the electronic properties of single or small ensembles of molecules. Every technique has its own benefits and drawbacks, but the knowledge gained from all of the experimental techniques gives a better view of actual electronic processes in organic molecules, and they also point out the challenges in creating future potential devices.

One early method for these types of measurements was to try to insert a single or small ensemble of molecules between two electrodes that had a very small gap. Needless to say, creating a gap that is large enough so that a molecule can be inserted, yet small enough to keep anything larger than 1 or 2 single molecules is tricky. One method of designing very small electrodes which has been used with some success has been to drive a very higher current through a thin piece of metal. This electric current is so strong that it actually moves the atoms of the metal, and eventually creates a very small gap that stops the current. This phenomena is known as electromigration. Once the gap is made, molecules can be inserted into the gap and appropriate voltage can be applied. The electromigration method of break junction creation has been used to study transistor effects in fullerene,[19] as well as Kondo effects (low temperature conductance effects due to magnetic interactions) in divanadium.[20] The drawbacks of the method are inconsistent gap formations and the difficulty in utilizing the created gap for multiple experiments.

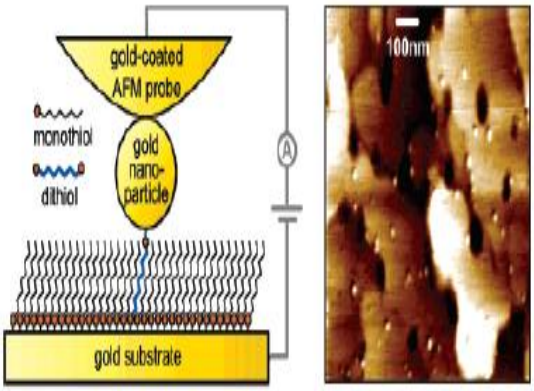

Figure 1.11. Design and image of experiment to measure single molecule conductance using gold nanoparticles and conducting AFM.[21] The left image shows the schematic of the experiment and the right image shows a typical AFM image with gold nanoparticles.

Utilizing scanning probe techniques to study molecular electronics has proven fruitful over the last decade. One creative method to wire molecules to electrodes and study molecular conductance has been to sandwich molecules between a conductive substrate and a metal nanoparticle and to contact the nanoparticle with a conducting AFM probe. Cui et al. demonstrated this method by creating a self assembled monolayer (SAM) of octanethiol on a planar gold surface (see Figure 1.11). Octanedithiols were then inserted into this monothiol matrix. Gold nanoparticles introduced to the surface selectively bonded to the isolated octanedithiol molecules. Scanning these types of surfaces with a conducting AFM showed images of the gold nanoparticles. The conducting AFM tip could then be placed in contact with the metal nanoparticles and successfully create a gold-molecule-gold junction through which to conduct current. The resulting IV curves actually proved to be multiples of the lowest conductance IV curve,

indicating that more conductive curves represented junctions with more molecules in them. One noticeable feature in all the curves, however, was the lack of current below a certain voltage in both forward and reverse bias directions. This was attributed to coulomb blockade effect in the small nanoparticles. This coulomb blockade effect was verified in later experiments utilizing larger nanoparticles that have much lower charging energies.[21] This method proved to be a reliable method for measuring the conductances of different molecules.[23,24]

Another widely utilized method for determining the conductance of organic molecules has been the STM break junction method. Pioneered by Xu and Tao[25], this method has proven to be widely robust and provides results that are within an order of magnitude of theoretical calculations of molecular conductance.[26] Using this method, bifunctionalized molecules are either attached to a metal surface or they are floating in solution above a metal surface. An STM tip is brought into and out of contact with the surface repeatedly while the current decay is measured (see Figure 1.12). When there is no molecule trapped within the gap, the current decays exponentially with distance from the

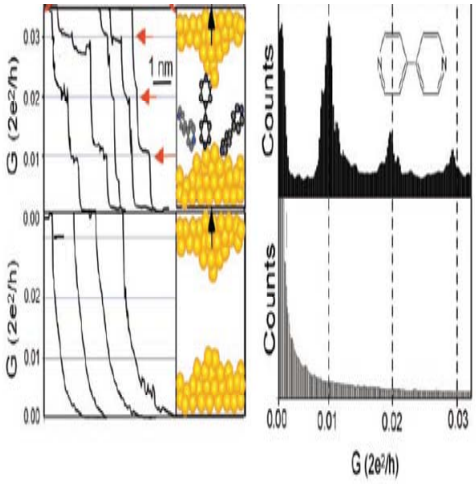

Figure 1.12. Schematic of STM break junction experiment.[25] The curves in the top left show steps from molecules in the electrode gap, while below it shows curves with no molecules. To the right are the resulting histograms from the two situations.

surface. If a molecule attaches to both the surface and the tip, however, the current decay curves display very distinct plateaus or "steps." These steps occur because, once a molecule is stuck in the gap, the gold on the tip begins to stretch as it pulls away from the surface. So, although the voltage on the piezo is still pulling upwards, the distance of the gap remains unchanged, along with the current. If all of the curves that have these plateaus are put together to form a conductance histogram, there will be peaks where these steps occur. These peaks are typically multiples of the conductance of the first peak, and correspond to the conductance of 1, 2, 3… molecules stuck in the gap. This is a fairly easy and direct way of measuring the conductance of a single molecule. Similarly, the CAFM can be utilized to determine both the conductance of single molecules and the force required to break the molecular junction simultaneously.[27-29]

Molecular electronics measurements can also be conducted using the STM under potential control. The break junction measurement, for instance, can be used to understand how the conductance of different molecules changes by applying different potentials. This is done in electrolyte solution with a reference and counter electrode (see Figure 1.13). Visoly-Fisher et al. used this method to study the conductance of carotenoids, which are conjugated molecules

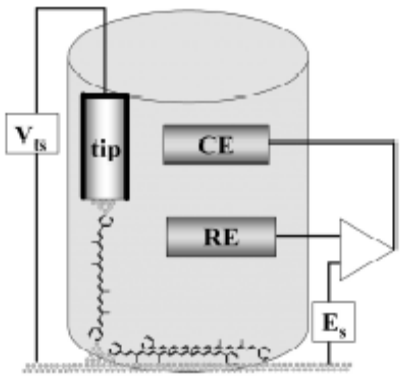

Figure 1.13. Schematic of STM under potential control.[30]

known to exist in photosynthetic complexes, under potential control.[30] Carotenoids are thought to act as a means to discharge excess electrons that could be potentially damaging in photosynthesis. The study showed that the carotenoids become more conductive upon oxidation, which may be one of the first steps in switching on this electron pathway. This method of potential control can also be seen as creating an electrochemical "gate" and is used to study gating effects on molecular systems.[31,32]

Another method of experimentally connecting molecules to two electrodes has been to use a mercury drop electrode. In this method a self assembled monolayer can be created on an electrode surface such as gold. A drop of mercury can then be brought down onto this layer, and a voltage can be applied between the mercury drop and the conductive surface. This process is relatively more simple than the process of creating an electromigrated break junction, as mentioned in the previous paragraph, since the junctions made are adjustable by simply changing the height of the mercury drop. Furthermore, the mercury drop can be used to study different positions on the same SAM surface. This method, however, creates a larger electrode area, and, thus typically precludes single molecule work. This method has been utilized to study conductance through alkyphosphonate monolayers,[33] as well as negative differential resitance effects in molecules that have cyclic disulfide groups.[34]

2. DNA SEQUENCING BY RECOGNITION

Deoxyribonucleic acid (DNA) is a molecule that forms the basis for the diversity in life seen on Earth. Every living cell contains this same chain-like molecule, but the chain sequence differs from species to species and from individual to individual. In humans, the sequence of nucleic acids (bases) in DNA determines a multitude of traits, from relatively inconsequential characteristics like eye color to serious potential conditions such as predispositions to cancer. Despite the importance of DNA, there is yet to exist a simple, cost effective method for determining the entire sequence of the human genome. An advance in science that would bring the cost of DNA sequencing down to $1000 per genome (a goal set by the National Human Genome Research Institute which is a branch of the National Institutes of Health[35]) could lead to great advances in personal diagnostics and personalized medicine. As the cost of health care continues to increase, these advances may very well lead to more effective, targeted treatment and prevention of disease, which could potentially decrease the cost associated with the long term maintenance of many individuals with diseases that, to date, can not be effectively cured.

Although there is currently a reliable method to sequence DNA, it is too costly and too slow to be of practical use in determining the sequence of any particular person's genome. For this reason, many resources have been employed to determine a better way to sequence DNA. One particularly interesting method being researched is the idea of using the process of chemical recognition at the

single base level to determine genetic sequences. The structure of DNA will be elaborated upon later in this chapter, however it is well known that DNA is composed of complimentary strands of nucleotides made of four distinct bases. Each base reliably hydrogen bonds with only one of the other bases to form the highly recognizable double helix structure. The idea behind sequencing by recognition is to utilize molecules that can reliably bind to the bases when the DNA is in single strand form. A single molecular "reader" or several different molecules could be employed that could interact with the different bases on a single strand of DNA, and if this interaction could be transduced into a recognizable signal that was base specific, it is possible that this could lead to a high throughput method of DNA sequencing. Challenges to this method include how to transduce the interaction between readers and bases into reliable signals and how to construct a robust device that can easily read long single strands of DNA by base recognition. To understand these challenges better, a basic understanding of DNA structure and function is necessary.

2.1. Deoxyribonucleic acid (DNA)

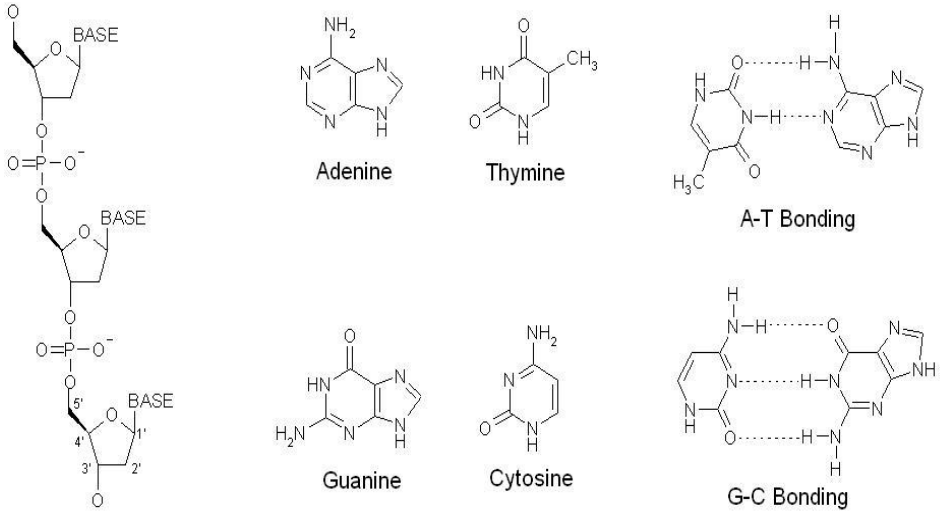

Figure 2.1. Molecular structures of DNA components. The picture on the left shows how the DNA sugar rings are connected through a phosphate backbone. The middle images show the structure of the DNA bases, and the image on the right shows how these bases hydrogen bond with one another.

Figure 2.1 shows the chemical structures that make up DNA. DNA is comprised of chains of 2'-deoxy-D-ribose (5 member sugar rings) connected together through a phosphate backbone. Attached to each of the sugar rings is one of four heterocyclic nitrogen compounds, commonly referred to as bases. Two of these compounds, adenine and guanine, are substituted purines, while the other two, thymine and cytosine, are substituted pyrimidines. Each base is able to reliably hydrogen bond to one other base. Adenine hydrogen bonds to thymine forming two hydrogen bonds, and guanine binds to cytosine forming three hydrogen bonds (see Figure 2.1). In this way, complementary single strands of

DNA are able to bind to one another to form the well known double helix structure.

The image on the left of Figure 2.1 shows how the sugar rings of DNA are linked by the phosphate backbone. This image only shows the linking of three sugar rings, but the sequence can go on to an infinite number of links. In DNA nomenclature, the carbons on the sugar ring are labeled with a prime symbol, distinguishing them from the carbons in the bases. Clearly, from the structure, single stranded DNA has two different ends, the 5' end and the 3' end. In double stranded DNA, the complementary DNA strands are bound together with opposing ends. The 5' end of one strand of DNA matches with the 3' end of the other strand. This is an important factor in the processes that lead to protein assembly, as DNA is only read from the 5' end to the 3' end.

A base attached to 2'-deoxy-D-ribose (the sugar ring in DNA) is referred to as a nucleoside. The nucleosides are then adenosine, guanosine, cytidine and thymidine. A nucleoside that is bound to a phosphoric acid, either at the 5' or 3' position is referred to as a nucleotide. Nucleotides are referred to by the nucleoside, the position of the phosphate and the form of the phosphate. Nucleosides can bind to a phosphoric acid in the monophosphate, diphosphate or triphosphate form. For instance, adenosine bonded at the 5' position to a triphosphate is referred to as adenosine 5'-triphosphate (ATP). Nucleoside triphosphates are the building blocks of DNA synthesis, during which the other 2

phosphates cleave off. ATP, by itself, has important roles as energy carriers in biological processes as well.

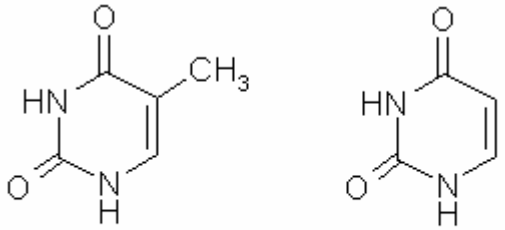

Figure 2.2. Molecular structures of thymine and uracil. Thymine is utilized in DNA and uracil is used in RNA

In the cell, DNA is translated into another biopolymer called ribonucleic acid (RNA). DNA differs from RNA in two ways. RNA has an OH group attached to the 2' position of the sugar. RNA also does not utilize the base thymine. In RNA the thymine base is replaced with another substituted pyrimidine, uracil. Figure 2.2 shows the difference between thymine and uracil. For translation to occur, the double strand of DNA has to be unwound. Once the DNA has been unwound, one of the strands, referred to as the template or antisense strand, is read from the 3' end and complementary bases of RNA bind to the DNA and are linked together. The resulting strand of RNA contains the exact same information as is contained in the DNA since the strand is complementary. This RNA strand is then able to move outside of the cell nucleus and play one of several vital roles in protein synthesis.

First Base	Middle Base				Last Base
	U	C	A	G	
U	Phe	Ser	Tyr	Cys	U
	Phe	Ser	Tyr	Cys	C
	Leu	Ser	Stop	Stop	A
	Leu	Ser	Stop	Trp	G
C	Leu	Pro	His	Arg	U
	Leu	Pro	His	Arg	C
	Leu	Pro	Gln	Arg	A
	Leu	Pro	Gln	Arg	G
A	Ile	Thr	Asn	Ser	U
	Ile	Thr	Asn	Ser	C
	Ile	Thr	Lys	Arg	A
	Met	Thr	Lys	Arg	G
G	Val	Ala	Asp	Gly	U
	Val	Ala	Asp	Gly	C
	Val	Ala	Glu	Gly	A
	Val	Ala	Glu	Gly	G

Table 2.1. The genetic code. Each three letter base segment in RNA codes for a different amino acid, or codes for the end of transcription (stop codon).

DNA codes for 3 types of RNA. Messenger RNA (mRNA) codes for the peptide sequence of a protein to be synthesized. Ribosomal RNA (rRNA) is a structural component of ribosomes, which is where proteins are synthesized within the cell. Finally, transfer RNA (tRNA) binds to and carries amino acids to the ribosome as the mRNA is read. Within the ribosome, the mRNA is read, and each three base segment either codes for one of the 20 amino acids found in proteins or signals for the stop of protein synthesis. These three base segments are referred to as codons. Table 2.1 shows the code for amino acids from RNA bases. As the RNA is read in three base segments, tRNA brings in the associated amino acid and a subunit of the ribosome binds the amino acids together as the

peptide chain grows. This process keeps on going until the a specific "stop" codon is read.

Proteins serves many vital functions in living systems, and thus, the DNA that codes for them is a precious structure in cells. For this reason, sequencing of DNA has, and continues, to play an important role in biological sciences. Furthermore, protein generation and regulation is imperative in maintaining optimal health, and many diseases are linked to problems related to proteins. The ability to sequence the human genome at a fraction of the current cost and time could potentially lead to detection of future diseases and increased implementation of individualized medical treatment.

2.2. Sequencing of DNA

Modern day DNA sequencing is almost always completed through a process developed in the early 1970s by Frederick Sanger.[36] The human genome is very large with just over 3 billion base pairs,[37] and so a high throughput method is needed to sequence it in a reasonable period of time. One of the first steps in the Sanger method is to chop the DNA into much smaller sequences. This is done with an enzyme called a restriction endonuclease. There are several hundreds of these enzymes and they each work by cutting DNA at very specific sequences.

After chopping, the DNA fragment to be sequenced is labeled with a small piece of DNA that contains a tag that can be identified later (either ^{32}P or a fluorescent label). This strand is referred to as a primer and marks the point where DNA synthesis will occur. All four 2'-deoxyribonucleoside triphosphates

(the building blocks of DNA synthesis), one of the four bases in 2',3'-dideoxynucleoside triphosphate form, and DNA polymerase (the enzyme that adds DNA nucleotides to the chain) are combined. Nucleotides will be added to the primer strand until one of the 2',3'-dideoxynucleotides gets added with copies of the labeled DNA fragment. Nucleotides are joined to the DNA chain by the 3' OH group on the sugar ring at the end of the chain attacking the α-phosphorous of a nucleoside triphosphate. Dideoxynucleotides do not have the hydroxide group at the 3' position on the sugar, and thus cannot react with the next nucleotide to further the chain. The point at which the 2',3'-dideoxynucleotide gets added is stochastic. In a given reaction with multiple copies of the DNA fragment to be sequenced with the primer, there will be an array of DNA fragments synthesized with different lengths, all corresponding to where the 2',3'-dideoxynucleotide was randomly added to the chain. This reaction is repeated using the same DNA fragment to be sequenced with the other three 2',3'-dideoxynucleotides.

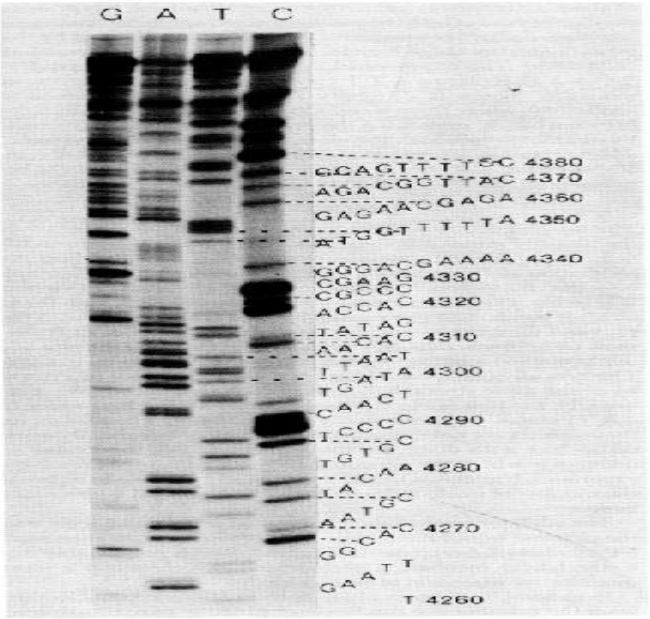

Figure 2.3. Autoradiograph gel for reading the sequence of DNA. Each track represents the lengths where each particular base occurs.[36]

Once the sequence has been reacted with all four 2',3'-dideoxynucleotides, the synthesized fragments, all of different lengths, are separated by length. If ^{32}P is used to label the DNA, then the fragments corresponding to each of the four 2',3'-dideoxynucleotides are loaded into separate lanes of a polyacrylamide gel. An electric field is applied and the fragments travel down the gel distances that are relative to their lengths (masses). When the gel is exposed to a photographic plate which is then exposed to radiation, the position of each fragment shows up as a dark band. Since each lane contains fragments from a different 2',3'-nucleotide added to the chain, each lane then represents all the lengths along the original sequence where that particular nucleotide occurs. By examining all four lanes together (see Figure 2.3.) one can determine by visual inspection the sequence of the original DNA.

As discussed previously, most modern day DNA sequencing uses a variation on the basic Sanger method. For higher speed and more automated

reads, the DNA fragment to be sequenced is labeled with one of four fluorescent dyes. Capillary electrophoresis is used to separate the different lengths of DNA that were synthesized, and as these fragments exit the capillary, the fluorescence signature is detected by laser excitation, and the sequence can be decoded very quickly by software systems.[38] Accuracy in these systems is very high and they can now read as many as 1000 base pairs in a DNA fragment. However, at a price of $0.50 per thousand bases sequenced,[38] the price to sequence the human genome would be approximately 1.6 million dollars, which is obviously far to high to make genomic sequencing a modern day reality for individuals.

2.3. Sequencing by recognition

2.3.1. Benefits of sequencing by recognition electron tunneling

As explained above, Sanger sequencing works well for short reads of DNA sequences, but sequencing the entire genome through this process, as automated as it has become in recent years, is still a timely, expensive venture. New approaches to DNA sequencing have been deemed necessary for high throughput, cost effective sequencing of mammalian genomes. One method of sequencing that has received a good deal of attention over the last few years has been to pass single stranded DNA through a nanopore which can read each base as it passes sequentially through. If the nanopore itself can read the DNA bases, the costs of a nanopore sequencer may be drastically lower than traditional Sanger sequencing.

Initially, when nanopore sequencers were being studied, it was thought that the sequence of DNA could be read by examining ionic current through the nanopore. Applying a voltage to the nanopore in the presence of an ionic liquid creates an ionic current through the nanopore.[39] In the presence of another molecule, like DNA, this current reduces at times when the molecule is translocating through the nanopore due to the fact that the bulkier molecule blocks a fraction of the ions from getting through and thus reduces the current flow.[40] It was thought that if different DNA nucleotides blocked the flow of the ionic current by different amounts, then the base sequence of DNA could be immediately read from a current trace of the nanopore as the DNA translocates through the pore.

At first, this process of ionic current readout appeared to be working for RNA. RNA strands of a purine base had a different ionic current signature than those of a pyrimidine base when passed through an α-hemolysin pore.[41] More interesting was the fact that RNA with two joining segments, one of a purine and one of a pyrimidine, could be translocated through a nanopore and the point of switching from one base to the other could be detected.[41] The results, however, were disappointing when using DNA. Different bases had very little difference in current signature, and it was eventually determined that the difference noticed in the RNA strands had more to do with different base stacking than with single nucleotide current blockage.[42] In fact, it was determined that the current signature differences were actually due to geometric consideration of as many as 20

nucleotides in the nanopore at a time. This was, of course, a setback for nanopore sequencing.

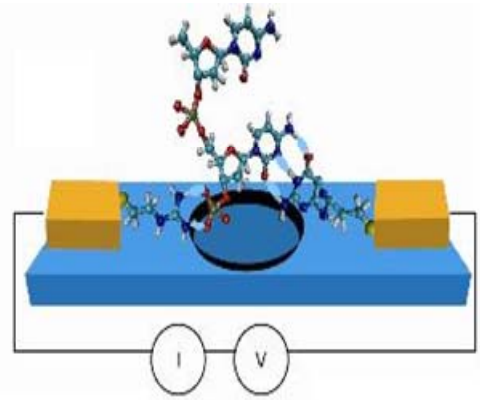

Figure 2.4. Schematic for a nanopore DNA sequencer utilizing molecular tunneling recognition.[43]

Sequencing by recognition is a way to get around the lack of contrasting current signature in a nanopore. In a recognition nanopore device, a molecule that could bind to the nucleotides would be attached to electrodes near the nanopore. As nucleotides exit the nanopore, they would interact with these "reader" molecules and create a unique conductance signature. A scheme for such a system is shown in Figure 2.4, where a reader molecule hydrogen bonds to a single nucleotide while another molecule grabs the phosphate backbone. This could either be accomplished with a single type of reader molecule that interacted with and gave a different current signal for each DNA nucleotide with which it encountered, or there could be separate reader molecules for each nucleotide and many copies of the DNA sequencing strand could be translocating through many pores with a different reader molecule at the end. Examining current signatures through all pores would then give a base readout for the entire segment of DNA, but would

require consistent synchronization of the translocation events of all the DNA strands. Of course, the future of sequencing by recognition is dependent upon the ability to create reader molecules that can accurately identify single nucleotides through a conductance signature. The following section and chapter explore how different experiments can be utilized to determine conductance through molecules hydrogen bonded to DNA bases.

2.3.2. STM measurements of sequence recognition

As the previous chapter explained, the ability to specifically recognize a molecule and then transduce that recognition into an significant electrical signal is a key benefit of many molecular electronic applications. One potential scheme to sequence DNA by recognition elements is to have a binding molecule recognize each base and produce a measurable and distinct electrical signal so that the electrical signal can be used to read out the sequence of bases in DNA. The goal is to produce a quick and efficient DNA sequencer. One of the biggest challenges, however, is to determine the structure of a highly selective base reading molecule, and, further, to determine how the base- reader complex operates electronically in order to effectively calibrate a unique signal upon recognition of a specific base.

The natural starting molecule to examine as a base reader is the complementary base itself. For example, if one wanted a molecule that specifically interacted with the base adenine and produced a recognizable electronic signal, the first molecule to try would naturally be a molecule that was

structurally similar to thymine. Since adenine binds very strongly to thymine, it is possible that measuring the current through an adenine-thymine bond may be significantly higher than through the solvent or through a base mismatch, and this current could be utilized as the electronic recognition signal.

There have been several reports regarding the utilization of the scanning tunneling microscope to examine the conductance relationship between hydrogen bonded base pairs. STM probes are very sharp, and thus, make excellent electrodes for this type of single molecule work. Ohshiro and Umezawa utilized the STM to study the electronic interactions between base pairs by imaging substrates containing self assembled molecules of bases with a gold tip that was functionalized with another base that could hydrogen bond with the bases on the surface.[44] While the bases could be imaged with an unmodified tip, contrast was greatest when imaging a SAM of a single base with a tip modified with its complementary base. Furthermore, single complementary bases were identified in high contrast while imaging a surface comprised of a mixture of different bases, meaning that the tip was able to recognize the complementary base and distinguish it from non-complementary bases in the SAM matrix. In addition, the sequence of a short segment of a peptide nucleic acid consisting of two different bases could be identified utilizing a tip modified with one of the complementary bases. Although the time scale involved with STM imaging makes it an unviable means of sequencing DNA, the implications of these results are clear. The transverse conductance of DNA associated with through-base tunneling is more

than the tunneling through an unbonded base, or through a non-complementary molecule. This is evidence that DNA may be able to be sequenced by recognition electron tunneling.

Ohshiro and Umezawa's work with the STM showed the potential of studying transverse electron tunneling through base pairs, and even showed how it would be possible to identify the sequence of a simple pattern of peptide nucleic acid. Peptide nucleic acid (PNA) differs from DNA, however, in that it has no phosphate backbone and includes amino groups that are able to interact readily with a gold substrate. Repeating this type of work on DNA would prove slightly more complicated. One method to study the transverse base pair tunneling interactions in DNA was to utilize guanadinium ions (see Figure 2.5), which can hydrogen bond to phosphates as linkers between DNA and gold substrates. The guanadinium monolayers were formed on the gold surface through a thiol bond. DNA, both double and single stranded, can then be introduced to the monolayer and forms densely packed layers on the surface,

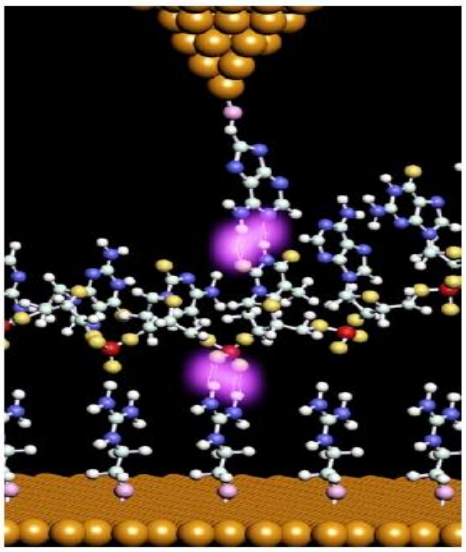

Figure 2.5. Schematic of STM tunnel decay experiment on DNA oligomers.[45] The guanadiunium on the gold surface hydrogen bonds to the phosphate backbone of the DNA, while the functionalized tip binds to the bases.

interacting strongly with the guanadinium.[46] This system then provides good electrical linkage between the DNA and the gold surface.

This DNA-guanadinium system can be utilized to study the interaction between base pairs on DNA, as opposed to PNA in previous work. Adsorbing single stranded DNA on the guanadinium monolayer leaves the bases open to study by the STM probe. This system was studied by He et al. by examining the electron tunneling decay distances while moving base modified and bare gold STM tips into and out of close contact with the DNA layer on the surface (see Figure 2.6).[45] For surfaces that contained DNA of a single base, it was found that the tunneling current would extend much farther (out to 2 nm) if the tip was functionalized with a molecule that could base pair with the base on the DNA than if the tip was bare or functionalized with an incompatible molecule (see Figure 2.6). For example, for a layer of cytosine DNA, the current with a G functionalized probe would extend out to 2 nm, but with a 2-aminoadenine (2-

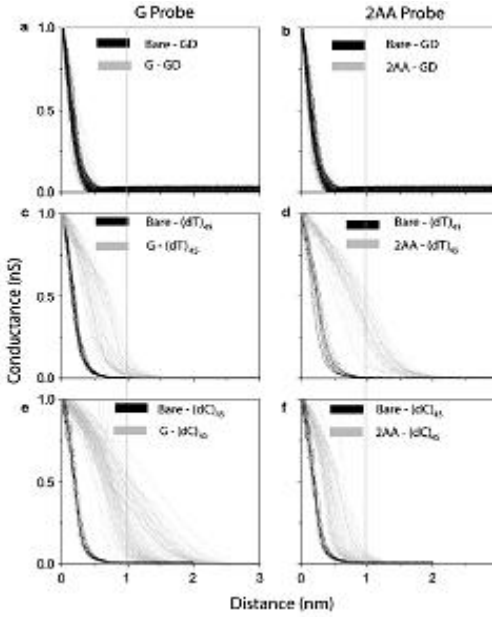

Figure 2.6. STM tunneling decay curves for different base functionalized tips and a DNA-Guanadinium surface.[45] The solid black lines show cures from bare tips on different DNA surfaces, and the lighter curves are decay curves from functionalized probes.

AA) probe it would only extend to 1 nm, and with a bare probe the current had completely decayed by 0.5 nm. Similarly, for a surface of T-oligomer, the current extended further with a 2-AA probe (2-AA can form 3 hydrogen bonds to thymine), than with a G probe or a bare probe.

Integrating these curves gives the charge transferred during the retraction process. Figure 2.7 (a) shows the charge transferred for a G probe on a guanidium surface, T oligo $(dT)_{45}$ surface and a $(dC)_{45}$ surface, the charge transferred for a 2-AA probe on the same surfaces, and the charge transferred for a bare probe on the same surfaces. Clearly, the more charge is transferred in systems of strong hydrogen bonding interactions (G-probe and $(dC)_{45}$ and 2-AA probe and $(dT)_{45}$). From this data, it was determined that using a threshold of 2.2

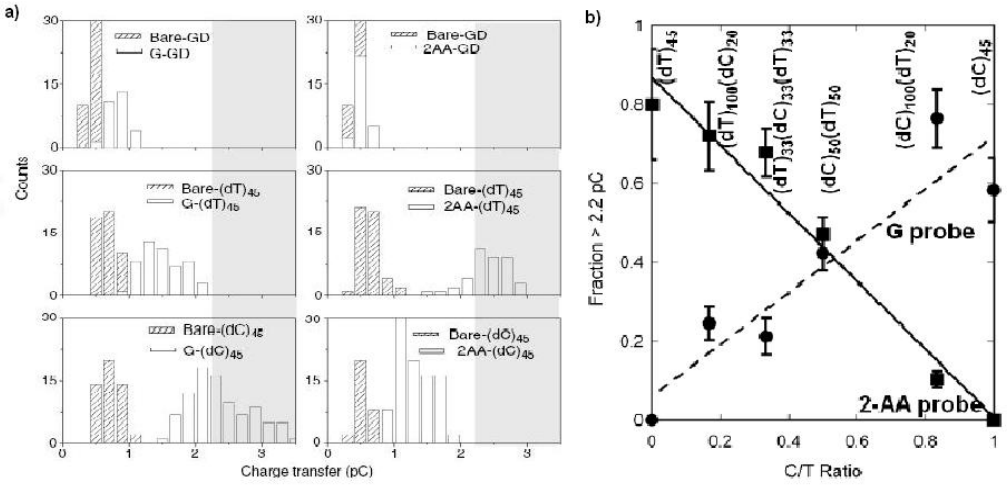

Figure 2.7. Charge transferred during STM probe retraction. a) Histograms of charge transferred with different surfaces and different tip functionalization. b) Fraction of positive recognition events compared to C/T ratio in DNA oligomer for both G probes and 2-AA probes. [45]

pC as a positive recognition event would yield a 50% recognition rate for G reading C, and an 80% recognition rate for 2-AA reading T. To test the specificity of these interactions, surfaces with oligos containing ratios of T and C in blocks were utilized and the fraction of positive recognition events (Q>2.2 pC) was plotted for each probe against the ratio of T and C in the oligo. The charge transfer was remarkably good at determining the ratio of the two bases in the oligos (see Figure 2.7 (b)) down to a block of target bases of 20. If the target block was under 20 bases, reliable results were unattainable for reasons that will be elaborated upon in the next chapter.

This tunneling decay method with the STM was further studied with nucleosides (bases with sugar rings but no phosphate backbone) as monolayers on gold surfaces connected through a thiol bond attached to each base.[47] Probes were functionalized with 2-aminoadenine, guanine, adenine or thiophenol. Thiophenol does not hydrogen bond with DNA bases, but was utilized as a control molecule. As with the DNA, it was noted that experiments that utilized tips that hydrogen bonded with the target nucleoside on the surface had tunneling curves that extended further than tips on bare targets or tips with molecules that did not hydrogen bond to the target nucleoside. Furthermore, it was shown that base combinations that made three hydrogen bonds extended even further than base combinations that formed two hydrogen bonds.

These experiments were conducted by holding the tip at a setpoint current and then retracting them at a given speed. Curiously, the setpoint current strongly

affected the shapes of these curves. For instance, a curve that began at a setpoint of 2 nA was not simply the lower part of a curve that began at 3 nA. Taking a polynomial fit from a curve at a higher setpoint and comparing the fit to the curves at lower setpoints showed very clearly that there was a fundamental difference between curves at different setpoints. Furthermore, the charge transferred in these experiments was highly correlated with the initial setpoint. These results, along with the fact that the decay distances were much longer than typical electronic processes, and the fact that, upon approach, the tips had to be brought much closer into the surface and had very steep current increases led to the belief that the curves were representative of both electrical and mechanical processes. This electromechanical system was studied further using the CAFM, and results from those experiments will be shown in the next chapter.

3. ADHESION FORCE AND CONDUCTANCE MEASUREMENTS OF DNA NUCLEOSIDES

Previous STM experiments on tunneling through DNA bases gave preliminary evidence that the current signature of hydrogen bonding between complimentary bases and nucleosides could be used as a recognition signal in a nanopore molecular recognition sequencer. The data, however, left some unanswered questions. The STM data on the DNA oligomers could only resolve nucleotides that were in segments greater than 20 bases. Furthermore, the STM withdraw curves on the nucleoside surfaces varied significantly as the current setpoint changed and extended much further out than electronic processes indicate. To demonstrate the dependence of curve shape on setpoint, Figure 3.1 shows the STM data for a guanine functionalized probe on a cytidine surface at several different setpoint. The curve at 3 nA is fit with a polynomial whose function is used to fit the other curves at different setpoints by simply shifting the function to the other current setpoint.

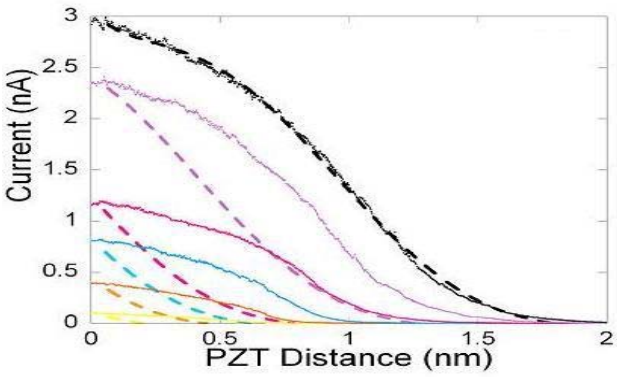

Figure 3.1. Initial STM retraction curve fits for a guanine functionalized probe retracting from a cytidine functionalized surface. The 3 nA curve is fit by a polynomial whose function is used to fit the other curves. Clearly, the function does not fit the other curves well.

The predicted curve simply does not fit any of the other curves with any degree of precision, which clearly shows this change is curve shape.

Because of the discrepancy between what is expected for purely electronic single molecule work and what was seen in the actual STM data, it was suggested that these retraction curves represented more than electronic processes and there were, in fact, geometric and mechanical factors influencing the measurements. With the STM, however, it is difficult to separate mechanical and electrical data in a single measurement since the tip is purely controlled by electronic tunneling. It is easier to understand how mechanical factors influence an electrical measurement if the measuring device has the ability to separately monitor mechanical effects. For this reason, the conducting AFM was utilized to understand the electromechanical properties of the base-nucleoside system.

Chapter 1 explained some of the benefits of utilizing the conducting AFM. Specifically, in this case, the same measurement that was conducted utilizing the STM can be performed on the AFM. However, in the case of the AFM, the force on the flexible cantilever can be recorded simultaneously with the electrical current. By comparing mechanical force with different attributes of the electrical curves, one can make inferences about what might actually be occurring as the nucleobase on the tip binds with the nucleoside on the surface and the complex is pulled apart. This information may be of use in designing future DNA sequencers.

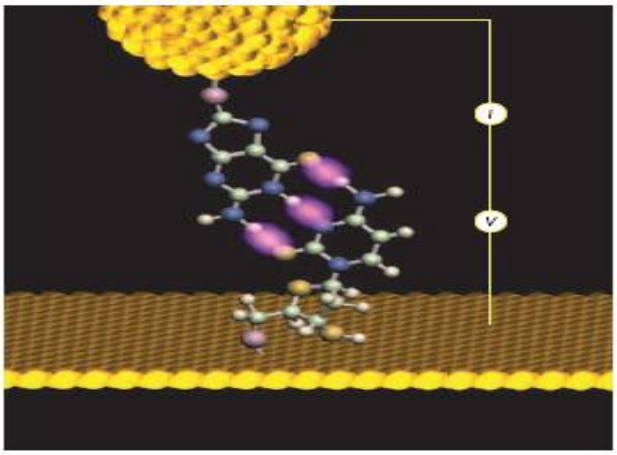

Figure 3.2. Picture of STM/AFM experiment. A gold probe with a nucleobase is brought into contact with a nucleoside surface and then retracted.[47]

3.1. CAFM measurements

3.1.1. Materials and methods

A picture of the experiment is shown in Figure 3.2. Gold on Mica substrates were received from Agilent Technologies (Chandler, AZ). They were annealed with a hydrogen flame to form clean <111> surfaces directly before assembly of nucleoside monolayers. Thymidine self assembled monolayers were created by first making a 1mM solution of 5'-S-acetyl-5'-thiothymidine in methanol, adding 10-20 drops of pyrollidine and allowing to sit for 1 hour to first remove the acetyl group from the molecule. After the hour, a freshly annealed gold substrate was left in the solution for another hour. The thymidine bonded as a monolayer to the gold surface through a thiol group at the 5' position of the sugar ring. After an hour, the substrates were rinsed with methanol to remove molecules that were not firmly bonded through the thiol linkage and were then dried with nitrogen.

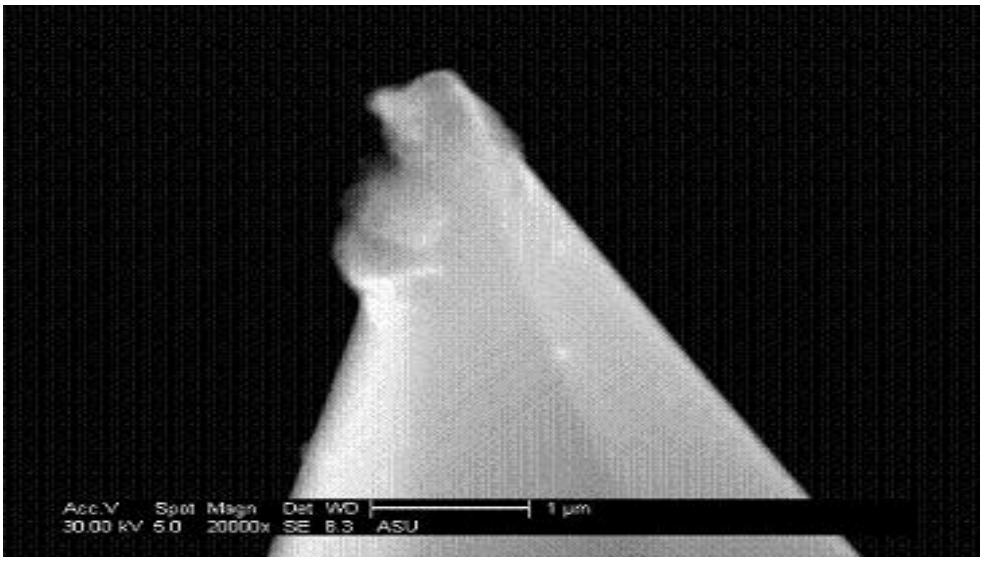

Figure 3.3. SEM image of AFM tip radius after metallic coating.

AFM tips used for CAFM experiments were from MikroMasch, (Tallinn, Estonia) and had reported spring constants of 0.35 N/m with triangular cantilevers. They were coated with an ion beam coater from Gatan (Pleasanton, CA) with chromium and gold in the following layers (25 Cr, 50 Au, 25 Cr, 50 Au, 25 Cr, 100 Au, 25 Cr, 300 Au). This layered structure of chromium and gold produces a more robust electrical coating on the AFM tips that is much less likely to peel off during measurements. The radius of curvature of a typical probe after coating was 100-200 nm and was measured by scanning electron microscopy (Figure 3.3). Probes were immediately transferred from the coater where they were held in vacuum to solutions of either 1 mM 8-mercaptoadenine or 2-amino-8-mercaptoadenine in dimethylformamide or 2 mM thiophenol in methanol for 2-12 hours. All molecules for tip functionalization were received from Sigma

Aldrich (St. Louis, Mo). Before use, the tips were rinsed in DMF and then methanol and dried in air or Argon.

All experiments were performed in 1,2,4-Trichlorobenzene solvent, which is a slightly polar but non-conductive solvent, in a Teflon liquid cell that had been cleaned with piranha (3:1 sulfuric acid: hydrogen peroxide). Functionalized tips were approached to the SAM surface using the Agilent PicoScan software on an Agilent PicoAFM microscope. After successful approach, custom labview software was utilized to maintain the tip at a current setpoint chosen by the user with a software PID controller. Upon withdraw, the servo was broken and the tip was retracted at a speed of 2,000 nm/s. Both current and cantilever deflection (from the AFM photodetector) were recorded through a breakout box on a Yokogawa DL750 Scopecorder oscilloscope, (Houston, TX) saved on the hard drive and transferred to computer files later.

After experiments, the spring constants of all tips were measured using the thermal noise method[48] on an Agilent PicoPlus microscope and a National Instruments PXI 6120 data acquisition card**.** Although tips are ordered at a given spring constant, they can vary by an order of magnitude from tip to tip within the same batch. Furthermore, the metallic coating of the AFM tip changes the spring constant (see Figure 3.4 (d))**.** For force curves to be accurate, therefore, the spring constant of every cantilever has to be measured. This is accomplished by examining the energy thermally dissipated in the cantilever while it is away from the surface. The deflection of the cantilever is measured with the AFM

photodiode for a given period of time at very high bandwidth (typically at least 10 times the resonant frequency of the cantilever). A power spectral density of the deflection trace is then measured and the area under the resonant frequency peak is determined. The sensitivity of the cantilever in V/nm is also determined by examining the contact region of a deflection approach curve on a hard substrate. These two values combined can give the spring constant of the cantilever through the following equation[49]

$$k = 0.8174 \frac{K_B T}{s^2 P} \left[\frac{1 - \left(\frac{3D}{2L} \tan\phi \right)}{1 - \left(\frac{2D}{L} \right) \tan\phi} \cos\phi \right]^2 \qquad 3.1$$

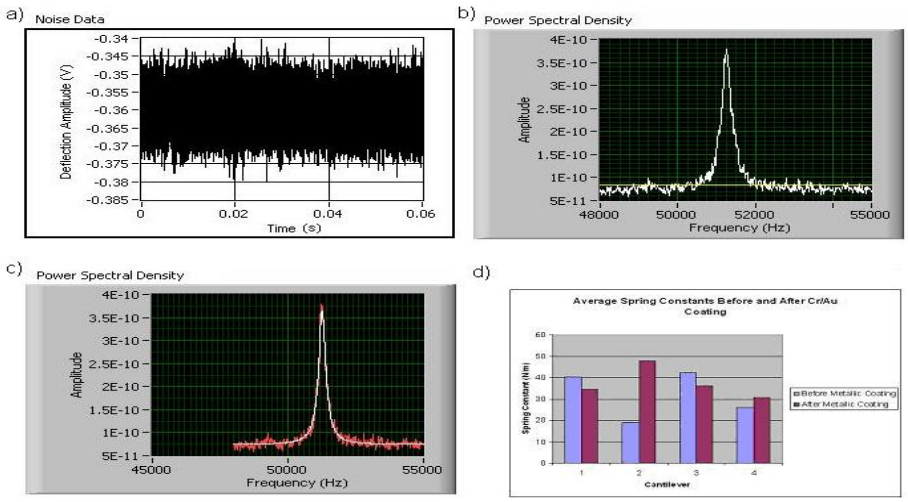

Figure 3.4. Procedure for obtaining cantilver spring constant. Cantilever deflection noise is recorded (a), followed by conversion to a power spectral density (b). Finally the resonant peak is fit with a lorentzian (c) in order to compute the area under the curve. This value, combined with the cantilever sensitivity is used in equation 3.1 to determine the spring constant. (d) shows the average spring constant values for several cantilevers before and after chromium and gold coating.

Where s is the sensitivity, P is the area under the power spectral density resonant peak and D, L and φ are geometric measurements of the cantilever typically obtained from the manufacturer. A custom labview program was created to better automate the thermal noise measurement and obtain spring constants for all cantilevers used in the experiments. Figure 3.4 shows the steps necessary to compute this spring constant.

Data was analyzed using custom labview analysis software. Deflection curves were translated into force curves in nN by using the measured spring constant and the sensitivity of the tip in V/nm as calculated from each individual force curve in the contact region. Figure 3.5 shows what a typical force retraction curve looks like, along with the simultaneously obtained current curve. The linear

region in the force curve occurs when the tip is in contact with the surface. As the tip moves away from the surface, recorded force decreases linearly due to the spring nature of the cantilever. The force becomes negative due to adhesion of the tip with the surface and finally breaks away to zero force by the end of the retraction. The minimum force value was calculated by the labview program and is referred to as the adhesion force. Similarly, for the current curves, the value of the current before withdraw and at F=0 are recorded by the labview software and are correlated with adhesion force.

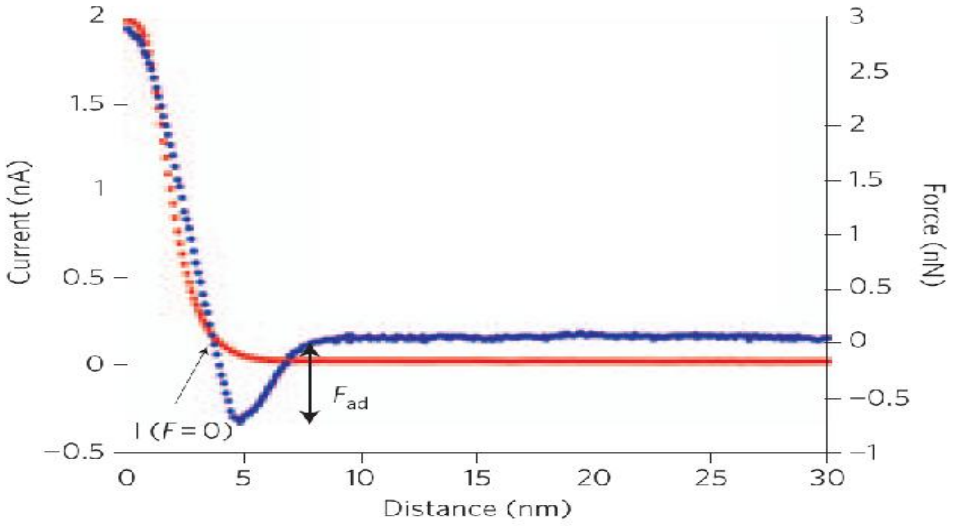

Figure 3.5. Typical force and current curve. The blue curve is the force while the red curve is the current. The two were obtained during the same withdraw and were recorded simultaneously. F_{ad} is the adhesion force felt by the tip during retraction.[47]

3.1.2. Relationship between force and setpoint current

The force of adhesion on a cantilever during retraction from a surface is due to a number of different factors. On a bare surface with a bare tip in a liquid

environment, the adhesion force is usually very small. In air, adhesion is significant due to a water layer that forms on the surface. In the case of the nucleosides, adhesion can be due to non-specific interactions between the molecules on the tip and the molecules on the surface and due to the binding between complimentary base pairs. Measurements for each functionalized tip were taken at several different setpoints, and for each setpoint, the average adhesion force and current at retraction were recorded. The current at the point of retraction slightly differs from the setpoint current since the PID controller is not very accurate and the current actually fluctuates considerably around the setpoint value. The retraction current and adhesion forces were plotted against one another. This plot is shown in Figure 3.6**.**

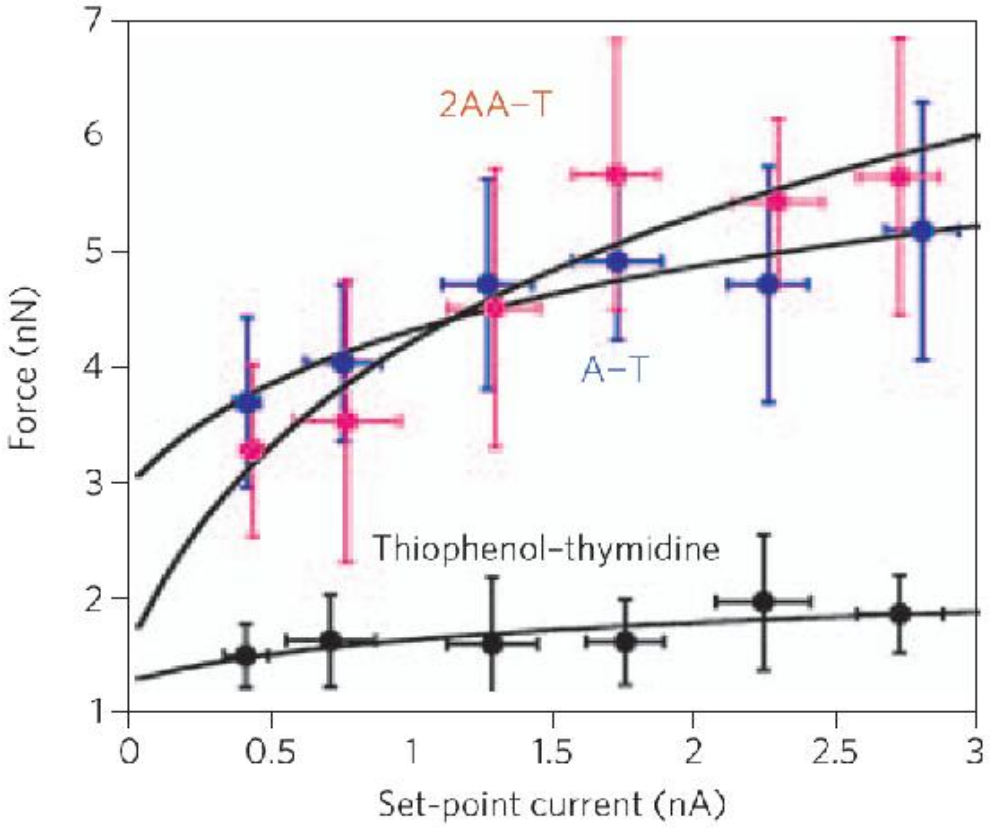

Figure 3.6. Plot of adhesion force versus the current at probe retraction. The surface was a monolayer of thymidine while the tips were functionalized with 2-aminoadenine, adenine or thiophenol.[47]

From Figure 3.6 it is clear that the adhesion force increases faster while using a 2-AA probe (which forms three hydrogen bonds with thymine) than with the A probe (which forms two hydrogen bonds with thymine). Both tips have much larger forces than seen with the thiophenol probe, which does not actually bind to the thymine. Since the thiophenol is similar in structure to the other molecules it is a good control as it will have similar non-specific adhesion to the SAM, without the bonding. The relationships are well-fitted with a natural logarithm, as shown in the figure.

The fit of the AFM data to a logarithm coincides with a multiple-molecule interaction model. The number of molecules in the interaction is strongly related to the contact area of the junction. From Hertz theory, the contact radius is related to the displacement of the probe by[50]

$$\delta = \frac{a^2}{R} \qquad 3.2$$

Where δ is the indentation of the probe, a is the contact radius and R is the radius of the probe. The tunneling current increases with the probe indentation, which leads to the following relationship

$$I = A(e^{b\delta} - 1) \qquad 3.3$$

Where A and b are both constants and the current is set to zero when there is no probe indentation. The number of molecules being probed, N, in any given retraction is proportional to the contact area at the setpoint, which means that it is also proportional to the current at the setpoint.

$$CN = \ln(BI_{SP} + 1) \qquad 3.4$$

Where, again C and B are constants. The adhesion force is then proportional to the number of hydrogen bonds, in addition to the nonspecific adhesion force. This leads to the following relationship for adhesion force and setpoint current:

$$F_{adhesion} \propto N_{HB} S_{HB} \ln(BI_{SP} + 1) + F_{NS} \qquad 3.5$$

In this case, N_{HB} is the number of hydrogen bonds per base pair interaction (2 for adenine-thymidine and 3 for 2-aminoadenine-thymidine), S_{HB} is the strength of each hydrogen bond and F_{NS} is the nonspecific adhesion which can be calculated

from the thiophenol control. This is the function utilized to fit the data in Figure 3.6, assuming that all hydrogen bonds are the same strength (5-7 kcal/mol).[51] In fact, the coefficients in front of the logarithm were fit for both A-T and AA-T. The ratio between the two coefficients was 1.92 (+0.7,-0.5) which is very close to the 1.5 expected from the ratio of hydrogen bonds (3:2) in each interaction.

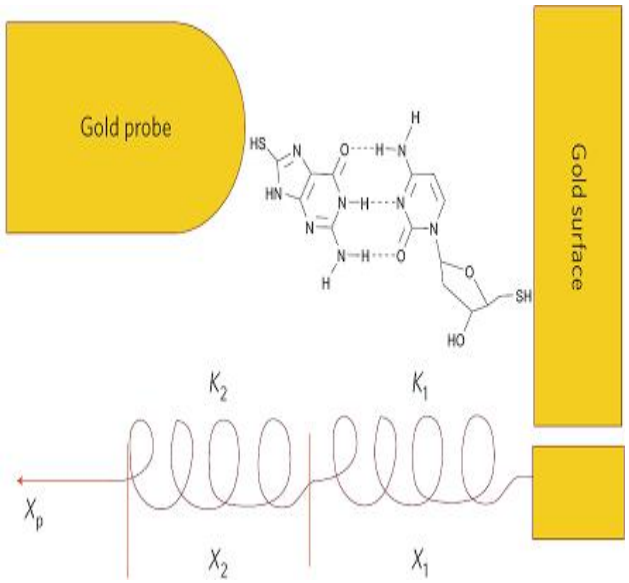

Figure 3.7. Schematic of the elastic-distortion model.[47]

This relationship, discovered from the conducting AFM data, has led to the elastic interaction model for the STM retraction curves. A schematic of the model is shown in Figure 3.7 and is valid for both the AFM experiment and the STM experiment. K_2 represents the stiffness of the probe-molecule bond, while K_1 represents the stiffness of a single hydrogen bond. X_1 is the distance of the tunnel gap, while X_P represents the external pull of the probe measured by voltage on the piezo. Changes in X_P actually results in smaller changes in X_1 due to the mechanical interactions of the junction. Since $X_P=X_1+X_2$, X_1 can be related to X_P by,

$$X_1 = \frac{K_2}{K_2 + K_G} X_P \qquad 3.6$$

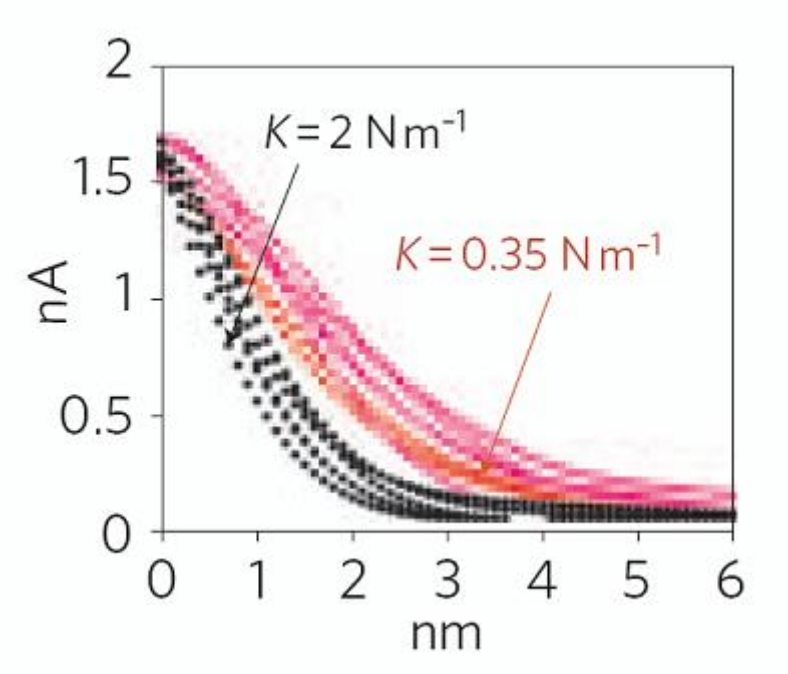

Figure 3.8. Decay curves for AFM cantilevers of different spring constants. The stiffer cantilever begins to approach the STM data[47]

Where K_G is the spring constant of the molecular gap, which is defined as the product of the number of formed hydrogen bonds and the stiffness of those bonds, K_1. This clearly explains why the STM tunneling curves decay so far. One would expect, then, that probes that are less stiff have even longer decays since K_2 would be dominated by the low probe stiffness. This is seen in comparing the AFM and STM withdraw curves. The AFM probe at k=0.35 N/m is much more flexible than the STM probe, and so the current retraction of the A-T systems extends further out to 4 nm as compared with the STM curve which extends out to 2 nm. This can be further examined with the conducting AFM by changing the spring constants of the probe. Figure 3.8 shows how going to a higher spring constant probe decreases

the extension of the current. A 2 N/m AFM probe begins to emulate the extension of the STM probe.

Since K_G represents the stiffness of the molecular junctions, which is directly proportional to the number of molecules being probed times the product of the number of hydrogen bonds per molecular interaction and K_1, the stiffness of a single hydrogen bond, then equation 3.6 can be rewritten as

$$X_1 = \frac{1}{1 + CN_{HB}K_1 / K_2 \ln(BI_{SP} + 1)} X_P \qquad 3.7$$

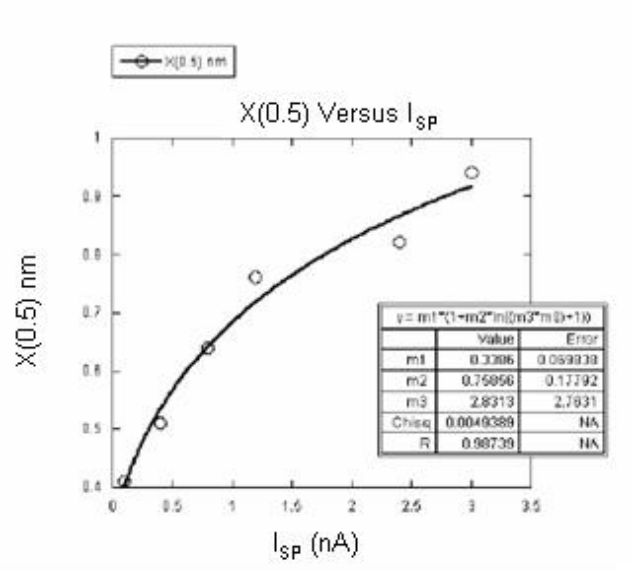

Figure 3.9. Elastic-distortion model coefficient fitting.[47]

The parameters needed to fit this model are CK_1/K_2 and B. These values can be readily obtained by taken a subset of the data at a particular decay value. For instance, the distance where the current falls by a factor of 2, $X_P(0.5)$, can be obtained from the data at a number of different setpoints, and CK_1/K_2, B and $X_1(0.5)$ can be fit accordingly **(**see Figure 3.9).

Equation 3.7 can be utilized to fit the STM current decay curves. First, an arbitrary function can be assigned such that

$$I(X_1) = I_{SP} f(\beta X_1) = I_{SP} f\left(\frac{\beta X_P}{1 + CN_{HB} K_1 / K_2 \ln(BI_{SP} + 1)}\right) \quad 3.8$$

Where β is the inverse decay length of the curves in solvent and f, again, is an arbitrary function equal to 1 at $X_1=0$ and 0 at $X_1=\infty$. If the function can be calculated given a set of X_P at a particular setpoint, then a simple change in coordinates will allow the function to be utilized for other setpoints by the following relation

$$X_P(I_{SP1}) = \frac{1 + CN_{HB} K_1 / K_2 \ln(BI_{SP1} + 1)}{1 + CN_{HB} K_1 / K_2 \ln(BI_{SP2} + 1)} X_P(I_{SP2}) \quad 3.9$$

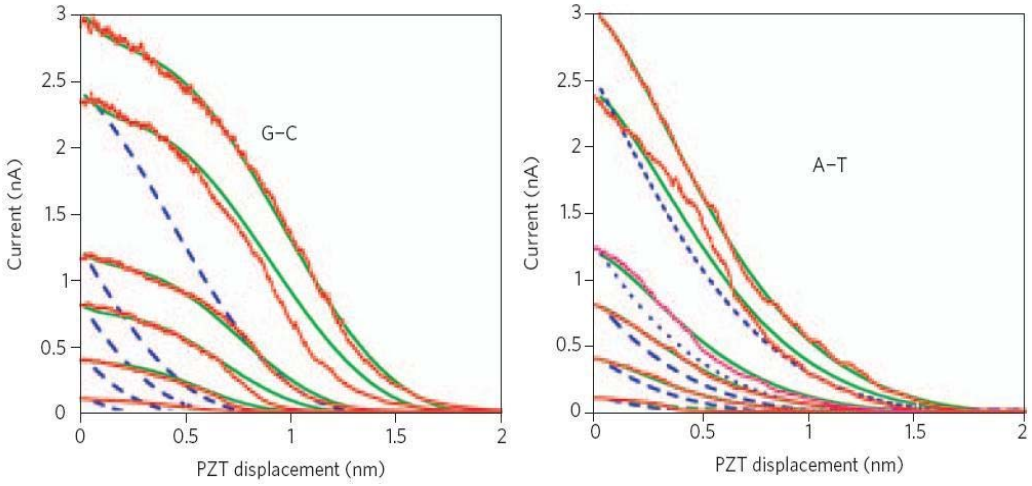

Figure 3.10. STM withdraw curves for G-C and A-T interactions. Dashed lines represent a polynomial fit for the 3 nA setpoint curve, while the solid lines represent the same polynomial fit, but using the elastic-distortion model to transform the displacement coordinate.[47]

Equation 3.9 can now transition coordinates to fit the STM decay curves properly. If a function can be found that can fit one of the curves starting at one setpoint, then the other curves can be fit with that same function by making the coordinate conversion in equation 3.9. This was accomplished for both the STM G-C

interaction and the A-T interaction shown in Figure 3.10. Both plots show several curves beginning at different setpoints. The dashed line is representative of a polynomial fit to the 3 nA setpoint curve used to fit all of the curves without coordinate change. The solid green line is the same polynomial fit with coordinate conversion from equation 3.9. Clearly, the solid green line is a much better fit to the data, giving evidence that this elastic-interaction model is a good representation of what is actually occurring in the measurement.

This elastic-interaction model was also used to fit STM data related to the charge transferred during tip retraction. The charge is found by finding the area under the retraction curve, which is equivalent to integrating the current as a function of time. With the arbitrary function in equation 3.8, this works out to

$$Q = \int_0^\infty I(t)dt = I_{SP}\int_0^\infty f\left(\frac{\beta v t}{1 + CN_{HB}K_1 / K_2 \ln(BI_{SP} + 1)}\right)dt \qquad 3.10$$

Where υ is the retraction speed of the probe. This, after substitution, works out as

$$Q = \frac{I_{SP}}{\beta v}\left(1 + \frac{CK_1}{K_2} N_{HB} \ln(BI_{SP} + 1)\right) \qquad 3.11$$

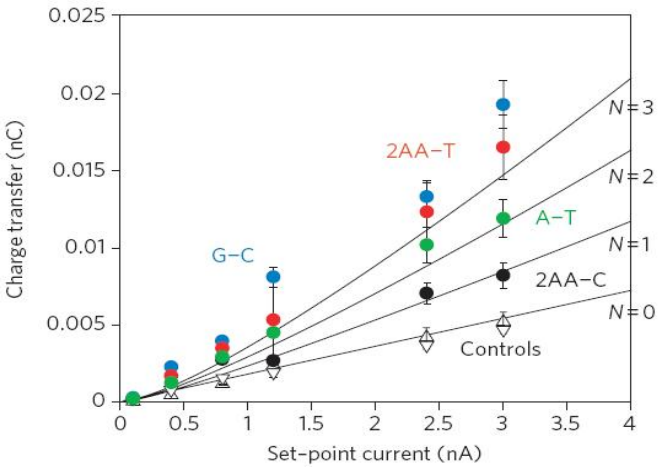

Figure 3.11. Elastic-distortion model fits to the STM charge transferred data.[47]

This formula was used to fit data on charge transferred versus setpoint current, and is shown in Figure 3.11. It is suspected that the small variations from this theory are due to the slight difference between hydrogen bond strengths between the different base pair combinations.

3.1.3. Calculations of molecular conductance

Figure 3.5 shows actual force and current curves obtained simultaneously in an A-T CAFM interaction. The point at F=0 in the retraction is shown by an arrow. This is, ideally, where the assembly has zero force applied, and would be the best point to measure a conductance value for the molecular junctions. One has to know, though, how many molecules are being probed in a given pull. This is easily read from the adhesion force value, minus the non-specific adhesion. In general, the AFM tip probed 2-10 molecules during a given retraction. Dividing this value by the force to break the molecular bonds, which is 600 pN for a 2AA-T pair and 400 pN for an A-T pair,[52] gives a good estimate for the number of molecules in any given pull. Based upon the number of molecules probed as calculated from the adhesion force and the current at F=0, it was found that the

average conductance of a single molecular nucleoside-base pair was between 100 and 300 pS. This was an order of magnitude lower than theoretical calculations (See Table 3.1) for nucleoside-base pairs, which is a standard discrepancy between molecular electronics theory and experiment.[26]

3.2. Conclusions

In this experiment, the conducting atomic force microscope was an important component in understanding the behavior of the mechanical and electrical interactions between nucleoside-base pair bonding and probe molecule interactions. The conclusion after AFM experiments was that the STM retraction curves do not represent single molecule measurements. Going back to previous STM experiments performed on DNA oligomers, it was noted that the base functionalized STM tip did not have the ability to distinguish blocks of nucleotides that were less then twenty in length. New understanding of the experiment explains the reasoning behind this lack of discrimination. Based upon this model, the STM tip was probing too many molecules to be able to accurately distinguish such a small block of bases.

The elastic-distortion model obtained after AFM results also explains why STM retraction curves have shapes that are dependent upon initial current setpoint, and why charge transfer depends strongly on this setpoint. Furthermore, the CAFM gave strong evidence that the conductance of these molecular junctions is very low, leading to the belief that the initial current setpoint is actually achieved through a through-space tunneling mechanism and not through

Base pair (N_{HB}) [Base-nucleoside]	Conductance base:base (nS)	Conductance nucleoside:base (nS)
C:G (3) [Cytidine:G]	83.8	0.96
T:2AA (3) [Deoxythymidine:2AA]	119	1.43
T:A (2) [Deoxythymidine:A]	22.2	1.62
T:G (2) [Deoxythymidine:G]	23.7	0.54

Table 3.1. Calculated conductances of base-base molecular junctions and base-nucleoside junctions.[47]

the bonds. The current setpoint does, however, affect the number of bonded molecules in each retraction, which leads to the extended decay length and increased charge transfer.

The final implications of these experiments relates directly into the creation of a device that can eventually sequence DNA by recognition electron tunneling. Clearly, from the AFM data, conductance in base-nucleoside junctions is very low. This is supported by theoretical calculations which show that base-nucleoside junctions have a conductance value that is an order of magnitude lower than similar base-base junctions. Furthermore, calculations show that the conductance differences between different nucleoside-base combinations is quite small compared to differences seen in base-base interactions (Table 3.1**)**. The sugar rings associated with the nucleosides clearly dominates the conductivity of the interaction. Adding a phosphate makes the conductance even lower. These results suggest that a single base may not be able to discriminate nucleotides coming out of a nanopore. Other readers or different schemes may be necessary in order to utilize molecular recognition tunneling in effective DNA sequencers.

4. ORGANIC PHOTOVOLTAICS

Another application of molecular electronics that is drawing more interest is within the field of organic photovoltaics. Traditional sources of energy in use today are mostly derived from non-renewable fossil fuel sources. These sources are in limited quantity and are often in politically unstable areas of the world. Furthermore, more evidence indicates that the burning of fossil fuels is contributing to global climate change. For these reasons, there is great interest in renewable and cleaner energy sources. One obvious and highly abundant source of renewable energy is solar energy, and there is much interest in harnessing the power of the sun with photovoltaic technology. The sun is a near-infinite source of energy, that, if converted properly, can provide society with the energy needed to move forward in 21st century. The current problems with solar energy, however, lie in lack of efficiency and cost.

Most photovoltaics currently utilize inorganic semiconductors like silicon to both absorb light and transport photogenerated current. With the latest technology in semiconductor processing and manufacturing, these devices can be made relatively efficient, but at great cost. For the most part, semiconductor solar cells available to the average consumer produce energy at a cost that is much higher than fossil fuel sources. For example, the United States Department of Energy (DOE) recently published that the levelised cost of energy for rooftop photovoltaics in 2008 was between \$0.20 and \$0.80 per kWh.[53] This is quite expensive compared to the average retail price of electricity in 2008, which was

$0.11 for residential consumers.[54] For this reason, research in organic molecules as photovoltaic materials has grown over the past few years. Organic molecules are utilized everyday for light energy conversion in plants, so it has been proposed that they can be used efficiently in organic photovoltaic devices, producing less costly solar cells. Although efficiency has remained an issue in organic photovoltaic research, the prospect of a less costly device has continued to spur more investigation in the field.

4.1. Photovoltaic energy conversion

There are two main processes occurring in the typical photovoltaic device. The device must first absorb light and excite electrons into higher energy states, and then those electrons must be transferred into electrodes. If wired in short circuit form, this produces a photogenerated current upon illumination. If the cell operates in open circuit design, this generates a photovoltage. The combination of short circuit photocurrent and open circuit photovoltage gives the maximum potential power that a solar cell can generate. Both the process of absorption and transport are critical to a solar cell's potential as a viable energy conversion device. If the cell does not efficiently absorb at high intensity solar wavelengths, then the cell has little utility. Furthermore, if those excited electrons are not able to be transported, they eventually recombine and the absorbed energy is lost. Balancing good absorption with good transport is a critical challenge in photovoltaic design.

4.1.1. Semiconductor photovoltaics

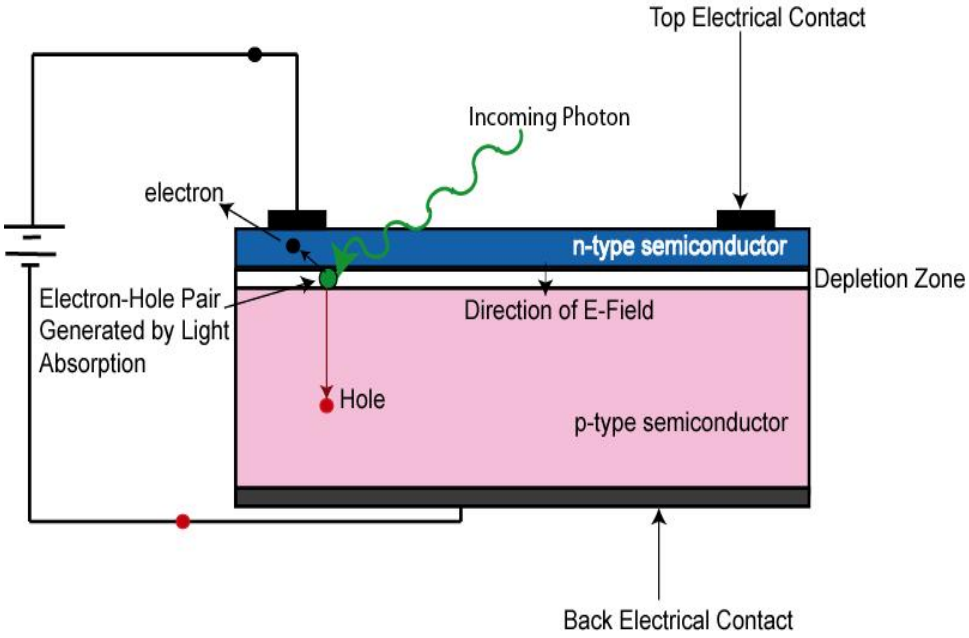

Figure 4.1. Schematic of a P-N junction photovoltaic device. A similar device can be made utilizing a P-I-N architecture.

Figure 4.1 shows a schematic of a traditional silicon photovoltaic cell. The cell operates as a P-N junction, with p-type semiconductor in contact with n-type. When the two types of materials are in close contact, holes from the p-type combine with electrons from the n-type and create a volume that is charge neutral and is referred to as the depletion region. An electric field exists in the region from the p-type to the n-type due to the difference in charge that is now separated by the length of the depletion region. When light is absorbed in this depletion region the electron and hole pair (the exciton) that is created is driven by the electric field to further separate into the respective types of semiconductor. In open-circuit configuration this creates a photovoltage, while in short circuit configuration, this creates a photocurrent. The equivalent circuit for this device is

shown in Figure 4.2 including both the shunt resistance and series resistance of the device.

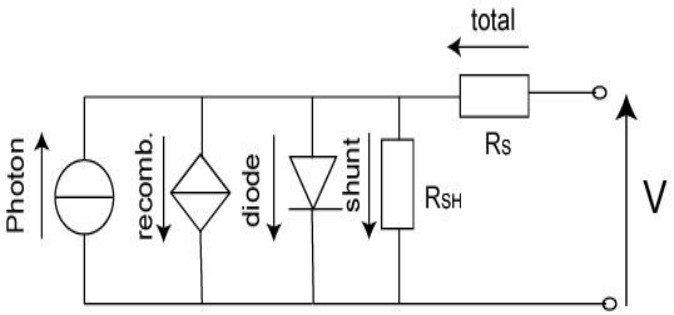

Figure 4.2. Equivalent circuit for a photovoltaic diode device.

Semiconductor photovoltaic cells are currently on the commercial market, available to both residential and industrial consumers. Many power companies even allow photovoltaics to be tied to the existing grid and buy any excess electricity that the consumer does not utilize. Although semiconductor photovoltaics are making headway in becoming larger-scale energy production sources, the drawbacks of their use currently stops many consumers from purchasing. The efficiency of a cell depends upon the quality and processing of the semiconductor, which is often proportional to the cost of the cell. This expense, compared to the low upfront cost of more conventional energy sources, can make consumers reluctant to purchase photovoltaics.

4.2. Benefits of organic photovoltaics

There are several different methods being utilized to both improve the efficiency of photovoltaic devices and bring their costs down. One promising method of producing low-cost photovoltaics is to utilize organic molecules as

light absorbers in a photovoltaic junction. At a very basic level, an organic solar cell consists of a layer of organic light-absorbing material sandwiched between one transparent electrode and another back electrode. As the organic absorbs light and creates excitons, these exitons would migrate to the electrodes and produce photovoltage or photocurrent. This type of scheme has several benefits and holds promise for future commercial devices.

The main benefit foreseen with utilizing organic materials for photovoltaic devices is in cost. If organic materials could be spin coated or self organized from solution onto electrodes, the cost of processing compared to the cost of semiconductor processing might be dramatically lower. The low cost of processing, alone, may make organic photovoltaics good competitors for semiconductor solar cells, even at lower efficiencies. Since much organic photovoltaic (OPV) research involves the processing of organics in low cost ways, this is clearly a goal for the OPV field.

Low cost processing is not the only potential benefit to organic photovoltaic research. Organic molecules are versatile materials, and thus can be changed and modified to suit different needs. Chemical variations in molecules change how they absorb light and this can be utilized to tune the absorption of the photovoltaic to the solar spectra in order to more efficiently capture available radiation. Bulk material flexibility is also seen as a potential benefit of OPVs. Unlike most inorganic semiconductor solar cells, organic thin films can be quite flexible and are usually easily prepared on a variety of substrates. This leads to

the idea that organic films can be made on flexible substrates, which may eventually lead to flexible photovoltaics. Since tradition semiconductor photovoltaics are typically rather rigid, they are limited in where they can be placed and how they can be transported. A flexible photovoltaic has many commercial applications and is a key potential benefit to organic solar cells.

4.3. Challenges to commercial organic photovoltaics

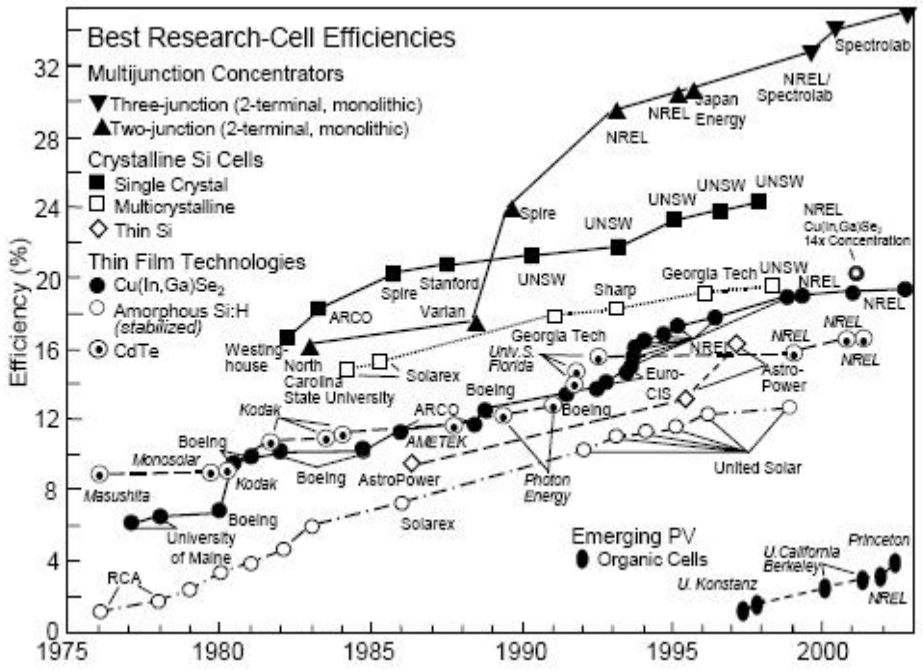

Figure 4.3. Best research cell efficiencies by type of solar cell and year.[55]

Although the benefits of organic photovoltaics certainly make them promising candidates for commercials solar cells, there are certain challenges that have and continue to keep them from large scale commercial markets. Most challenges in the design and fabrication of these photovoltaics is centered around the low efficiencies of such devices. Figure 4.3 shows the efficiencies of different types of research solar cells versus the year that the efficiency was determined.

Clearly, the graph shows that organic photovoltaics are among the lowest efficiency devices. Figure 4.4 gives a schematic that explains the different processes that occur in a typical organic device and is a good representation to explain why efficiencies in organic photovoltaics are traditionally very low. Every photon that gets absorbed by the film leaves an electron in a higher energy excited state and a hole. In order to produce photocurrent or photovoltage, this electron and hole pair need to travel to their respective electrodes, which are determined by the electronic work functions. The efficiency of the device can be determined by the rates of carrier transport minus the recombination rate.

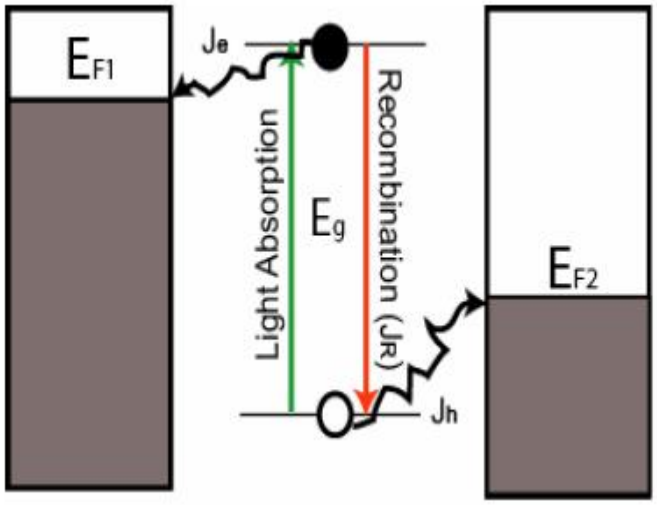

Figure 4.4. Energy diagram of organic photovoltaic device.

Unfortunately, in most organic devices the rate of absorption is small (organic molecules typically have absorption cross sections on the order of $Å^2$), while the rate of recombination is relatively high. Combined with low mobilities (as low as 10^{-4} $cm^2/(V*s)$ for electron and hole mobilities for some polymer-fullerene blends discussed later in the chapter)[56] which limit the rate of particle capture by the electrodes, and the

efficiencies of these devices turn out to be low. Exacerbating the problem is the fact that most changes that can improve one part of the efficiency equation tend to negatively affect the other parts. For example, increasing the thickness of the organic layer does increase the amount of light being absorbed, but a fewer percentage of the excitons generated get to the electrodes. This is because excitons must diffuse to the electrodes. The diffusion length before recombination of excitons in typical organic film is on the order of 5-20 nm.[57-60] So, a film that is any thicker than 20 nm does not collect all the generated excitons due to charge recombination. Decreasing the thickness of the film increases how many excitons make it to the electrodes, but obviously decreases the amount of light absorbed. So beneficially changing this rate equation in significant ways requires more sophisticated methods.

4.4. Organic photovoltaic architecture

As previously mentioned, organic photovoltaics suffer from low efficiencies that are a result of competing factors in the rate equation that determines efficiency. There have been numerous methods to increase the efficiency that go beyond simply changing the thickness of the organic layers, which, as mentioned, can only affect efficiencies by a very limited amount. For this reason, several more sophisticated methods of producing more efficient organic photovoltaics have been utilized with some success, although efficiencies, and practicalities in some cases, have meant that these breakthroughs have not been incorporated into commercial solar cells to date.

4.4.1. The Gratzel electrochemical cell

One exceptional improvement on the organic photovoltaic came in 1991 with the creation by O'Regan and Gratzel of an organic electrochemical photocell.[61] A schematic of a typical Gratzel cell is shown in Figure 4.5**.** The original Gratzel cell utilized nanoporous TiO_2 on top of sheets of conducting glass. The TiO_2 was then exposed to an organic dye which adsorbed onto the surface. The resulting TiO_2 was able to absorb up to 46% of incident solar light. The dye-sensitized TiO_2 was then put into contact with an electrolyte solution such as iodide/triodide which was in contact with another transparent electrode, like ITO. In this solar cell configuration, when the dye absorbs light, it injects the excited electrons into the TiO_2, leaving the dye positively charged. The electrolyte can then quickly donate an electron to the dye leaving it neutral, and leaving the electron permanently injected into the TiO_2. The ITO then donates an electron to the electrolyte ion in the solution. By connecting the TiO_2 through a load to the ITO in contact with the electrolyte, the circuit can be completed and power generated.

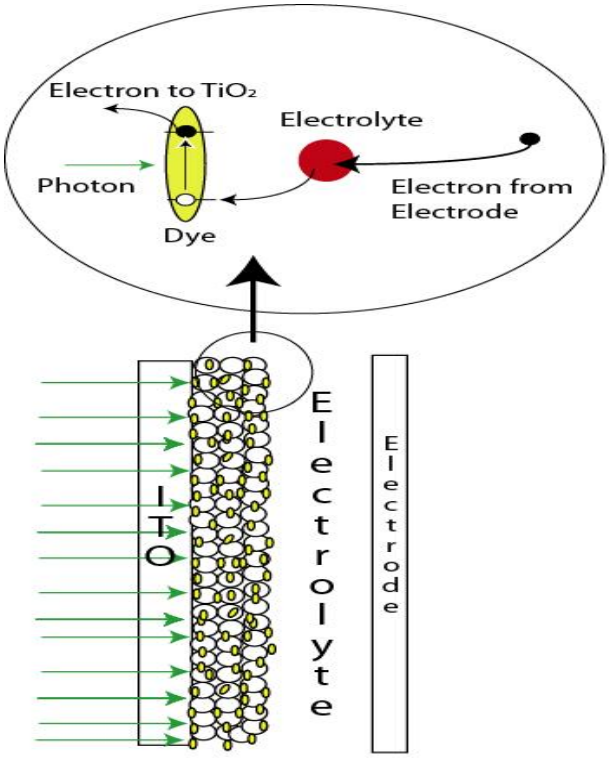

Figure 4.5. Gratzel electrochemical photocell

This solar cell scheme gets around some of the typical problems with many OPV devices. There is no need, for instance, for the exciton to diffuse within the organic, since the electron can immediately inject into the TiO_2 and the hole can be filled by the dye being in constant contact with the liquid electrolyte. Rates of electron and hole transfer increase without changing the amount of absorbed light. In addition, the nanoporous TiO_2 provides a very high surface area electrode, allowing for more organic dye to absorb onto the surface. This, then, increases the absorption of the device, without creating a thick, non-conducting organic film. Originally these cells had efficiencies from 7.1%-7.9%,[61] which, amazingly, is still higher than thin film organic photovoltaic devices. Current research in Gratzel-type cells has led to photovoltaics achieving up to 10.6% efficiency.[62] Gratzel cells, unfortunately, do suffer from difficulties in practical application. They currently require a liquid electrolyte in order to operate. This necessity has made it impractical to use in any significant way as a photovoltaic device. A breakthrough in electrolyte

technology to create an efficient semi-solid electrolyte may lead the way into bringing Gratzel cells into commercial use, and some research in this area appears somewhat promising.[63]

4.4.2. Heterojunction organic photovoltaics

The Gratzel cell gets around some of the problems with recombination by providing a simple pathway for excited state electrons to be donated directly into a semiconductor. Getting the electron away from the excited state light absorber is an essential component in efficient OPV devices. Another method of accomplishing this is to utilize molecular donors and acceptors within the same organic device. By having them close to each other in the same device, light absorbers can quickly donate electrons into the acceptors, slowing the rate of recombination and increasing the chance of extracting charges more efficiently.

This donor-acceptor scheme has had particular success when utilizing a polymer like regioregular poly(3-hexylthiophene) (P3HT) or poly(2-methoxy-5-(2'-ethyl-hexyloxy)-1,4-phenylene vinylene) (MEH-PPV) as the light absorber/electron donor, and the fullerene derivative, phenyl-C_{61}-butyric acid methyl ester (PCBM)[64] as the electron acceptor. The absorber and the fullerene are typically blended together and spin coated onto an ITO substrate pre-coated with Poly(3,4-ethylenedioxythiophene) :poly(styrenesulfonate) (PEDOT-PSS). Efficiencies in the 3-6% range have been achieved by several different groups utilizing this method.[65-67] Since charge transfer occurs at the interface between molecules in solid form, this means that there is no need for a liquid electrolyte.

It has been found, however, that interfacial properties are very important for efficient solar cell devices using this architecture. Cells work best when the donor and acceptor form separate domains that are roughly the same size as the exciton diffusion length. There exist multiple ways to control these domains, from choosing the appropriate spin-cast solvent, to annealing the device.[68] The simple methods of fabrication, ability to perform charge transfer without electrolytes and efficiencies that are much higher than cells made out of single molecular absorbers have spurred much interest in this technique.

4.4.2. Utilization of inorganic nanostructures

With ever-increasing knowledge of the construction of inorganic nanostructures, some groups have begun to utilize them in order to increase the efficiencies of organic photovoltaics. Many inorganic materials are excellent electron acceptors which, when paired with complimentary organics, can increase the rate at which excitons diffuse to electrodes. One way to incorporate inorganic materials is to blend inorganic nanostructures with organic light absorbers, much the same way that fullerene is blended with light absorbing polymers in the bulk-heterojunction solar cell. In some cases, even the inorganic nanostructure can be utilized with the organic to absorb light and capture more of the solar spectra.

Huynth et al. utilized this method of blending inorganic nanostructures with organic materials by synthesizing CdSe nanorods in solution and mixing them with the polymer P3HT.[69] CdSe is a semiconductor material and its absorbance spectra can be tuned by altering the bandgap of the structure which, in

this case, is accomplished by changing the dimensions of the nanorods. The energy levels of the system are such that excited state electrons from the P3HT can be readily transferred into the CdSe, while holes from the CdSe can hop to the P3HT. Recombination is, therefore, more limited in such a system. Efficiencies as high as 1.7% under Air Mass (A.M.) 1.5 Global solar conditions have been achieved utilizing this method, again, without the need for liquid electrolyte. Several other systems have been researched blending inorganic nanostructures with organic light absorbers with some success.[70,71]

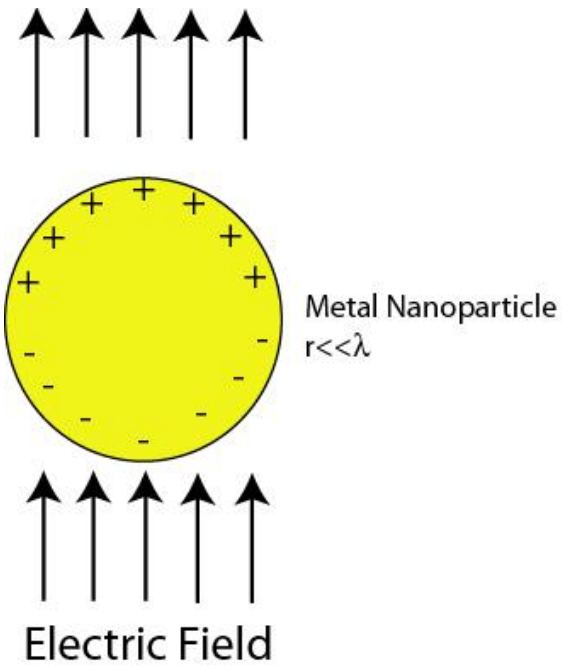

Figure 4.6. Schematic of metal nanoparticle in an electric field. Charges will oscillate as the electric field oscillate, creating a surface plasmon.

In addition to being good electron acceptors, some nanostructures are believed to actually alter the absorbance of organic molecules. Metal nanoparticles, specifically, have a unique property known as surface plasmon resonance. In the presence of an electromagnetic wave, the electrons in a metal nanoparticle will oscillate with the changing electric field (Figure 4.6**)**. This oscillation of charge around the surface of the nanoparticle creates its own

electromagnetic field as it becomes an oscillating dipole. The wavelength at which the nanoparticle will absorb light strongly is given by the classical electrodynamics expression for the polarizability of the nanoparticle with volume V and relative dielectric constant of ε_r

$$\alpha = \varepsilon_0 3V \frac{\varepsilon_r - 1}{\varepsilon_r + 2} \qquad 4.1$$

Clearly, this quantity gets very large as the relative dielectric constant approaches -2. For most metals, this occurs in the visible wavelength range. For instance, gold nanoparticles appear very red in color because their plasmon absorption is around 520 nm.

This re-radiation of incident light is what makes metal nanoparticles potentially useful components in organic solar cells. As discussed, most organic light absorbers have very low absorption cross sections (on the order of $Å^2$) which, coupled with the low rate of electron transport, typically hampers the efficiency of organic solar cells. If metal nanoparticles can increase the intensity of the electromagnetic fields, it is possible that they could increase the absorption of organic molecules in these higher intensity fields. There have been several reports of metal nanoparticles enhancing the fluorescence or organic molecules[72,73] and even some reports that metal nanoparticles increase the absorption and efficiencies of organic photovoltaic cells.[74,75] The physics of surface plasmons and their effects on organic fluorophores are still not completely understood however, and more research into what actually happens when an

organic light absorber is placed in close proximity to metal nanoparticles will no doubt help illuminate ways to utilize these particles most effectively.

4.5. Porphyrin based molecular dyads and triads

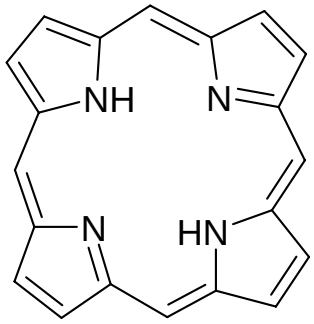

Figure 4.7. Chemical structure of porphine

Another interesting potential way to circumvent the problem of recombination in organic films is to create covalently bonded molecular donor-acceptor assemblies that increase the molecular excited state lifetimes. In this direction, much research has been conducted examining the possibility of utilizing porphyrins connected to different acceptors and donors as photovoltaic elements. Figure 4.7 shows the chemical structure of porphine, the main component of all porphyrins. In a porphyrin, four pyrrole rings (cyclical groups that contain nitrogen) are joined together by single carbon atoms to form a larger heterocyclic ring. The conjugated nature of the molecule allows it to absorb visible light quite strongly. A spectra of a porphyrin molecule (tetratolyl-porphyrin) is shown in Figure 4.8**.** The strongest absorption band (around 416 nm) is known as the Soret band, and the other bands between 500 and 800 nm are referred to as Q-bands. Porphyrins are naturally found in several different biological processes. The unbonded electrons in the nitrogens can ligate a metal ion, and this feature is utilized in hemoglobin, which is a molecule that binds to iron in the blood. More relevant to

solar cells, however, is the fact that porphyrins are utilized within chlorophyll molecules as light absorbers in photosynthesis.

Since porphyrins are utilized as light absorbers in photosynthesis, it is natural to believe that they could be used to absorb light in an organic photovoltaic. However, porphyrin based photovoltaics suffer the same problem of rapid exciton recombination that all organic photovoltaics suffer. In order to reduce the rate of recombination, some groups have researched ways to covalently attach electron and hole acceptors to porphyrins in order to increase the lifetime of the charge separated state, hoping to extract the charges more efficiently. A common electron acceptor utilized in these molecules is fullerene. When attached to a porphyrin (see Figure 4.9**)** the assembly can be referred to as a porphyrin-fullerene dyad. Due to the energy levels of the porphyrin and fullerene (the excited electron in porphyrin is at 1.90 eV compared to the lower 1.74 eV excited singlet state of the fullerene)[76] the porphyrin, upon absorbing light, readily donates its excited electron to the fullerene. When the porphyrin is able to transfer the electron to the fullerene, the excited state lifetime

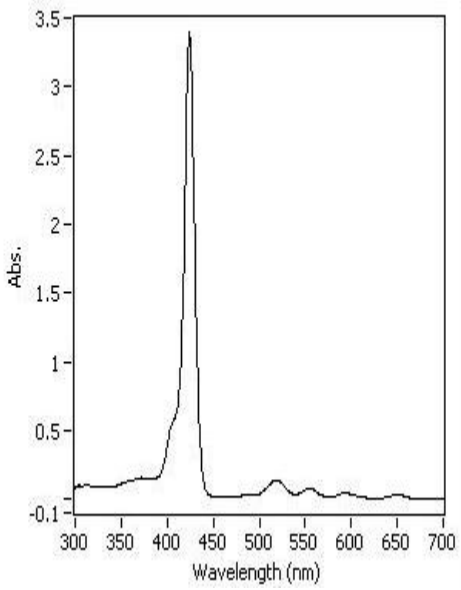

Figure 4.8. Absorbance spectra of tetratolylporphyrin

of the free base porphyrin-fullerene dyad extends from 20 ps to 290 ps.[76] Further, a carotenoid can be added which accepts the hole from the porphyrin, leaving the porphyrin neutral after donating an electron into the fullerene. This type of structure is referred to as a molecular triad and the charge separated state of a molecule like this can exist for up to 1500 ns.[77]

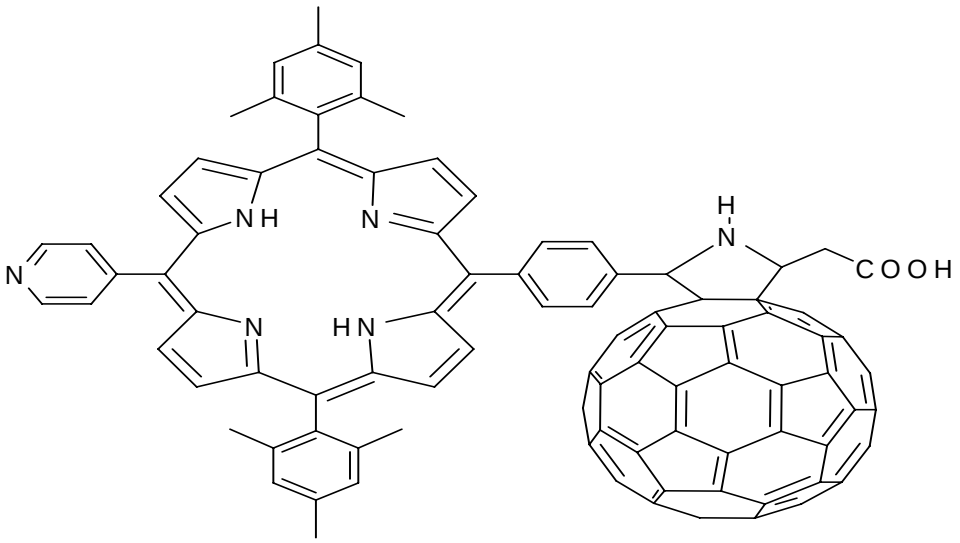

Figure 4.9. Chemical structure of a porphyrin-fullerene dyad molecule.

This fast electron transfer from porphyrin to fullerene (the rate constant is 1.8×10^{11} s^{-1} for the free base porphyrin-fullerene dyad in benzonitrile)[76] mimics observations in photosynthesis. Soon after chlorophyll absorbs light, the excited state electron undergoes electron transfer from one compound to another, preventing it from recombining so that the energy can be utilized by the cell. In this way, photosynthetic organisms are able to extract energy from the sun and turn it into useful chemical energy which, in one way or another, sustains almost

all life on the planet. Nature has clearly found a way to utilize solar energy efficiently and mimicking this pathway may lead to advances in solar energy that allow humans to utilize the sun for some of their present energy needs. Research in molecular structures such as porphyrin-fullerene dyads may lead to breakthroughs in solar cell technology, and potentially give insight into the chemistry and physics of these photosynthetic pathways.

5. ILLUMINATED STM FOR SINGLE MOLECULE CONDUCTANCE

As discussed in the previous chapter, organic photovoltaics severely suffer from recombination losses after the organic layer absorbs incident light energy. Porphryin-fullerene dyads (see Figure 4.9) are currently being examined as potential absorbing materials, due to their relatively long electronic excited state lifetimes, which may prove to be a beneficial feature in photovoltaic applications. Although there has been much research conducted on the spectroscopic properties of these molecules,[76] information on how these molecules conduct electricity at the single molecule level, both in the dark and under illumination, may help to shed light on how these molecules would perform in a photovoltaic device.

The STM break junction method (see chapter 1) is an ideal way to measure the electrical behavior of these dyads at the single molecule level. Furthermore, by outfitting the instrumentation with various optical components, the electrical behavior of the molecules can be recorded under both dark and illuminating conditions, allowing for the examination of the molecular conductivity. To better understand these molecules, a laser-illuminated STM system was constructed and the conductance of a porphyrin-fullerene dyad was measured both in the dark and under monochromatic illumination within an absorption band of the molecule. The following chapter outlines the instrumentation for this system and concludes the results of measuring the conductivity of a porphyrin-fullerene dyad.

5.1. Illuminated STM instrumentation

Figure 5.1 shows both a picture and a schematic of the illuminated STM apparatus used to measure the conductivity of the porphyrin-fullerene dyads. Several changes needed to be made to an existing scanning probe microscope to incorporate an illuminating element in order to measure molecular conductivity under laser illumination. In this section, the scanning tunneling microscope will be described, along with the optical components needed to incorporate the illumination and the environmental controls that needed to be modified in order to keep the system in an oxygen-free environment.

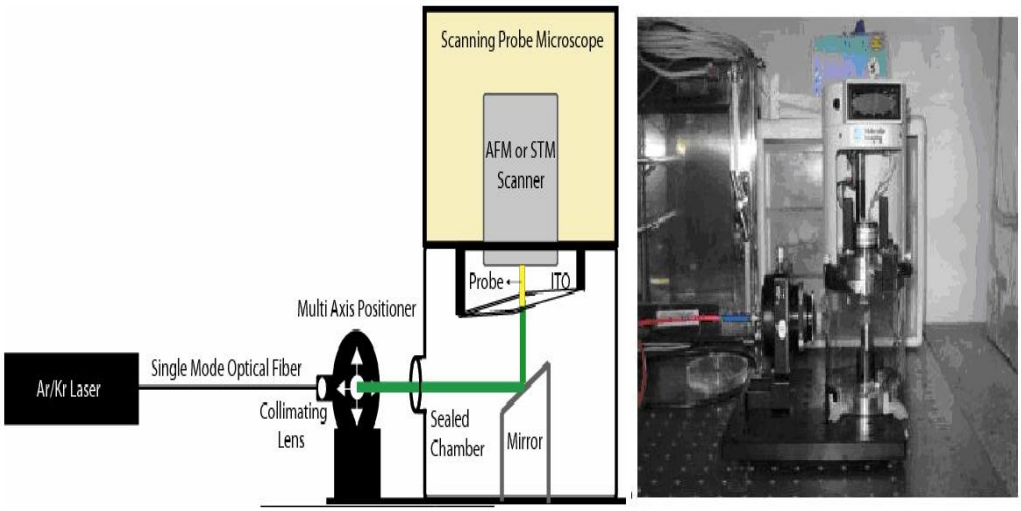

Figure 5.1. Schematic and picture of illuminated STM system. On the left is a schematic representation and on the right is a photograph of the actual instrument.

5.1.1. STM

The STM system utilized in these experiments was a Agilent PicoSPM. This scanning probe instrument has both AFM and STM capabilities.

Measurements involving illuminated CAFM (utilizing the same illumination instrumentation) will be described in the next chapter. An STM scanner with a 1 nA/V current preamplifier was used for all dyad break junction measurements. Initial scanning of surfaces was performed using Agilent PicoScan software. The head electronics of the microscope were connected to a signal breakout box (Agilent) for data recording and signal manipulation purposes.

5.1.2. Laser beam delivery

The samples (porphyrin-fullerene dyad monolayers on ITO) were illuminated with an Ar/Kr laser (CVI Melles-Griot, Albuquerque, NM) which could operate in the following wavelengths: 476 nm, 483 nm, 488 nm, 496 nm, 514 nm, 520 nm, 568 nm, 647 nm, 676 nm. The diameter of the beam from the laser head was 0.7 mm, and the maximum power available at different wavelengths was tens of milliwatts. The beam was launched into a single mode optical fiber using a laser-to-fiber coupler with an achromatic lens for focusing onto the 3.5 um fiber core (CVI Melles-Griot, Albuquerque, NM). The coupler was adjusted to maximize power output from the other end of the single mode fiber. Single mode fibers were utilized due to their small core diameters which allows for smaller beam diameters after collimation from the other end of the fiber. The use of single mode fibers leads to losses in power, but this does not negatively impact experiments, as will be discussed in later sections.

The fiber was 2 meters long and was terminated in an adjustable fiber collimator (Thor Labs, Newton, NJ). The fiber collimator contained an aspheric

lens with an estimated focal length of 4.6 mm which could adjust along the optical axis. An adjustable collimator was chosen to correct for any changes in the wavelength of the laser. The lens was positioned to collimate the light exiting the fiber with the smallest amount of divergence in order to minimize error in beam diameter and thus illumination intensity. At the sample the beam diameter was 0.48 mm.

The collimator was screwed into a multi-axis lens positioner (Newport Corporation, Irvine, CA) which was bolted down onto a small aluminum breadboard (Thor Labs). The multi-axis lens positioner had adjustment in the x, y and z direction. The x and y directions were used to locate the laser beam under the STM tip. The z adjustment can be utilized in future experiments for focusing the beam to tighter spots on the sample. A 0.3 optical density neutral filter was placed in front of the multi-axis lens positioner for these measurements in order to get a very low illumination intensity. A controllable optical shutter (Thor Labs) was placed in front of the filter and could block the beam or allow the light to pass through depending upon the applied voltage on the shutter (determined by a separate controller).

Also attached to the aluminum breadboard was an environmental chamber (explained in next subsection) into which the STM could be sealed. The laser light was directed through the environmental chamber to a silver 45º mirror (Thor Labs) which reflected the light to the sample. The sample holder was a standard

Agilent Pico STM sample holder, with a hole underneath the sample to allow the reflected light from the mirror to reach the sample.

5.1.3. Environmental control

Porphyrin and other light absorbing organics can be very sensitive to the presence of oxygen and can undergo irreversible photo damage. For this reason, it was critical for experiments to be conducted in as oxygen-free an atmosphere as possible. The experiments explained in this chapter were all performed in a sealed environmental chamber, which had been purged with Argon gas prior to recording data. To accomplish this, the glass from a cylindrical Agilent PicoSPM environmental chamber was removed from its stainless steel base, and replaced with a custom glass piece with a puckered hole. The hole (about 1″ in diameter) was covered with an optical window (Thor Labs) where the laser light could transmit through into the chamber with minimal scattering losses. A hole was screwed through the stainless steel base in order to bolt the entire environmental chamber onto the aluminum breadboard. A stainless steel ring was attached to the top of the glass, and the STM could seal onto this ring with the sample and tip securely sealed in the chamber. The base of the chamber contained gas inlet and outlet valves that could be sealed once purging was complete. The entire breadboard could be lifted and set onto a brick hanging from bungee cords in an electrically shielded chamber to prevent both mechanical and electrical noise.

To further reduce the effects of oxygen in the tip-sample junction, measurements were performed in liquid environment. Mesitylene, a

nonconductive solvent, was utilized for these measurements. Nonconductive liquids are ideal for STM work since the metal tip (wire) is immersed in the liquid during measurement. In order to utilize a conductive solvent, all but the very end of the tip must be insulated with wax or polyethylene. The mesitylene was bubbled with nitrogen or argon prior to use to remove any oxygen dissolved in the solvent. The solvent was contained in a Teflon liquid cell held above the substrate with spring clamps.

5.2. Illuminated single molecule experiment design

5.2.1. STM breakjunction experiment

The dyad samples were made prior to the experiments by immersing ITO that had been cleaned with 5 minutes exposure to oxygen plasma in a solution of 5 uM porphyrin-fullerene dyad in mesitylene overnight and lastly rinsing with mesitylene and drying in nitrogen. The porphyrin-fullerene dyads in this experiment are shown in Figure 4.9. They contain a carboxylic acid on the fullerene which can attach to the ITO, and a pyridine group on the porphyrin which can attach to a gold STM tip. These molecules were prepared by the Gust-Moore group at ASU.

The dyad STM breakjunction experiments were controlled by a labview program and a National Instruments data acquisition device (NI USB-6221). Measurements were taken at -0.4 V sample bias. The negative sample bias is used in order to facilitate bonding of the pyridine to the gold STM tip (positive relative to the sample). Picoscan software was first utilized to approach the tip to

the surface and an image of the surface was taken in order to determine the quality of the tip and the surface. The Picoscan servo was turned off and the labview program took control of the tip through an external z-position input on the STM controller. The tip was held at a user-determined setpoint value above the sample for a short period of time using a software PID controller which read the current through the data acquisition device. The PID control was broken after a set time and the tip was retracted and then re-approached to the surface where it was held under PID control again. This process would be repeated multiple times at several different places on the surface.

Data was recorded on a Tektronics TDS 2004B oscilloscope which recorded current, piezo voltage, bias and optical shutter voltage. Once a set of data for one withdraw was recorded on the oscilloscope it was immediately transferred via USB cable to a computer where it was added to an open file through another labview program. The entire process to withdraw the tip and record the data took approximately 10 seconds, so a typical experiment of about 6 hours could collect as many as 2000 curves.

5.2.2. Illumination

Since the molecules are thought to be prone to irreversible photo damage, it is important to understand whether any changes in conductance of the single molecules are due to illumination or photo damage. A single sample, therefore, needed to be measured in both the light and the dark during the same experiment. To accomplish this, the optical shutter controller was set to automatically open

and close every ten minutes. To track which data were taken with the shutter open and which data were taken with the shutter closed, a signal line from the voltage output on the shutter controller was connected to the oscilloscope. Every recorded curve also recorded the voltage on the shutter, which could be used in data analysis in order to determine whether the sample was illuminated or not during a given tip retraction. In this way, the same part of the sample can be probed under illumination and dark conditions automatically, and the reversibility of any changes in the molecules examined.

5.2.3. Data analysis

A labview program was created in order to analyze the break junction data. Chapter 1 explains that when a molecule is trapped in the tip-surface gap during withdraw, a step/plateau is observed in the current versus distance retraction curve. When the current curves that have steps in them are compiled into a conductance histogram, peaks appear that represent the molecular conductivity of the molecules being studied. This works well with very simple molecules, like alkanethiols, on a gold surface with a gold tip. Conductance peaks in such a system are very clear and easy to characterize as can be seen in Figure 1.12.

The gold tip-dyad-Indium Tin Oxide system, however, is a much more complicated experiment. Unlike the gold-thiol bonds, carboxylic acid-ITO bonds are not as well defined. Changes in bond formation can lead to heterogeneity in the conductance of the molecules. This can lead to wide conductance peaks that

are difficult to interpret if the analysis is completed by simply compiling all curves that have plateaus. For this reason a different data analysis program was utilized in order to better interpret the data.

One way to differentiate peaks from noise is to remove the sloping background from conductance histograms. The curves are essentially exponential decays, so a current versus time curve has more data points at low current. When these curves are compiled into a single histogram, it leads to significant sloping effect, where very low conductance values have very high counts in the histogram. This can make it difficult to read peaks that may be lower in conductance. In order to remove the background of the histograms, it is beneficial to only compile the points within the step/plateau, and not the rest of the curve.

This step analysis was completed with a labview program that created a "window" of a user-specified number of data points that was automatically "slid" over the entire decay curve, point by point. In order to determine if a step occurred within the window of data, a histogram of the data in the window was produced. Since this histogram is also a histogram of a decay curve, it decays in a similar way as the entire decay curve. The histogram is then automatically analyzed by the software. The maximum and minimum count values in the window are determined. If the difference between the maximum value in the window and the minimum value in the window is determined to be above a user-selected threshold, and the maximum occurs in the middle of the window, then

the position of the maximum value is assigned a single count. This procedure eliminates the exponential decay background that exists when creating a histogram from complete curves, since the count will only be assigned if the maximum occurs in the middle of the window. This produces histograms that have zero counts at zero conductance, and peaks in the conductance histograms are much more readily analyzed. This procedure has been previously reported in determining the conductance of oligoalanine.[78]

5.3. Illuminated single molecule conductance results

5.3.1. Conductance of illuminated dyads

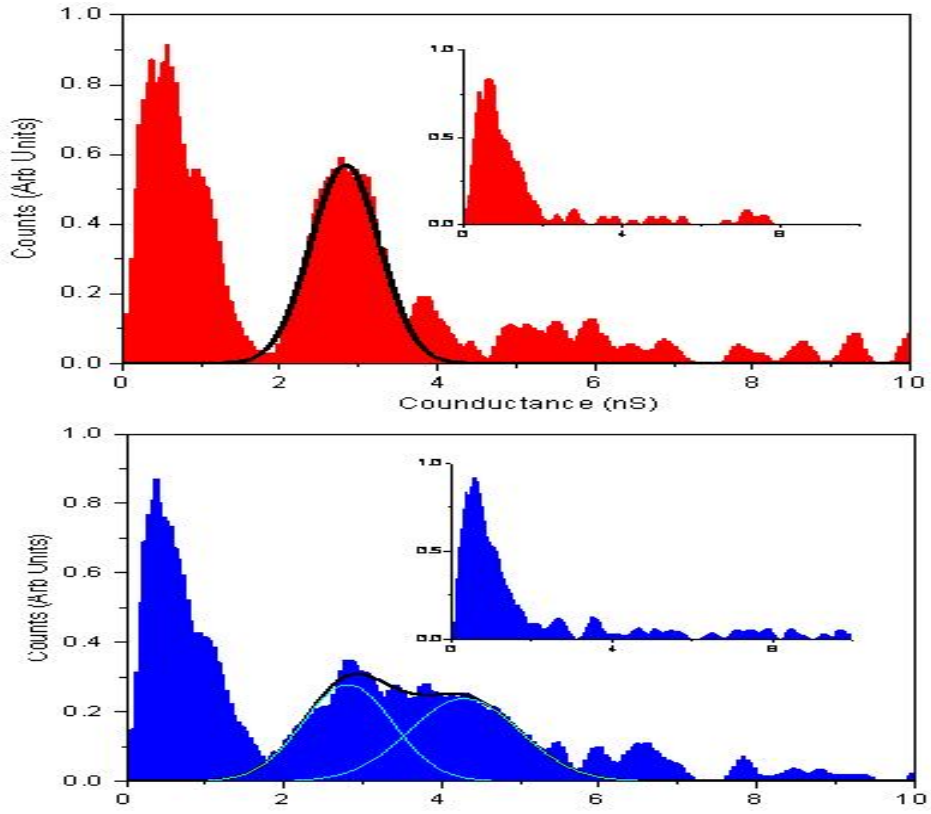

Figure 5.2. Conductance histograms of porphyrin fullerene dyads on ITO. The red histogram is with the light off, and the blue histogram is with the light on. The insets in both pictures are light on and off histograms of experiments conducted on blank ITO samples.

The conductance of the porphyrin-fullerene dyad, both in the dark and under laser illumination, was determined using the instrumentation described in the previous section. Since the dyad molecules contain a porphyrin, it is believed that the conductance of the molecule may be affected by photon absorption of that porphyrin. The molecules were exposed to 520 nm laser illumination for 10 minutes at a time, followed by 10 minutes of darkness as controlled by the

programmable optical shutter. This allowed for the reversibility of any changes in conductance to be determined. Figure 5.2 shows the results of the experiment performed at a laser intensity of 183 ± 13 mW/cm^2. The conductance histogram in red shows the conductance values of the molecule during the dark periods, while the blue histogram shows the conductance values of the molecule during the illuminated periods. The peak in both histograms between 0-1 nS is an artifact of the measurement and/or the data analysis and occurs in control experiments with clean samples (Figure 5.2 insets).

In examining the dark conductance histogram, the molecule exhibits a singular conductance peak, which is determined to be the single molecule conductance of the dyad in the dark. This peak is centered at 2.45 nS. The illuminated histogram, however, looks remarkably different. The peak around 2.45 nS still appears, but is much broader, and another peak around 4.3 nS is also apparent. This second peak goes away quickly in the absence of light, since the non-illuminated histogram does not exhibit this conductance feature. This is clear evidence that the conductance of a portion of the molecules changes in a reversible manner upon illuminating at 520 nm.

This illuminated experiment was completed at different laser intensities to determine if any relation existed between the flux of photons on the surface of the ITO and the monolayer, and the strength of the second peak seen in Figure 5.2. The two peaks shown in the illuminated histogram were non-linearly fit to two Gaussian peaks, and the positions, amplitudes and widths of those peaks was

determined. The first peak is labeled P1 and the second peak is labeled P2. The two peaks were compared with the following formula

$$Ratio = \frac{(Guassian \quad Amplitude * FWHM)P_2}{(Guassian \quad Amplitude * FWHM)P_1} \qquad 5.1$$

This ratio was plotted against the laser power density in mW/cm^2 and is shown in Figure 5.3. Clearly, as the power density increases, this ratio increases nearly linearly until a peak power density around 270 mW/cm^2 is reached, at which point the ratio levels off. So, as the power density increases, the area under the Gaussian curve of the second peak compared to the first peak also increases, signifying that more of the molecules are exhibiting higher levels of conductance.

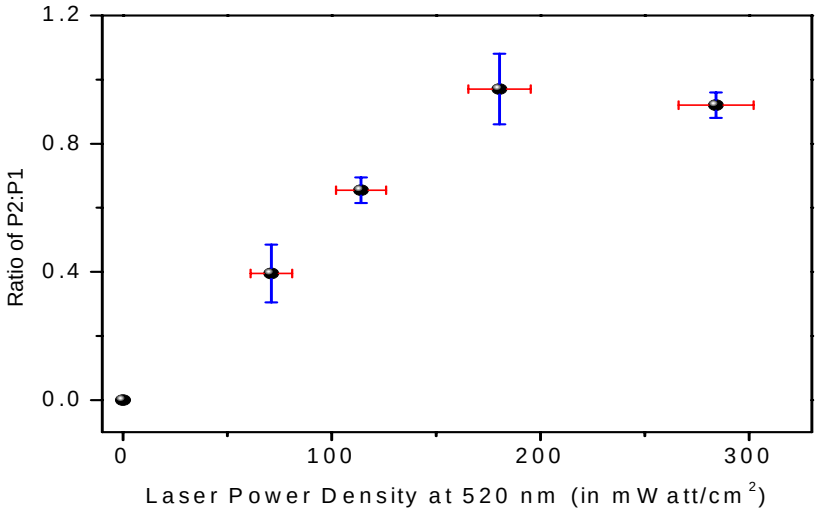

Figure 5.3. Graph of peak ration versus laser intensity. The higher conductance peak becomes stronger as the laser intensity increases.

Since the ratio levels off around 270 mW/cm^2, higher laser intensities were unnecessary in the apparatus. It is possible that higher intensities were accelerating molecular photodamage.

5.3.3. Free-base porphyrin

The conductance of a free base porphyrin with both carboxylic acid and pyridine functional groups was also measured under illumination. This molecule was chosen due to its lack of fullerene attachment in order to determine whether or not the fullerene plays a role in the change in conductance upon illumination. The conductance histograms of this molecule (not shown) do not indicate a higher conductance peak upon illumination, despite repeated experiments at numerous laser illumination powers.

5.3.4. Control experiment

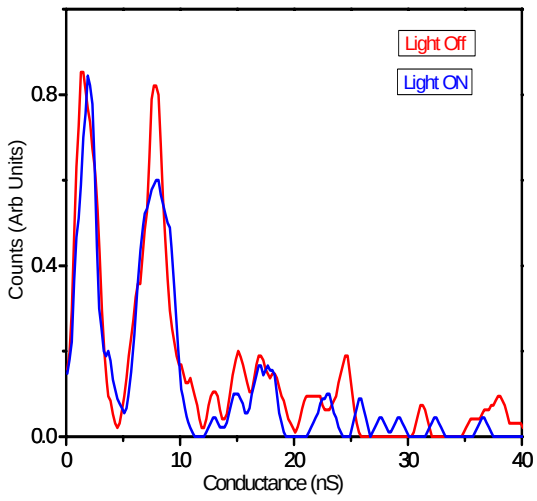

Figure 5.4. Light on and off histograms of 3-(pyridine-4-yl)-propionic acid

3-(pyridine-4-yl)-propionic acid was utilized as a control molecule. This molecule is a short alkane chain that has the same functional groups (carboxylic acid and pyridine) as the dyad molecule used in this experiment. However, this control molecule is not optically active. Figure 5.4 shows the

results of this experiment in the dark (red) and in the light (blue). The molecule shows little to no difference in conductance upon illumination, which is the expected result due to the lack of optical absorption at 520 nm.

5.3.5. Conclusions

The new conductance peak observed after illuminating the molecules with 520 nm is a remarkable feature. The first thought would be that the feature represents increase in conductance due to photogenerated charges. However, the power intensity utilized in this experiment is not sufficient enough to actually cause a noticeable shift in molecular conductance due to photogenerated charge. Even if every single photon that hit the molecule being probed was absorbed and the excited state charge was transferred into the electrodes generating a photoinduced current, that photocurrent would be much less than a picoampere, which is less than the detection limit of the experiment. Taking that into account, the substantial increase in conductance must be due to a factor other than photoinduced carrier generation.

The increase in conductance seen in the illuminated histograms has been ascribed to changes in the molecule during excitation that change how the molecule conducts electricity. The natural change to explore in this system is the electron transfer from porphyrin to fullerene. As explained, in solution, once the porphyrin absorbs light the excited state electron immediately transfers into the fullerene electron acceptor, extending the excited state lifetime of the molecular

unit. This charge separated state has a different electronic configuration than the ground state of the molecule, and may very well be the source of the change in molecular conductance. Evidence for this separated-state theory can be seen in the illuminated conductance of the free-base porphyrin without the fullerene. This molecule does not have a higher illuminated conductance, which aligns with the idea that the fullerene is, therefore, a necessary component in the molecular dyad conductance change.

This theory was tested with optical spectroscopy. Transient absorption was performed on ITO samples with dyad layers using a 520 nm laser line to pump the samples. The absorption kinetics between 550-880 nm (where absorbance can be attributed to porphyrin radical cations) show a very long lived state that went out to 14 us. Further, a transient absorption spectra showed the appearance of an absorption state around 640 nm. Figure 5.5 shows the transient absorption spectra of the dyads on ITO with the state at 640 nm appearing clearly after 3 ps (red squares), decaying after 10 ps (green circles) and almost, but not completely, gone after 2 ns (blue triangles). A similar spectra of free-base porphyrin on ITO shows no appearance of this peak.

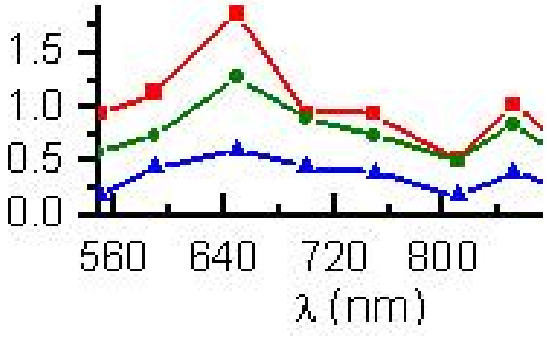

Figure 5.5. Transient absorption spectra of porphyrin-fullerene dyads on ITO. The red squares are after 3 ps, the green circles are after 10 ps, and the blue triangles are after 2 ns.

This peak is attributed to the formation of the porphyrin radical cation in the porphyrin-fullerene dyad on ITO. The long lived state (up to 14 us) shows that this cation is sometimes very long lived within the dyad film. Further, the fact that this state goes away very quickly after the light is turned off (almost completely gone after 2 ns) explains why the conductance goes back to the completely dark conductance after the light is turned off in the STM apparatus. This might also explain why the ratios of the two histogram peaks (Figure 5.3) changes with laser power intensity. There are probably more molecules in the cationic state when the laser intensity increases, increasing the number of high-conductance species.

The measurements on dyad molecules show how the scanning tunneling microscope may be utilized to understand how molecular conductance of novel molecules can be optically controlled. The ability to study this molecular arrangement at the single molecule level was necessary in order to observe this effect, due to fact that there are two very clear populations of molecules that have different conductances. A bulk measurement, by contrast, may have yielded an average measurement that does not fully explain the phenomenon. The STM was the ideal measurement technique for these molecules, and the instrumentation changes were necessary and vital in understanding illuminated porphyrin-fullerene molecular conductance. This measurement, in particular, shows the versatility of scanning probe instrumentation.

6. PORPHYRIN-FULLERENE DYAD THIN FILM GROWTH AND ELECTRICAL CHARACTERIZATION

It was recently found that the molecule in Figure 4.9 could organize to form multiple layers on an Indium Tin Oxide surface after the porphyrin ring had been protonated. The first evidence of this phenomenon came after sonicating the molecule in 1,2,4-Trichlorobenzene. The sonication of the solvent releases chlorine atoms, forming hydrochloric acid in the solvent. This acid, although very low in concentration, is enough to protonate the, typically low, concentration of the dyad in solution. A film of the protonated dyad molecules would then grow on an ITO substrate from this sonicated solution, thicker than a self assembled monolayer. It was determined that protonation of the dyad leads to these layers forming, as unprotonated dyads do not form such films. As a test of the illuminated scanning probe system, these protonated films were measured under both illuminated CAFM and illuminated mercury drop electrode apparatus for comparison purposes.

6.1. Film growth and characterization

As will be mentioned in the section describing CAFM measurements on these films, reliable data of photocurrent and photovoltage was only actually obtained for mercury drop experiments. For this reason, the materials and methods utilized in the mercury drop experiment are much more uniform since the best procedures for making films could only be determined after repeated photovoltaic results. In the materials and methods section, the set protocol for the

mercury drop experiments are noted, as are the different general methods for producing samples for the CAFM experiments.

6.1.1. Materials and methods

Sonicating solutions of dyad in 1,2,4-Trichlorobenzene is a somewhat haphazard way of protonating the molecules. For this reason, once it was determined that protonation caused dyad film growth, the organic acid Trifluoroacetic acid (TFA) was utilized as the protonating agent, in lieu of the sonication to produce HCl in solution. For a solution of 5 uM, a single drop of TFA is enough to protonate the entire solution, however multiple drops were typically utilized to ensure that the solution remained protonated throughout sample deposition, as TFA is more voltatile that 1,2,4-Trichlorobenzene and can evaporate out of solution easily.

In order to make sample solutions, 1,2,4-Trichlorobenzene was first stirred with sodium bicarbonate in order to remove residual HCl that might exist in the solvent as bottled. This allows for TFA to be the only protonating agent in the sample solutions. For CAFM experiments, the 1,2,4-Trichlorobenzene was distilled once under reduced pressure prior to use. For mercury drop experiments, it was found that distilling twice gave better photovoltaic results, probably due to the removal of residual sodium bicarbonate left in the solvent after the first distillation. The distillation apparatus was cleaned with distilled water and ethanol between distillations for the mercury drop experiments. 1,2,4-

Trichlorobenzene was stored after distillation in the dark to prevent any HCl forming in the solution and was purged with Nitrogen prior to use.

For all experiments, a stock solution of the dyad molecule was prepared by stirring several milligrams of the molecule into about 15 mL of 1,2,4-Trichlorobenzene until dissolved. For mercury drop experiments, a couple drops of TFA was also added to the solution prior to stirring, and the solution was heated. The TFA was found to help the dyad dissolve into the solvent better. For mercury drop experiments, the solution was allowed to cool before further testing.

The concentrations of stock solutions were checked by absorbance in a UV-Vis spectrophotometer (Varian, Palo Alto, CA). Spectra were taken from 200-800 nm. For the mercury drop experiments, stock solution concentration was determined in protonated form, whereas this varied in CAFM experiments. In the mercury drop experiments, the spectra was also utilized to determine if the solution was fully protonated by the TFA. Once concentration of the stock solution was determined, it was diluted down to the desired sample solution concentration, which was usually 5-10 uM for CAFM experiments and was always 10 uM for mercury drop experiments. A couple more drops of TFA was typically added during the dilution process to maintain proper dyad protonation throughout sample deposition.

Background UV-Vis spectra of the ITO slides on glass (Delta Technologies) was typically taken in the UV-Vis spectrophotometer prior to sample cleaning. Samples were cleaned by sonicating in acetone for 10 minutes

to remove large residual particles, and then cleaned for 5 minutes in oxygen plasma to remove any leftover organics from the surface of the ITO. ITO slides were then immediately removed from the oxygen plasma and submerged in the sample solutions. The solutions were then purged by bubbling with nitrogen through a cleaned needle, and sealed under nitrogen with parafilm. Samples were left in the solution in the dark for a determined length of time. For CAFM experiments, samples were left anywhere from 1 day to 2 weeks, while, for mercury drop experiments, samples were left to soak in solution for 6 days.

ITO slides removed from sample solutions were typically green immediately after removal After removal from solution, CAFM samples were rinsed with both 1,2,4-Trichlorobenzene and toluene and dried in nitrogen. TFA was sometimes added to these solvents to maintain the protonated state of the films. Mercury drop samples were dried in a vacuum oven for at least an hour at 50 C. Both rinsing with solvent (without TFA added) and drying in the vacuum oven caused the color of the films to change from bright green to yellow, indicating a deprotonation of the porphyrin following removal from the sample solution, which was probably a result of some TFA evaporation.

6.1.2. Spectral properties of dyad thin films

All spectral measurements were taken with a UV-VIS spectrophotometer (Varian, Palo Alto, CA). Background absorbance of molecular solutions were taken with clean solvent in a 1 cm pathlength quartz cuvette, and background absorbances of ITO were taken by placing clean ITO slides in the cuvette holder

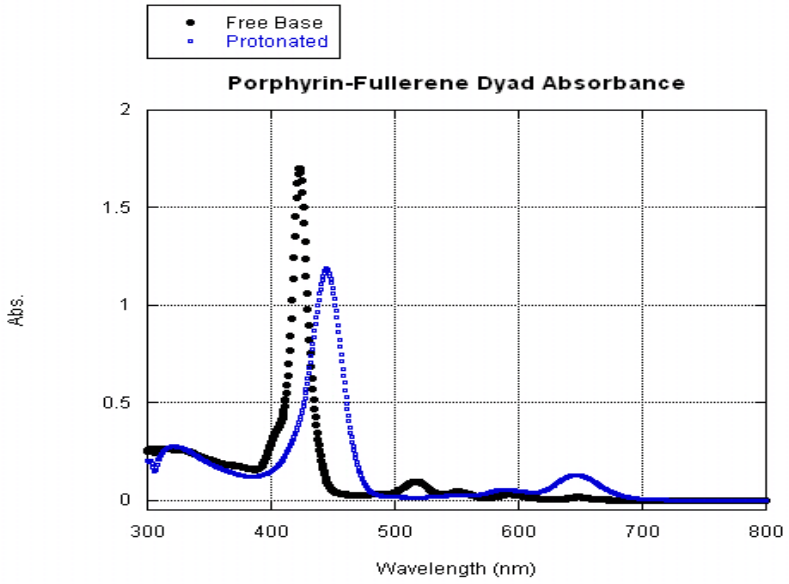

Figure 6.1. Absorbance spectra of 5 uM free-base and protonated porphyrin-fullerene dyad in 1,2,4-Trichlorobenzene.

in the instrument. Figure 6.1 shows the absorbance spectra of the dyad in solution. The black circles represent the spectra of a solution of 5uM free-base (not-protonated) dyad in 1,2,4-trichlorobenzene. The blue squares represent the spectra of the same solution after protonation with TFA. After protonation in solution, the soret peak shifts from 415 nm to 445 nm. The full width at half maximum of the Soret also changes from about 15 nm to 30 nm, indicating absorption broadening of the Soret after protonation. The absorbance at 650 nm (Q-band) also increases after protonation. The color of the solution visibly turns from yellow to green after protonation with TFA.

Figure 6.2 shows the absorbance spectra of a monolayer of dyad on ITO created from a 5 uM solution of the dyad in TCB, and a spectra of a dyad film grown from a 5uM solution of protonated dyad in TCB. The deposition time for

both samples was 5 days. The Soret peak for the sample made with unprotonated dyad was at 430 nm, while the peak position for the sample made from protonated dyads was at 435 nm. The Soret absorbance for the sample made from un-protonated dyads was 0.062, while the soret-absorbance of the sample made with protonated dyads was 0.32 and the ratio of the FWHM of the two soret peaks was roughly 2:3 (actual values were 28 nm for the sample made from unprotonated dyad and 41 nm for the sample made from protonated dyad), indicating that the sample made from the protonated dyad also showed peak broadening. The red-shifted peak of the sample made from protonated dyads, along with the peak broadening and the fact that the peak at 650 nm is also relatively larger than the other Q-band peaks indicates that, after removal from the solution, not all of the film de-protonated back to the free-base form of the porphyrin. However, since the overall shape of the spectra of the sample made with protonated dyad has the features that are associated with the free base sample, it is believed that the majority of the porphyrin in the film reverted to free-base form.

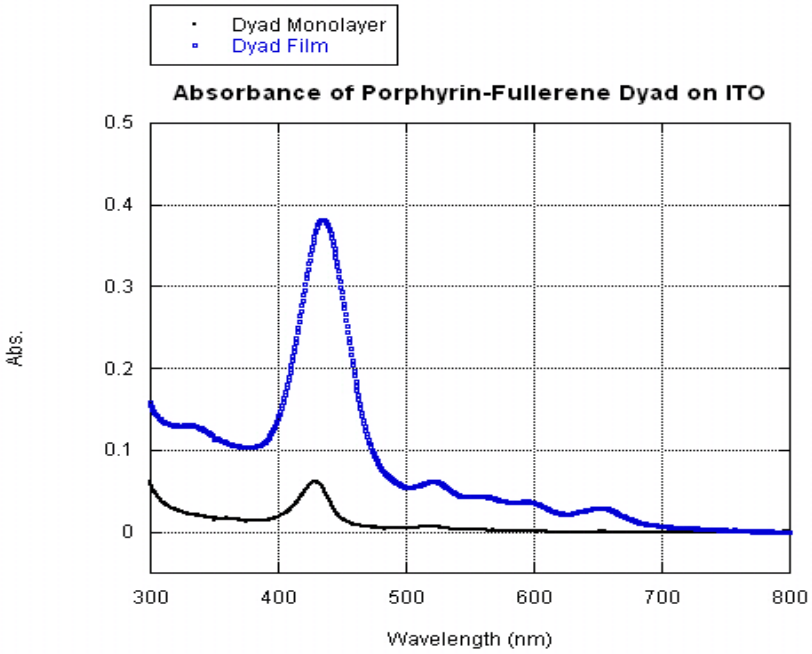

Figure 6.2. Absorbance spectra of porphyrin-fullerene dyad on ITO

6.2. Attempts at CAFM photocurrent measurements

6.2.1. Materials and methods

Numerous attempts were made to study photocurrent properties of dyad thin films on ITO with illuminated CAFM. The following outlines a typically CAFM experiment on dyad thin films. The same illuminated scanning probe instrumentation that was outlined in chapter 5 was employed to study these films with the AFM instead of the STM. The only major differencse with the AFM system was the use an AFM scanner in the microscope and the use of an AFM photodetector with an optical bandpass filter positioned over the photodiode. This bandpass filter allowed for the AFM laser light to reach the photodiode, but blocked out the green illuminating light from the Ar/Kr laser. Samples were

prepared as outlined in the previous section and were tested in multiple solvents, including 1,2,4-Trichlorobenzene, toluene and toluene with TFA added. AFM tips were coated with chromium and gold in consecutive layers. This procedure was outlined in chapter 3, however, for many of the CAFM experiments more layers were utilized. Conductive diamond tips (Mikromash) were also used in some CAFM experiments. Illumination was conducted at 520 nm at different powers.

The current, shutter voltage and deflection were directly wired through BNC cables to the National Instruments data acquisition system (USB-6221), while the piezo voltage was routed through a homemade voltage divider and follower before connection to the data acquisition system. These four values were monitored and recorded with custom-written labview software. The AFM tip was approached to the surface through the PicoScan control software to a user-specified tip deflection (typically 1 V on the AFM photodiode). Once the tip had settled on the surface, the labview program was started and the shutter was programmed to open and close at set times. The labview program recorded the photocurrent as the shutter opened and closed, along with the deflection (system was usually kept under deflection control), shutter voltage and piezo voltage.

6.2.2. CAFM photocurrent results and challenges

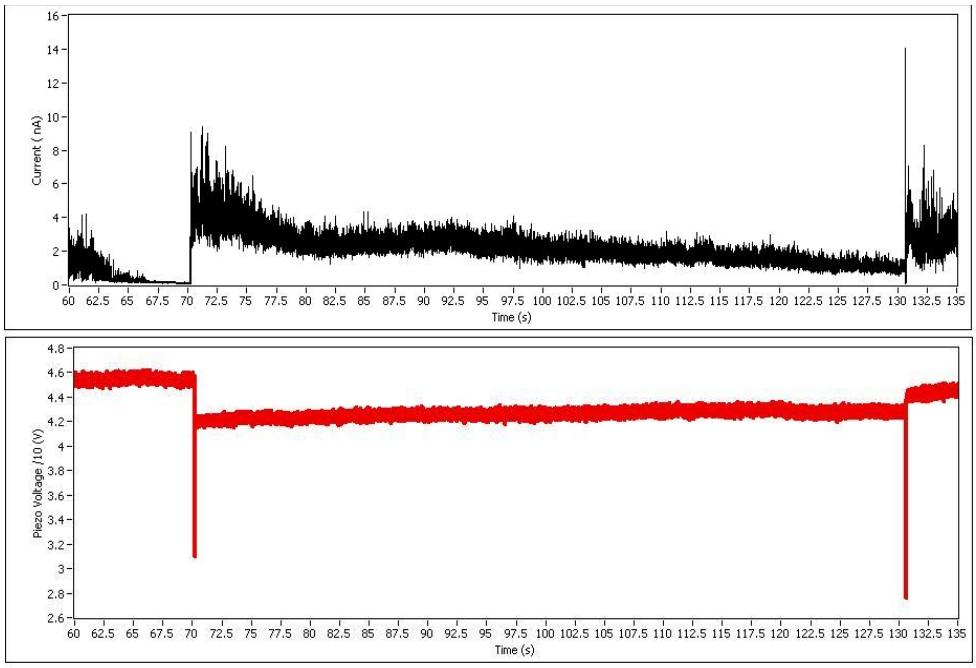

Figure 6.3. CAFM photocurrent measurements. The top graph shows the current as the light is switched on around 70 seconds and off at 130 seconds. The current increases to about 6 nA when the light is turned on. The lower graph shows the voltage applied to the piezo (divided by 10 through a voltage divider). Clearly, when the light is turned on, this voltage changes, reflecting a disturbance in the AFM tip. The voltage bias was 0.005 V.

Figure 6.3 shows a typical result from a CAFM photocurrent experiment. Although, it appears as though the current is increasing rapidly when the sample is illuminated (70 seconds), changes in other signals indicate that the increase in current may be related to more than light absorption by the dyad film. The voltage on the piezo (also shown in Figure 6.3) also changes when the sample is illuminated. Since the servo is on in this experiments, the piezo voltage changes with changes in the deflection of the AFM tip. Typically, when an AFM tip is on the surface, these changes are quite small and the piezo voltage goes up and down

to keep the cantilever at a stable deflection. However, as can be seen in Figure 6.3, the change in piezo voltage is not random and occurs precisely as the shutter opens and closes. This seems to indicate that there is a change in cantilever deflection upon opening and closing the shutter. If this is true, then the light may be inducing a change in the force between tip and surface, leading to changes in current which may be unrelated to photon absorption by the film.

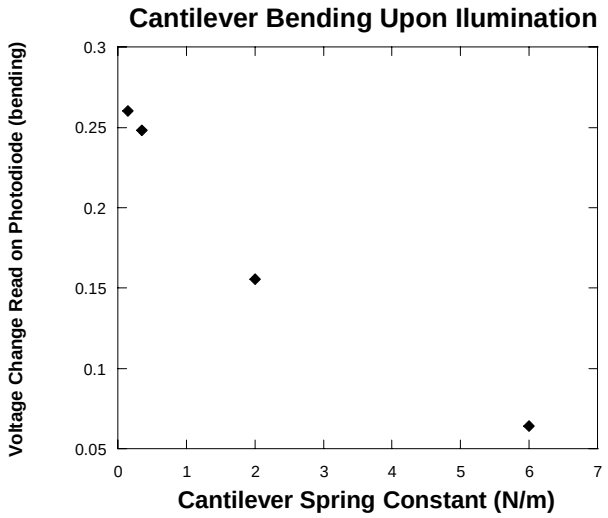

Figure 6.4. Effect of laser illumination on cantilever bending. As the value of the cantilever spring constant gets larger, the voltage change read on the detector gets smaller, indicating less bending of the cantilever upon illumination.

This was explored further by examining the effect that laser illumination has upon tip deflection by removing the tip from sample surface. The deflection of the cantilever was monitored away from a surface both before and after illuminating it with the Ar/Kr laser. Figure 6.4 shows the results of the change in tip deflection versus cantilever spring constant upon laser illumination. Clearly, as the spring constant decreases, the amount that the AFM laser deflects gets larger. This suggests that the laser can actually induce a bending on the cantilever, the

displacement of which is inversely proportional to the spring constant. This, of course, suggests flaws in the experimental design if the probe is bending due to interactions with the illuminating laser. Changes in contact forces can, by themselves, lead to changes in the current recorded by the CAFM.

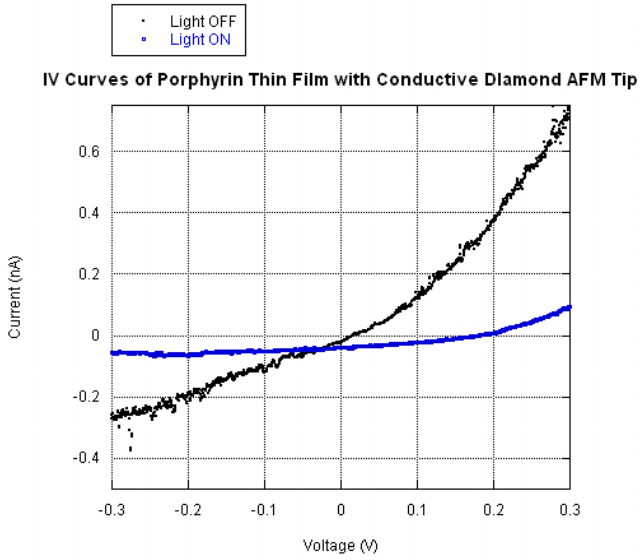

Figure 6.5. IV curves of porphyrin layer made with conductive diamond AFM tips. The blue curve, while not showing as much overall current, shows significant photovoltage as evidenced by where the curve crosses the 0 current axis.

Other methods were employed to reduce the effect of this interaction between the probe and the light. In one method, the tip was first approached to the surface either in the light or in the dark. IV curves were then measured in the light and in the dark, and the system was maintained in a static illuminating condition throughout the measurement. Influences of the light on the cantilever were then reduced. Initial measurements on porphyrin thin films (made in a similar method to the dyad thin films) utilizing a conducting diamond tip were promising, as the IV curves (Figure 6.5) showed significant open-circuit voltage as well as fill factor, defined as the maximum power output divided by the theoretical maximum determined by the short circuit

current and the open-circuit voltage. The conductive diamond was thought to enhance the photovoltaic properties of the system due to having a favorable work function that created a larger energy gap than the typical gold tips, However, when these measurements were repeated on a blank ITO slide, similar photovoltaic results were obtained. It is thought that the boron doping in the conductive diamond tip makes for a p-type semiconductor. When in contact with ITO, then, the tip can form a P-N junction with the n-type ITO, and work as a photovoltaic device without the need for another absorbing material. IV curves on dyad layers with a gold tip showed no measurable photocurrent or photovoltage.

6.2.3. Calculations of expected photocurrents

Since the AFM seemed inadequate in determining photocurrent from dyad films, it was necessary to calculate what the theoretical maximum photocurrent would be given the dimensions of the tip and the absorptive properties of the film. This helped determine whether the AFM system was not working properly, or whether the system was simply incapable of observing even the maximum possible generated photocurrent given the AFM specifications. This was accomplished by first examining the absorption spectra of a typical dyad film on ITO (Figure 6.2**)**.

The extinction coefficient of the porphyrin-fullerene dyads in solution at the Soret peak is about 380,000 $M^{-1}cm^{-1}$. The width of the peak on the sample, however, was approximately 1.75 times the width of the peak in solution. So,

using a guassian fit for the Soret peak, the extinction coefficient of the molecule on the ITO sample can be estimated at approximately 220,000 $M^{-1}cm^{-1}$. The peak absorption of the film in the absorption spectra (Figure 6.2) is approximately 0.375. The concentration of the molecules on the sample can then be given by Beard's law as

$$Absorption = \varepsilon cl \qquad 6.1$$

Where ε is the extinction coefficient, c is the concentration and l is the pathlength. If, instead of being on a slide, the molecules were in a 1 cm pathlength cuvette, the concentration would be approximately 1.7 uM or 1.02 x 10^{15} molecules/mL in the cuvette. If, now, those molecules were condensed onto two 1 cm x 1 cm surfaces (the front and back of the ITO slide), that would mean that each side of the ITO contained 5.12 x 10^{14} molecules. The molecular area had been previously determined by molecular modeling of tetraphenyl-porphyrin as 213 $Å^2$. Dividing the area of the slide probed by the spectrophotometer by this area gives about 5 x 10^{13} molecules per layer on the surface. Dividing the number of molecules by this gives approximately 10 layers of molecules on the surface of the slide.

A power intensity that has been shown not to damage the molecules in the breakjunction experiment is approximately 0.183 W/cm^2. Converting this to photon flux per Angstrom squared (the absorption cross sectional area of the molecules) gives

$$\frac{183mW}{cm^2} * \frac{3x10^{15}\ photons}{mW * s} * \frac{(100cm)^2}{(10^{10}\ \mathring{A})^2} = 55\frac{Photons}{\mathring{A}^2 * s} \qquad 6.2$$

The area of the AFM tip contact is calculated by Hertz theory

$$a^3 = \frac{R * F}{K} = \frac{(200x10^{-9}\ m) * (1 * 10^{-9}\ N)}{10 * 10^9\ Pa} = 2x10^{-26}\ m^3 \qquad 6.3$$

Where a is the radius of the circular contact area, R is the radius of the probe, F is the force of contact and K is the Young's modulus of the material (estimated here as 10 GPa).[79] Thus, the area of the contact is approximately 23 nm^2. The area of the molecule, as mentioned above, is approximately 2.13 nm^2, and so the number of molecules being probed by the AFM tip is then

$$N = \frac{23nm^2}{2.13nm^2} * 10\ \text{layers} \approx 108 \qquad 6.4$$

Since every molecule has an absorption cross sectional area of approximately 1 $Å^2$, then the photon flux per $Å^2$ can be used to determine the number of electrons generated by the film in contact with the AFM probe, per second.

$$(108\ \text{molecules}) * (\frac{55\ \text{Photons}}{\mathring{A}^2 * s}) = 5940\frac{electrons}{s} = 9.52x10^{-4}\ pA \qquad 6.5$$

This calculated photocurrent is well below the detection limit of the CAFM preamplifier. Even significant changes to the quantities in this calculation (lower elastic modulus or larger tip radius) do not change the final result enough for the sensitivity of the current instrumentation. Therefore, it was decided that the CAFM is an ineffective instrument for studying photocurrent behavior in these samples. This is, of course, compounded by the various artifacts found when

doing the actual measurements, such as laser interference and tip doping complications.

6.3. Mercury drop photocurrent measurements

Clearly, based upon the calculations, the AFM tip is simply too small to measure any photovoltaic effects with the current instrumentation. In order to test this assumption, and to see if these dyad films truly had any photovoltaic properties, a mercury electrode was also utilized to study these films under illumination. The size of the mercury drop is much larger than the size of the AFM tip, and can be controlled to a greater degree by using different drop volumes and contact areas. The size of the electrode contact area can also be easily determined by optical techniques, as opposed to the AFM tip which requires electron microscopy in order to determine tip radius.

6.3.1. Materials and methods

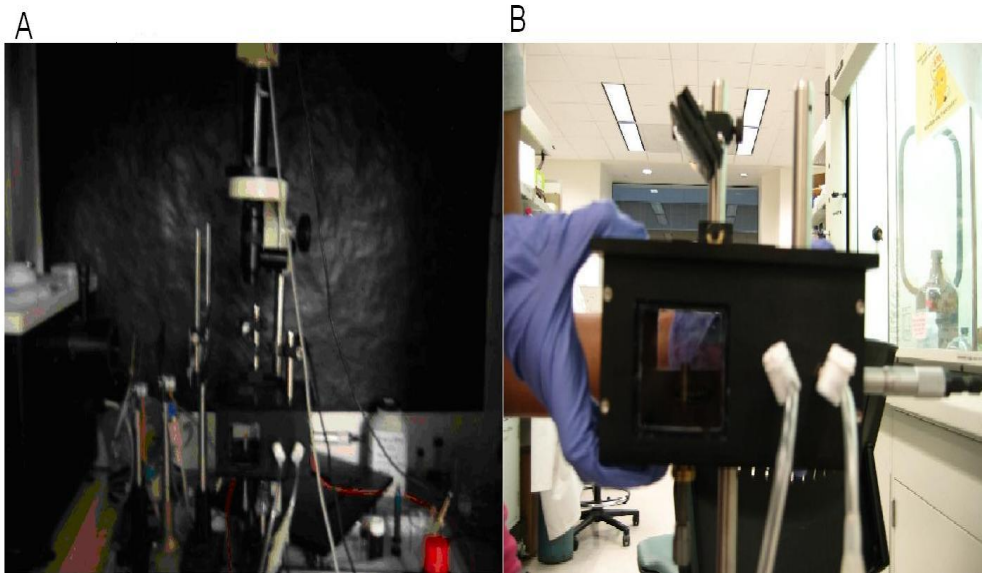

Figure 6.6. Mercury drop electrode instrumentation. A) A photograph of the entire setup with CCD camera positioned over the beam splitter and monochromator to the left. B) A close up of the environmental chamber with beam splitter above.

Samples were prepared for mercury drop experiments as described in the previous sections. The average peak absorbance for the samples measured was 0.34 ± 0.10. Figure 6.6 shows a picture of the mercury drop experimental apparatus. All experiments were conducted in an aluminum environmental chamber to prevent electrical noise in the measurements. The sample was attached ITO-side down to the sample holder and made electrical contact with a piece of brass. This piece of brass was then in electrical contact with a Kiethley electrometer outside of the aluminum environmental chamber. Light from a Xe/HgXe lamp (Oriel) and monochromator (SPEX) was diverted to the sample by reflection off of a 50/50 beam splitter situated on top of the environmental

chamber and through a window placed in the chamber lid. Part of the beam was transmitted through the beam splitter to a laser power meter also situated on top of the environmental chamber.

At the bottom of the environmental chamber, a stainless steel precision adjustment screw was attached which translated up and down within the environmental chamber. The drop of mercury could be situated on top of this adjustment screw and then be twisted up to be in contact with the Indium Tin Oxide. The precision screw was grounded, effectively grounding the mercury drop. The sample holder within the environmental chamber was tension fit onto the non-rotating spindle of a micrometer whose adjustment knob screwed into the side of the chamber. This allowed for the sample to be moved in one dimension so that multiple locations on the same sample could be probed by the mercury drop.

Before testing, the intensity of the illumination was determined. A calibrated photodiode was placed at approximately the same position as the sample. The sample holder and the beam splitter were positioned until the desired intensity was achieved. Once this had been completed, a spectra of the lamp was recorded by moving the monochromator from 300 nm to 800 nm and observing both light and dark currents at wavelengths in 5 nm increments. This allowed for future action spectra to be calibrated in order to determine the incident photon-to-electron conversion efficiency (IPCE).

A CCD camera with telescope zoom was situated above the beam splitter looking down through the window into the environmental chamber. The camera was able to focus on the contact area of the mercury drop on the ITO. For every spot tested on the film, a picture of the drop on the ITO was recorded. The contact area diameter was calculated by determining the diameter of the precision screw which was also in the camera frame. By determining the diameter of this screw with a precision micrometer, the diameter of the contact could be directly read from the camera image.

The 20 uL mercury drop was placed in electrical contact with the precision screw by dropping it on the top of the recessed tip of the screw. The drop could then either be used for experiments as a clean electrode, or a monolayer of thiolated organic molecules could be self assembled on the mercury drop. Various experiments done previously by other groups have shown improved photovoltaic performance with the addition of an interfacial layer between electrodes and the photoactive material.[80,81] One reason that an interfacial organic layer may improve performance is the idea that an organic with an intrinsic dipole moment may direct current in a diode like way, forcing electrons or holes to flow in a singular direction and preventing recombination with the photoactive material after carriers have percolated to the electrodes. This could be especially important with the mercury apparatus, as the work function of mercury is very similar to that of ITO (4.49 eV for mercury and 4.3-4.75 eV for ITO).[82-84] This means that the electrodes by themselves do not provide a strong current direction

preference. In these experiments, a hexanethiol monolayer was utilized in order to determine if it could improve upon the photovoltaic properties of the dyad films. Previous mercury drop experiments have shown that alkanethiols can exhibit rectifying behavior when sandwiched between a semiconductor substrate and a mercury electrode.[85] It is then believed that the hexanethiol may prevent electron-hole recombination in the dyad film.

Hexanethiol monolayers were assembled on the mercury drop by applying a drop of neat hexanthiol solution directly to the mercury drop sitting on top of the precision screw. Afterwards, the experimental chamber was sealed and flushed with nitrogen for five minutes. A kim wipe was utilized to remove any excess hexanethiol on the mercury drop, and the chamber was resealed under nitrogen for another 5 minutes. Hexanethiol is very volatile so after 5 minutes in a nitrogen atmosphere any unattached molecules evaporate off of the mercury drop leaving the self assembled monolayer ready for testing.

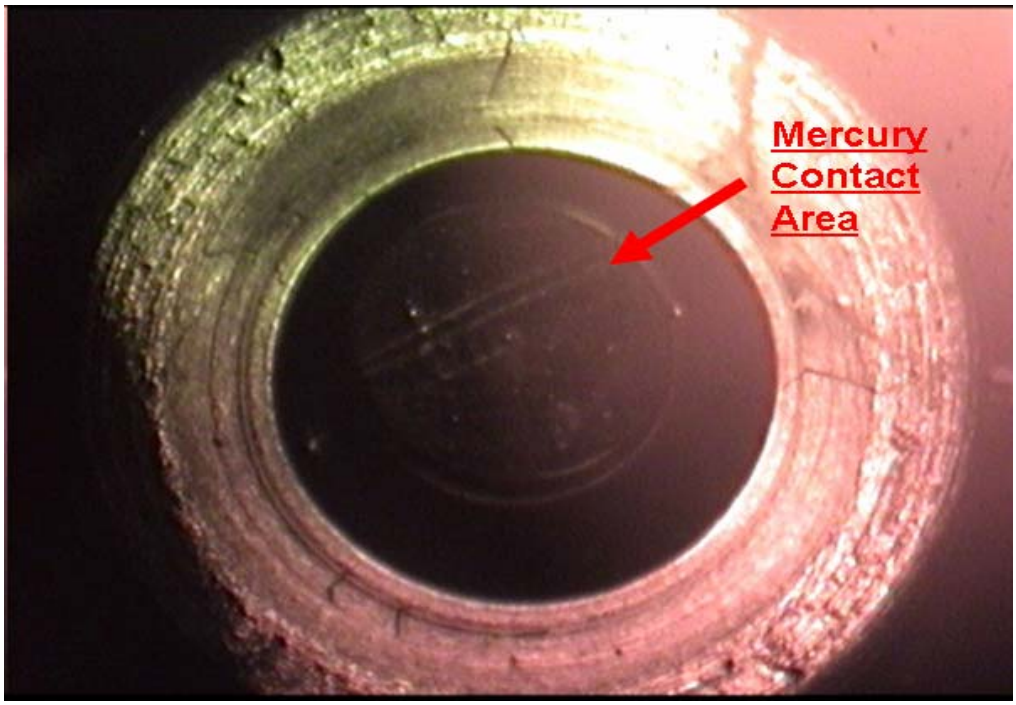

Figure 6.7. CCD image of mercury in contact with dyad thin film sample. The inner circle is the mercury contact, while the outermost circle is the edge of the precision screw.

After contact with the ITO sample, a picture of the mercury drop was taken with the CCD camera positioned over the optical beam splitter. A photo of a typical mercury drop contact area is shown in Figure 6.7. The center circle is the mercury in contact with the ITO, while the largest circle is the edge of the precision screw that supported the mercury drop. This outer circumference was utilized to calibrate the area of the mercury drop contact.

Electrical tests were performed to determine the photovoltaic properties of the dyad thin film. The first test was a photocurrent experiment completed under white light illumination. The current between the ITO and the mercury drop was recorded on the Keithley electrometer at 0 bias. After a given time the sample was illuminated from reflection off of the beam splitter for a time, before the light

was blocked from the sample again. Similarly, a photovoltage measurement was recorded with the same technique, but with the electrometer recording the voltage between the two electrodes instead of current. An IV curve was also recorded in the dark and in white light illumination. Finally, an action spectrum of the photocurrent was completed by ramping the monochromator from 300 nm to 700 nm, with 5 nm increments. For each wavelength, the dark current was recorded along with the illuminated current. The subtraction of the two would then give the photocurrent generated at each wavelength by the dyad sample.

6.3.2. Mercury drop electrical results

Initially, 6 samples were prepared as described above in the materials and methods section for dyad thin film growth. Three samples were tested with a mercury drop that had been treated with neat hexanethiol solution as described above, while 3 samples were tested with a bare mercury drop. All experiments were performed in a nitrogen atmosphere. 5 spots on each sample were tested, and the positions of each spot were recorded on the micrometer. The same horizontal positions were tested on all six samples.

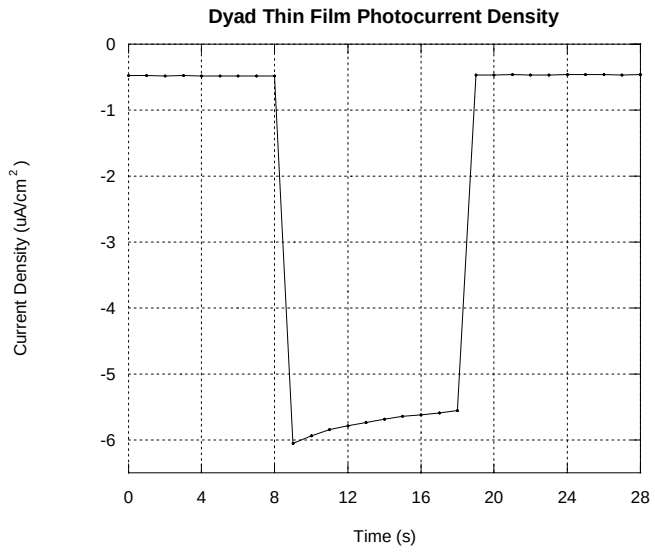

Figure 6.8. Dyad thin film photocurrent density measurement.

Figure 6.8 shows a typical photocurrent measurement taken with a mercury drop with a hexanethiol monolayer. The current is negative which indicates that the electrons are going into the mercury drop. Almost all spots with the hexanethiol monolayer show some transient photocurrent with white light illumination, whereas, with the bare mercury drop, only 6/15 spots show any measurable photocurrent. This may be due to the fact that the current in the dark at 0 V is often over 1 uA for the bare mercury drop, making it difficult to detect small changes in current on the order of nanoamperes. The lack of measurable photocurrent may also be due to the lack of current direction preference explained earlier. The average photocurrent density measured with the hexanethiol drops was -1.56 ± 1.42 uA/cm^2, while the average photocurrent density measured with the bare mercury drops was -1.32 ± 0.96 uA/cm^2 (only included were drops that showed measurable photocurrent).

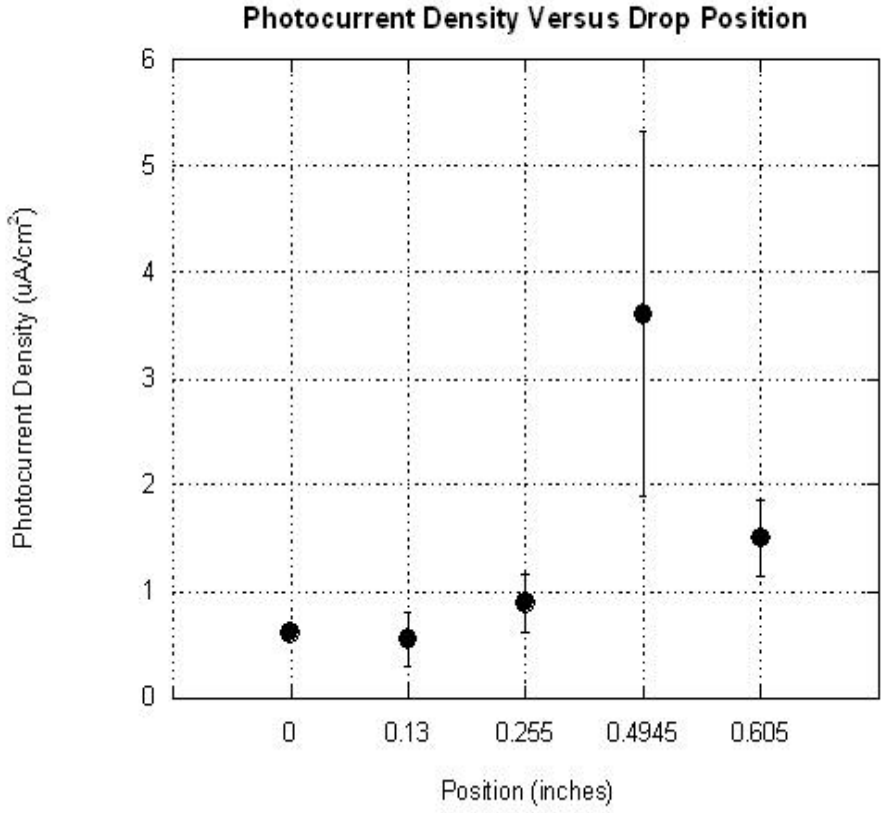

Figure 6.9 Average photocurrent density versus drop position, measured from position 1. The mercury drop had a hexanethiol monolayer. Spot 1 only had measurable photocurrent on 1 sample, so there are no error bars a the zero position.

Figure 6.9 shows the average value of the photocurrent density at each of the 5 spots with the hexanethiol drop. Values were only taken if the photocurrent density was measureable and are noted as such. The samples were only 1″ long, and it is noted that the values of the photocurrent density uniformly increase towards the middle of the sample, and then decrease when approaching the other

end of the sample. This could be due to non-uniform film thicknesses depending upon position, or non-uniform ITO electrical properties.

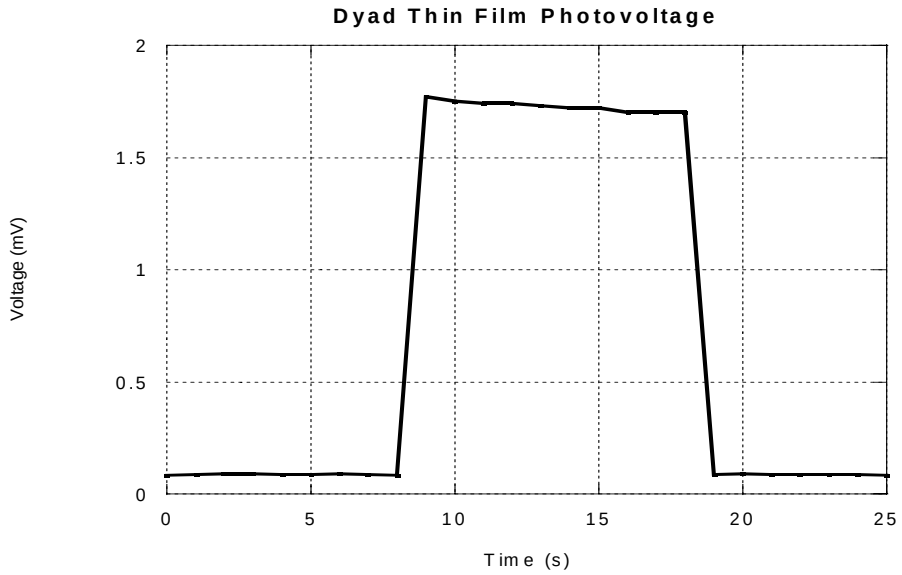

Figure 6.10. Dyad thin film photovoltage measurement.

Figure 6.10 shows a typical photovoltage measurement taken with a hexanthiol drop. The photovoltages measured for all drops were relatively low, with the largest photovoltage response measuring about 1.75 mV. The average measured photovoltage for all hexanethiol drops and positions was 0.20 ± 0.45 mV. The hexanthiol drops, again, showed larger values of photovoltage than the bare mercury drops (average photovoltage for bare mercury drops was 0.12 ± 0.18 mV) which could be due to the reduction in charge recombination with the hexanthiol layer. The large standard deviations seen in both the hexanethiol and the bare mercury drops are due to variations in measured quantities based upon

position of the drop on the sample. This variation in position is similar to the photocurrent density measurements.

Due to the presence of artifacts in the CAFM photocurrent data, it was important to obtain evidence that no similar artifact occurred in the mercury drop experiments which would lead to a false photocurrent observation. Specifically, it was important to validate that the photocurrent was due to the presence of the dyad film on the ITO and not some heating effect or effect between the mercury drop and the ITO (as was the case with the conducting diamond AFM tip). If the photocurrent occurred in wavelengths that the dyad absorbs strongly, then this would be strong evidence that the photocurrent occurs due to the dyad film. As such, the photocurrent action spectra gave reliable evidence that the photocurrent was the result of light absorbance from the dyad thin films. Figure 6.11 shows a photocurrent action spectra on the same graph as a spectra of the fraction of photons absorbed for the same sample (measured with a UV-Vis spectrophotometer). The photocurrent in the action spectra is the magnitude of the measured current so that both the absorbance and the current appear on the same side of the graph. Clearly, the maximum of the photocurrent is observed to appear very close to the Soret of the dyad thin film. Furthermore, there are peaks in the photocurrent where porphyrin Q-band absorption peaks occur (500-700 nm). This gives clear evidence that the photocurrent results are due to the dyad thin film, and not some experimental artifact.

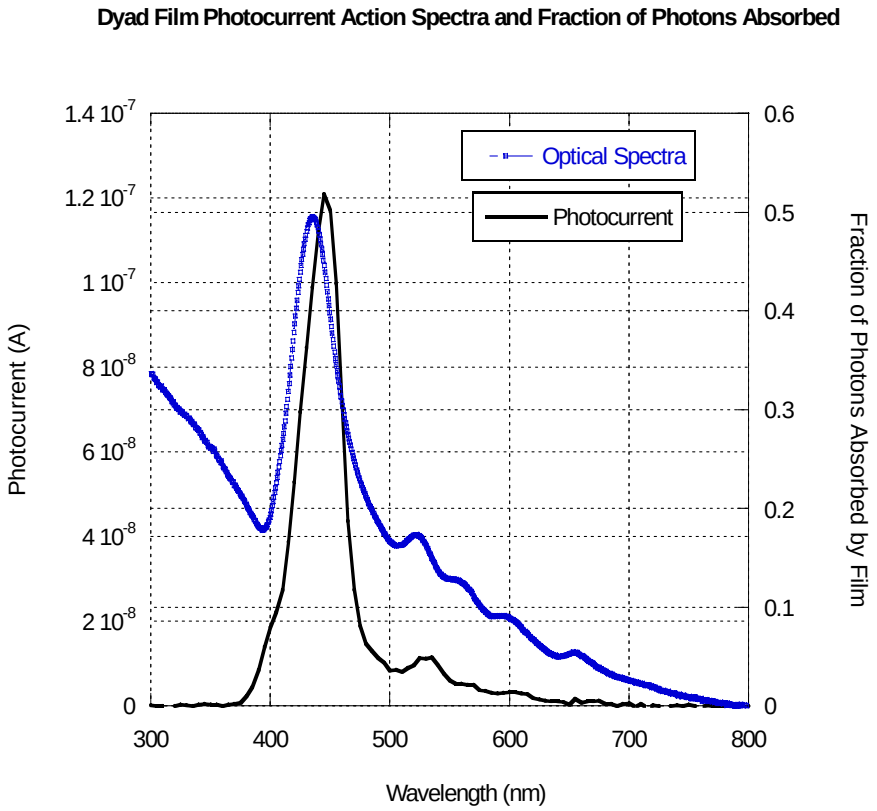

Figure 6.11. Comparison of photocurrent action spectra of the dyad film with the spectra of the fraction of photons absorbed by the sample. The shape of the photocurrent action spectra (black) is very similar to the shape of the photon absorbance spectra. Photocurrent is typically negative, but is displayed positively here.

Data from almost all hexanethiol drop action spectra (10 out of 14) showed measurable photocurrent, while only 5 out of 14 of the clean mercury drops showed measurable photocurrent in the action spectra. In both the hexanethiol drops and the bare mercury drops, there was a spot where action spectra was not measured at all due to problems with the apparatus. The increase incidence of measurable photocurrent with the hexanethiol drop coincides with

previous results showing increased white light photocurrent with the hexanethiol drop compared to the bare mercury drop. Furthermore, the sign of the photocurrent in the action spectra with the bare mercury drop was occasionally positive, meaning that electrons went to the ITO as opposed to the mercury drop. This was never seen with the hexanethiol drop. Figure 6.12 shows an action spectra of a typical hexanethiol drop compared to the action spectra of a plain mercury drop with current going in the positive direction. This may help explain why the hexanethiol drop shows more overall efficiency. The mercury drop-dyad-ITO geometry may not provide enough driving force for the electrons and holes to move in a given direction with 100% certainty, meaning that slight variations in the film may lead to a switching of the current signal due to the lack of diode-like behavior from the metals. However, when a hexanethiol molecule is added, this could provide the correct dipole moment to control the direction of the current, and thus prevent recombination, increasing photovoltaic efficiencies.

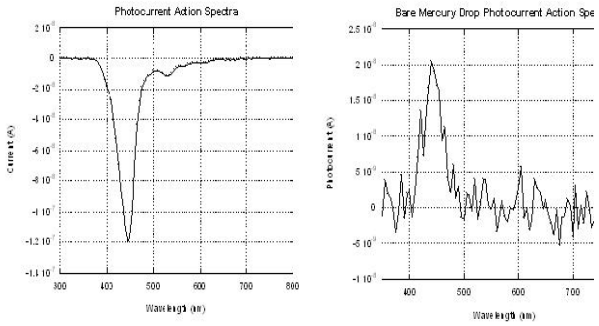

Figure 6.12. Comparison of photocurrent action spectra. On the left, a typical hexanethiol mercury drop action spectra on dyad thin film shows with negative current. On the right is the action spectra for a bare mercury drop with current going in the positive direction.

The IV curves were analyzed by examining the conductance of each curve from 0 V to 0.05 V.

Results showed a slight increase in conductivity upon illumination, with an average increase of approximately 5 ± 3.7 % for hexanethiol drops and 2.1 ± 3.8 % for bare mercury drops. Increases in conductance upon illumination are consistent with the STM results on single porphyrin-fullerene dyad on ITO, which showed that a long lived charge separated state can occur after illumination of the sample which most likely leads to increases in photo-conductance.

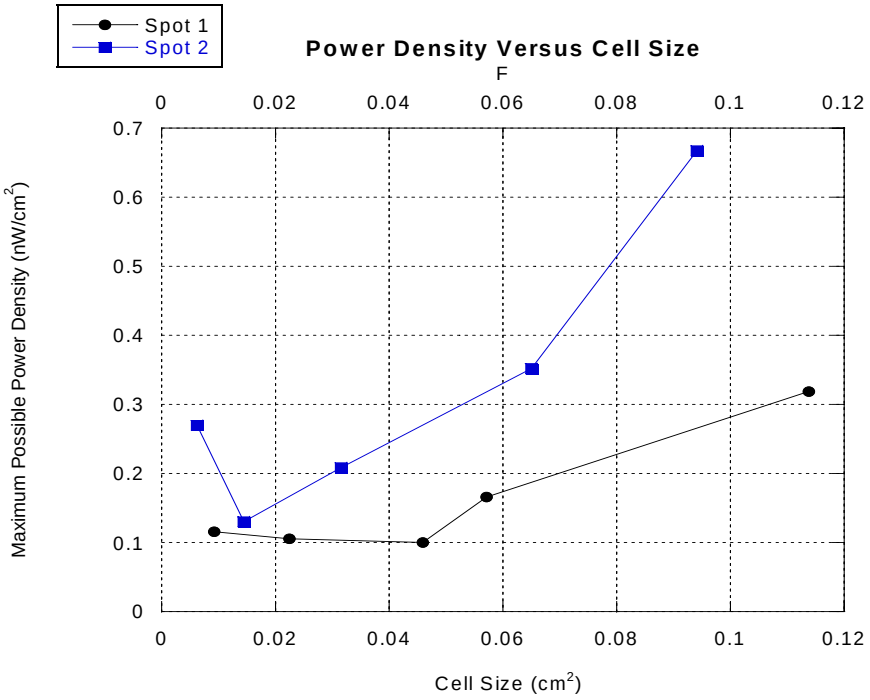

Figure 6.13. Maximum possible power density versus solar cell size. The maximum possible power density is calculated as the product of the transient photovoltage and the transient photocurrent.

Finally, the potential maximum power density of the cells were compared with the area of the cell (contact area of the mercury). Figure 6.13 shows a graph of the potential power per cm^2 (calculated as the product of the transient photocurrent and the transient photovoltage) taken for two positions on the same

dyad thin film sample. This particular sample was not one of the six samples originally made for the experiment, but was made later. For each position, the area of the cell was gradually increased, taking a transient photocurrent and photovoltage measurement before increasing the size of the mercury contact. In general, as the cell size gets larger, the potential power density increases. This is a unique application of the mercury drop electrode, as most solar cell area tests have to be conducted by making several permanent metal contacts on an organic film. Changes in photovoltaic efficiency, could then be due to changes in the sample from one location to another. With the mercury drop, these tests were able to be performed in the same general location on the organic sample. The increase in maximum possible power density with increased cell size may be due to better contact with the organic film as the mercury drop is pressed against the sample.

6.3.3. Calculations of photocurrent efficiencies

Although the action spectra and transient photocurrent measurements show that photocurrent is produced from the dyad thin films upon illumination, it is difficult to tell from these measurements how efficient the cell is at converting light to current. In order to determine this efficiency, the incident photon-to-electron conversion efficiency (IPCE) was calculated. This quantifies the percentage of photons that are converted into electrons during the illumination of a solar cell. The calculation of the IPCE is based upon the wavelength of the light

and the incident illumination intensity which was recorded on the photodiode. The calculation to determine IPCE was

$$IPCE = 1240 * \frac{I_s R A_D}{I_D A_D \lambda} \qquad 6.6$$

Where I_s and I_D are the current at the sample and the photodiode at wavelength, λ (in nanometers), R is the responsivity of the photodiode at the specified wavelength, and A_S and A_D are the area of the mercury drop contact and the photodiode. 1240 is a conversion factor that relates the responsivity of the photodiode to its quantum efficiency. It is the wavelength associated with 1 eV of photon energy.

After inserting current data into this equation, a spectra of IPCE was developed for every action spectra. An example of an IPCE spectra is shown in Figure 6.14. The highest IPCE value occurs around the Soret region. For all measurable IPCE spectra for both the bare mercury drop and the hexanethiol drop, the wavelength of maximum IPCE was 447 ± 6.2 nm. Of the six samples and 30 spots tested, the maximum IPCE was about 0.5% in the Soret region. Reported values for the IPCE for bulk heterojunction solar cells incorporating fullerene derivatives have been over 60% in some spectral regions. The IPCE values for these self assembled films is much lower in comparison, but this may still be due to the similar work functions of the ITO and mercury drop.

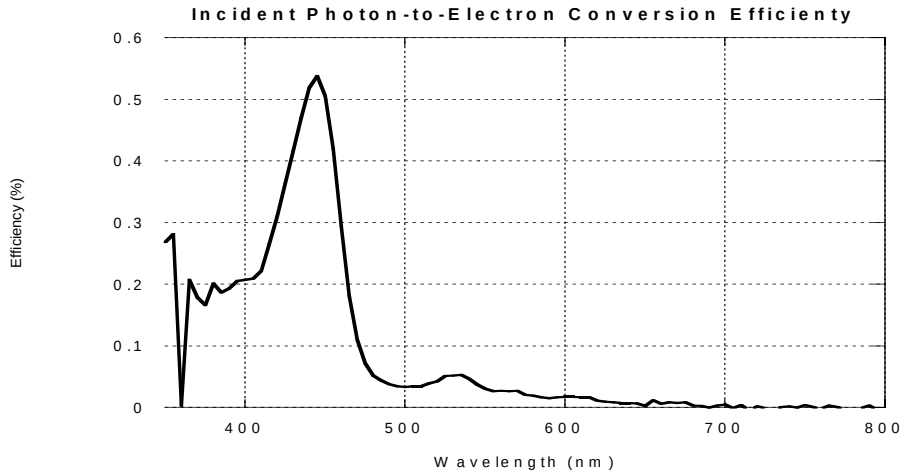

Figure 6.14. Incident photon-to-electron conversion efficiency for dyad thin film and mercury drop electrode.

6.4. Conclusions

The spontaneous formation of the dyad thin films on the ITO after porphyrin protonation is an intriguing feature of these molecules. There is currently quite an ongoing search for suitably cheap and efficient organic materials that can be utilized as active photovoltaic elements, and the potential to have a material assemble on a surface in a beneficial way would be an important breakthrough in organic photovoltaics. For this reason, instrumentation to examine photovoltaic materials is a vital component in understanding the potential benefits of a new material.

There is, unfortunately, very little to say conclusively about the organization of the dyad film on the ITO. Surface characterization techniques are notoriously difficult on ITO, and prove even harder with very thin organic films.

However, the fact that the film only grows in the protonated state indicates that the trifluoroacetate ions are actually a component of the film, as the fully protonated molecule, where the porphyrin is protonated in addition to the pyridine attached to the porphyrin and the amine on the fullerene, would not be prone to aggregating without the presence of counter ions. It may be that the trifluoroacetate ions form a layer on the ITO first, followed by the dyad molecules, and the two species of molecules continue to alternate to form the film. The photovoltaic experiments do not indicate a very ordered film, or photovoltage would be higher due to an accumulated dipole moment.

It is clear from both the AFM results and the calculations of photocurrent efficiencies that the conducting AFM is not the ideal instrument for studying organic photovoltaic materials. The difficulties in working with an AFM cantilever in an illuminating environment are plentiful, from the deflection of the cantilever, to the potential of creating p-n junction devices between the substrate and the tip. Furthermore, based upon photocurrent calculations, the size of the AFM tip is not adequately large enough to be able to detect sizeable photocurrent. It could be possible that with better electronics, the signal to noise ratio could be reduced and the photocurrent detected, but this is beyond the current capabilities of the illuminated SPM system.

The mercury drop instrument, however, proved to be much more suited to determining photovoltaic efficiencies in these dyad films. The size of the mercury contact was much larger than the size of the AFM contact, allowing for

more photocurrent to be obtained. The utilization of a lamp and a monochromator also allowed for the sample to be illuminated in both white light and at very specific wavelengths so the properties of the film could be examined in a spectral manner.

From the mercury drop experiments, it was determined that while the films showed some photovoltaic properties, the photovoltages and overall power were very low. An important factor in achieving reliable photocurrent measurements was the use of a monolayer on the mercury drop. It is believed that this monolayer helps direct current in a specific direction relative to the two electrodes, thus preventing recombination at the mercury interface which could lead to losses in photocurrent efficiency. Despite the increased performance with the hexanethiol, however, the IPCE values were still comparatively low, but this may also be partially due to the similar electrode work functions. Regardless of the low IPCE, though, the films still exhibit novel assembly features with measurable, if not phenomenal, photovoltaic properties.

REFERENCES

1 G. Binnig and H. Rohrer, Helvetica Physica Acta **55** (6), 726 (1982).

2 B. L. Zhang and E. K. Wang, Electrochimica Acta **39** (1), 103 (1994).

3 S. Kerfriden, A. H. Nahle, S. A. Campbell et al., Electrochimica Acta **43** (12-13), 1939 (1998).

4 S.M. Lindsay, *Introduction to Nanoscience*. (Oxford University Press, Oxford, 2010).

5 G. Binnig, C. F. Quate, and C. Gerber, Physical Review Letters **56** (9), 930 (1986).

6 W. H. Han and S. M. Lindsay, Applied Physics Letters **72** (13), 1656 (1998).

7 A. Ebner, F. Kienberger, G. Kada et al., Chemphyschem **6** (5), 897 (2005).

8 L. Lin, H. D. Wang, Y. Liu et al., Biophysical Journal **90** (11), 4236 (2006).

9 T. R. Albrecht, P. Grutter, D. Horne et al., Journal of Applied Physics **69** (2), 668 (1991).

10 Sergei Magonov and John Alexander.

11 T. Trenkler, T. Hantschel, R. Stephenson et al., Journal of Vacuum Science & Technology B **18** (1), 418 (2000).

12 Neil W. Ashcroft and N. David Mermin, *Solid State Physics*. (Thompson Learning, 1976).

13 A. Aviram and M. A. Ratner, Chemical Physics Letters **29** (2), 277 (1974).

14 P. Hohenberg and W. Kohn, Physical Review B **136** (3B), B864 (1964).

15 J. Tomfohr and O. F. Sankey, Journal of Chemical Physics **120** (3), 1542 (2004).

16 F. Evers, F. Weigend, and M. Koentopp, Physical Review B **69** (23) (2004).

17 R. A. Marcus, Journal of Chemical Physics **24** (5), 966 (1956).

18 K. W. Hipps, Science **294** (5542), 536 (2001).

19 H. Park, J. Park, A. K. L. Lim et al., Nature **407** (6800), 57 (2000).

20 W. J. Liang, M. P. Shores, M. Bockrath et al., Nature **417** (6890), 725 (2002).

21 T. Morita and S. Lindsay, Journal of the American Chemical Society **129** (23), 7262 (2007).

22 X. D. Cui, A. Primak, X. Zarate et al., Science **294** (5542), 571 (2001).

23 A. M. Rawlett, T. J. Hopson, L. A. Nagahara et al., Applied Physics Letters **81** (16), 3043 (2002).

24 G. K. Ramachandran, J. K. Tomfohr, J. Li et al., Journal of Physical Chemistry B **107**, 6162 (2003).

25 B. Q. Xu and N. J. J. Tao, Science **301** (5637), 1221 (2003).

26 J. He, O. Sankey, M. Lee et al., Faraday Discussions **131**, 145 (2006).

27 F. Chen, Z. F. Huang, and N. J. Tao, Applied Physics Letters **91** (16) (2007).

28 B. Q. Q. Xu, X. L. L. Li, X. Y. Y. Xiao et al., Nano Letters **5** (7), 1491 (2005).

29 B. Q. Xu, X. Y. Xiao, and N. J. Tao, Journal of the American Chemical Society **125** (52), 16164 (2003).

30 Iris Visoly-Fisher, Kayvon Daie, Yuichi Terazono et al., PNAS **103** (23) (2006).

31 X. Y. Xiao, L. A. Nagahara, A. M. Rawlett et al., Journal of the American Chemical Society **127** (25), 9235 (2005).

32 X. Y. Xiao, B. Q. Xu, and N. J. Tao, Nano Letters **4**, 267 (2004).

33 H. Shpaisman, E. Salomon, G. Nesher et al., Journal of Physical Chemistry C **113** (8), 3313 (2009).

34 A. Salomon, R. Arad-Yellin, A. Shanzer et al., Journal of the American Chemical Society **126**, 11648 (2004).

35 The National Institutes of Health National Human Genome Research Institute, *NHGRI Seeks Next Generation of Sequencing Technologies*, (2004), http://www.genome.gov/12513210.

36 F. Sanger, S. Nicklen, and A. R. Coulson, Proceedings of the National Academy of Sciences of the United States of America **74** (12), 5463 (1977).

37 Paula Yurnakis Bruice, *Organic Chemistry*, 5th ed. (Pearson Prentice Hall, Upper Saddle River, 2007).

38 J. Shendure and H. L. Ji, Nature Biotechnology **26** (10), 1135 (2008).

39 D. Branton, D. W. Deamer, A. Marziali et al., Nature Biotechnology **26** (10), 1146 (2008).

40 J. J. Kasianowicz, E. Brandin, D. Branton et al., Proceedings of the National Academy of Sciences of the United States of America **93** (24), 13770 (1996).

41 M. Akeson, D. Branton, J. J. Kasianowicz et al., Biophysical Journal **77** (6), 3227 (1999).

42 A. Meller, L. Nivon, E. Brandin et al., Proceedings of the National Academy of Sciences of the United States of America **97** (3), 1079 (2000).

43 Author, *The Lindsay Lab: Research Electronic Sequencing by Recognition*, http://www.biodesign.asu.edu/labs/lindsay/research.

44 T. Ohshiro and Y. Umezawa, Proceedings of the National Academy of Sciences of the United States of America **103** (1), 10 (2006).

45 J. He, L. S. Lin, H. Liu et al., Nanotechnology **20** (7) (2009).

46 J. He, L. S. Lin, P. M. Zhang et al., Nano Letters **8** (8), 2530 (2008).

47 S. Chang, J. He, A. Kibel et al., Nature Nanotechnology **4** (5), 297 (2009).

48 Jeffrey L. Hutter and John Bechhoefer, Rev. Sci. Instrum. **64** (7) (1993).

49 Jeffrey L. Hutter, *Calibration of AFM Cantilevers*, (2005), http://www.physics.uwo.ca/~hutter/calibration/afmcal.html.

50 Jacob N. Israelachvili, *Intermolecular and Surface Forces*, 2 ed. (Elsevier Ltd., London, 1985).

51 J. Sponer, P. Jurecka, and P. Hobza, Journal of the American Chemical Society **126** (32), 10142 (2004).

52 J. M. Williams, T. J. Han, and T. P. Beebe, Langmuir **12** (5), 1291 (1996).

53 U.S. Department of Energy, *2008 Solar Technologies Market Report*, January, 2010,

54 U.S. Department of Energy, (June 16, 2010).

55 Thomas Surek and The National Renewable Energy Laboratory, *PROGRESS IN U.S. PHOTOVOLTAICS: LOOKING BACK 30 YEARS AND LOOKING AHEAD 20*, http://www.nrel.gov/pv/thin_film/docs/surek_osaka_talk_final_vgs.pdf

56 Y. Kim, S. Cook, S. M. Tuladhar et al., Nature Materials **5** (3), 197 (2006).

57 J. J. M. Halls, K. Pichler, R. H. Friend et al., Applied Physics Letters **68** (22), 3120 (1996).

58 A. Haugeneder, M. Neges, C. Kallinger et al., Physical Review B **59** (23), 15346 (1999).

59 L. A. A. Pettersson, L. S. Roman, and O. Inganas, Journal of Applied Physics **86** (1), 487 (1999).

60 T. J. Savenije, J. M. Warman, and A. Goossens, Chemical Physics Letters **287** (1-2), 148 (1998).

61 Brian O'Regan and Michael Gratzel, Nature **353**, 737 (1991).

62 M. Gratzel, Journal of Photochemistry and Photobiology a-Chemistry **164** (1-3), 3 (2004).

63 P. Wang, S. M. Zakeeruddin, J. E. Moser et al., Nature Materials **2** (6), 402 (2003).

64 G. Yu, J. Gao, J. C. Hummelen et al., Science **270** (5243), 1789 (1995).

65 F. Padinger, R. S. Rittberger, and N. S. Sariciftci, Advanced Functional Materials **13** (1), 85 (2003).

66 G. Li, V. Shrotriya, J. S. Huang et al., Nature Materials **4** (11), 864 (2005).

67 Jin Young Kim, Kwanghe Lee, Nelson E. Coates et al., Science **317**, 222 (2007).

68 H. Hoppe and N. S. Sariciftci, Journal of Materials Chemistry **16** (1), 45 (2006).

69 W. U. Huynh, J. J. Dittmer, and A. P. Alivisatos, Science **295** (5564), 2425 (2002).

70 M. Law, L. E. Greene, J. C. Johnson et al., Nature Materials **4** (6), 455 (2005).

71 Y. M. Kang, N. G. Park, and D. Kim, Applied Physics Letters **86** (11) (2005).

72 S. Kuhn, U. Hakanson, L. Rogobete et al., Physical Review Letters **97** (1) (2006).

73 F. Tam, G. P. Goodrich, B. R. Johnson et al., Nano Letters **7** (2), 496 (2007).

74 B. P. Rand, P. Peumans, and S. R. Forrest, Journal of Applied Physics **96** (12), 7519 (2004).

75 M. Westphalen, U. Kreibig, J. Rostalski et al., Solar Energy Materials and Solar Cells **61** (1), 97 (2000).

76 D. Kuciauskas, S. Lin, G. R. Seely et al., Journal of Physical Chemistry **100** (39), 15926 (1996).

77 D. Kuciauskas, P. A. Liddell, S. Lin et al., Journal of Physical Chemistry B **104** (18), 4307 (2000).

78 F. Chen, C. Nuckolls, and S. Lindsay, Chemical Physics **324** (1), 236 (2006).

79 S. W. Hahm, H. S. Hwang, D. Kim et al., Electronic Materials Letters **5** (4), 157 (2009).

80 M. Y. Chan, C. S. Lee, S. L. Lai et al., Journal of Applied Physics **100** (9) (2006).

81 D. A. Rider, K. D. Harris, D. Wang et al., Acs Applied Materials & Interfaces **1** (2), 279 (2009).

82 H. B. Michaelson, Journal of Applied Physics **48** (11), 4729 (1977).

83 Y. Park, V. Choong, Y. Gao et al., Applied Physics Letters **68** (19), 2699 (1996).

84 K. Sugiyama, H. Ishii, Y. Ouchi et al., Journal of Applied Physics **87** (1), 295 (2000).

85 Y. J. Liu and H. Z. Yu, Chemphyschem **3** (9), 799 (2002).

APPENDIX A

LABVIEW CODES

All labview codes were written in either Labview 8.2 or Labview 8.5. This appendix covers most of the major programs used in this dissertation work, and includes commented diagrams for the main portions of each code.

Main programming template

Complex labview code can be difficult to write. For this reason, a programming template was utilized for most of the codes. This template allowed for the program to remain idle unless a specific panel was called by a control on the front panel (user interface). The block diagram for this template is shown below.

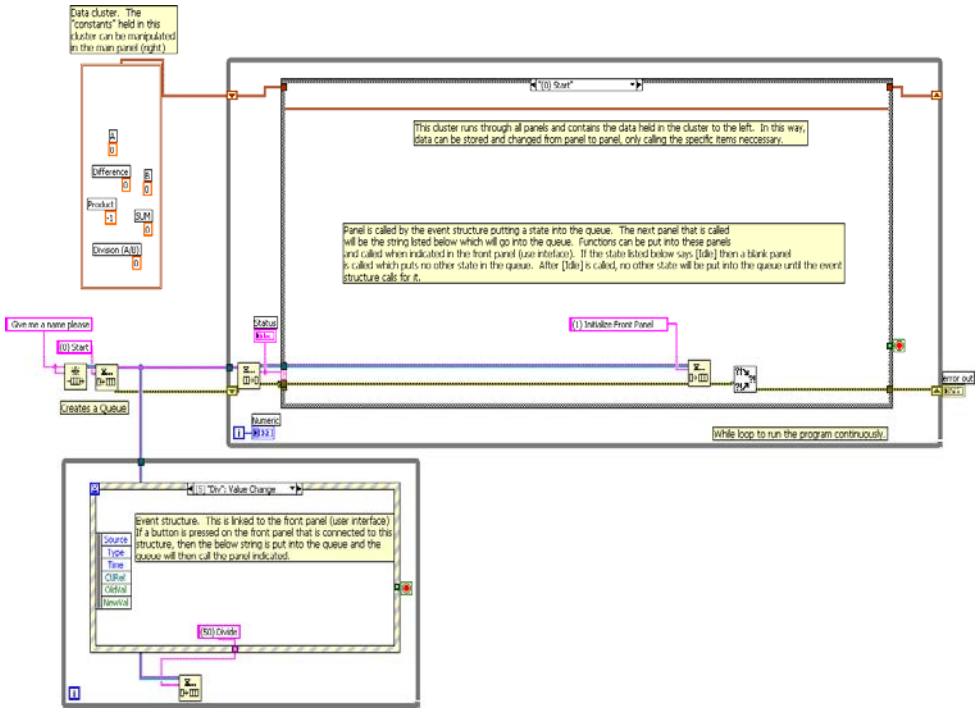

The bottom structure is the event structure which is linked to different controls on the front panel. When one of those controls is changed by the user, the event structure identifies the control and passes a corresponding string up into a queue structure. The string then goes through the queue, where it is de-queued and passed to the main case structure which is held in a while loop. The element then determines which case/state to call. Then, whatever functions are in that state are completed and a new string is put into the queue, directing the program as to which case/state to call next. In the event that there are no further functions to complete, the queue calls an [Idle] case, which puts nothing new into the queue, idling the program until another case is called by the user.

To the left of the program is a data cluster where values can be held. A connection to this cluster is run through all cases/states in the case structure so that data values can be called, manipulated and changed within a case. This is an efficient way of storing data in Labview, and allows for "cleaner" programming code. Data is added to the cluster by simply adding constants to it and naming those constants appropriately to describe what they are in the program. Again, this programming template was utilized for most labview codes.

Base-nucleoside tip withdraw and approach program

The main author of the withdraw and approach program was Shuai Chang. The most relevant cases are included here. The program allows the STM or AFM tip to be controlled at the surface under a setpoint current value. Then, the user

can decide when to withdraw and re-approach the surface. The tip is held at the surface in the programming case shown below.

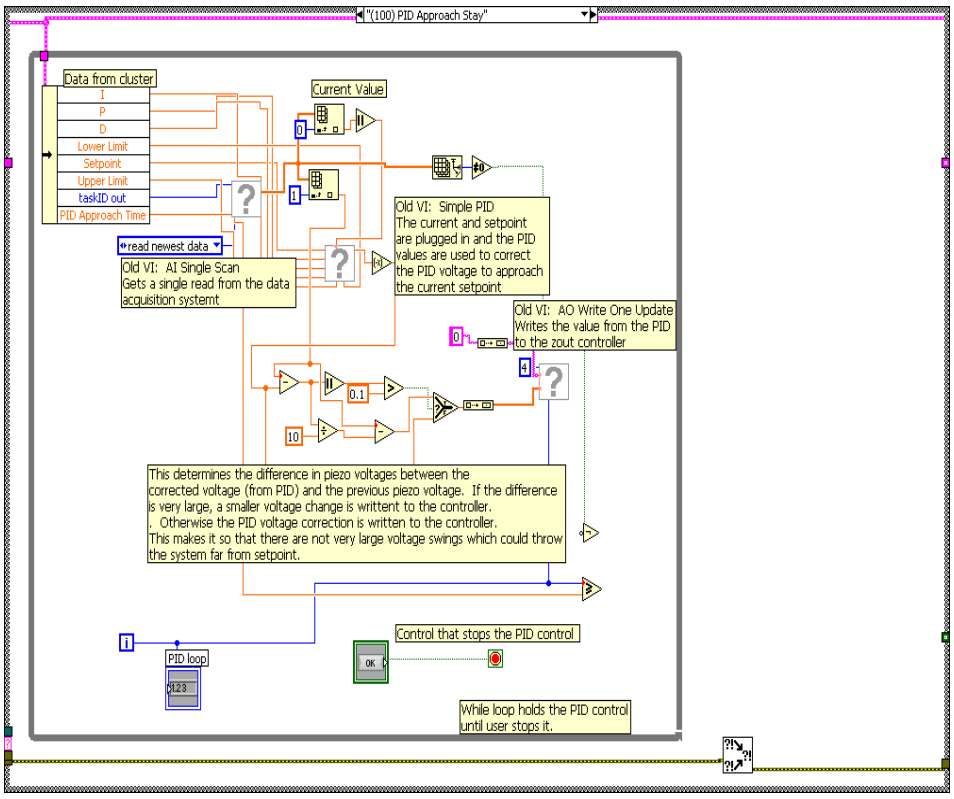

The above program takes a sample of the current and runs it through a PID VI which calculates a piezo voltage correction based upon the setpoint value and the PID values, which are determined by the user. If this correction value is very different than the current piezo voltage, then a smaller difference is written to the piezo controller (which controls the height of the tip). If the difference is small, then the corrected voltage is directly written to the piezo.

Once the user decides to withdraw the tip, the PID loop is broken and the program moves to a new case/state in order to withdraw and re-approach to the surface. That case is shown below.

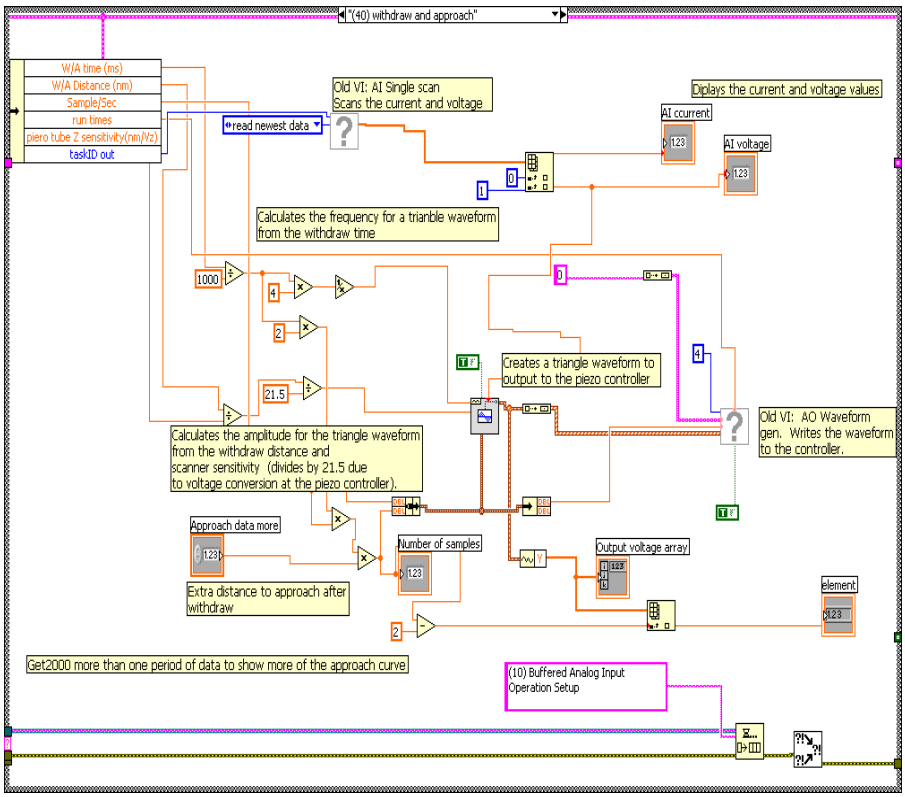

In the above panel, the withdraw time, withdraw distance and scanner sensitivity are used to calculate values (frequency and amplitude) for a triangle waveform to be written to the PZT controller in order to withdraw and approach to the surface. The value for the piezo voltage is obtained and used as a baseline value for the triangle waveform. Once the waveform is written, the program eventually returns to PID control.

AFM tip calibration program

The AFM tip calibration program first acquires a set of data for cantilever deflection at very high sampling rates for a short period of time. Typically, the

program acquires 50,000 samples at a rate of 800,000 samples per second. The program then calculates the power spectral density of the data. This sampling/calculating procedure repeats for a set number of times (typically 150), while compiling the power spectral densities. The diagrams for the cases to acquire the data and calculate the power spectral densities are below.

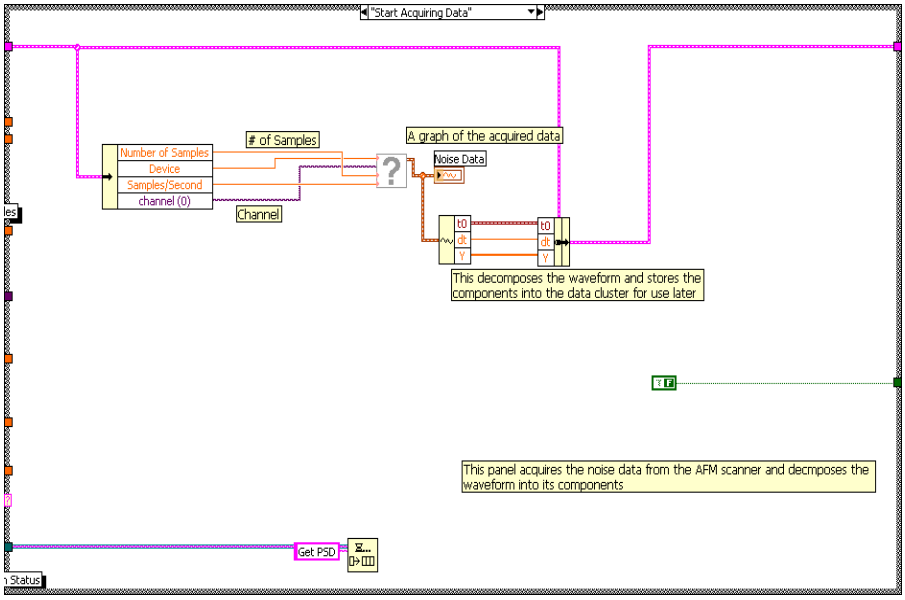

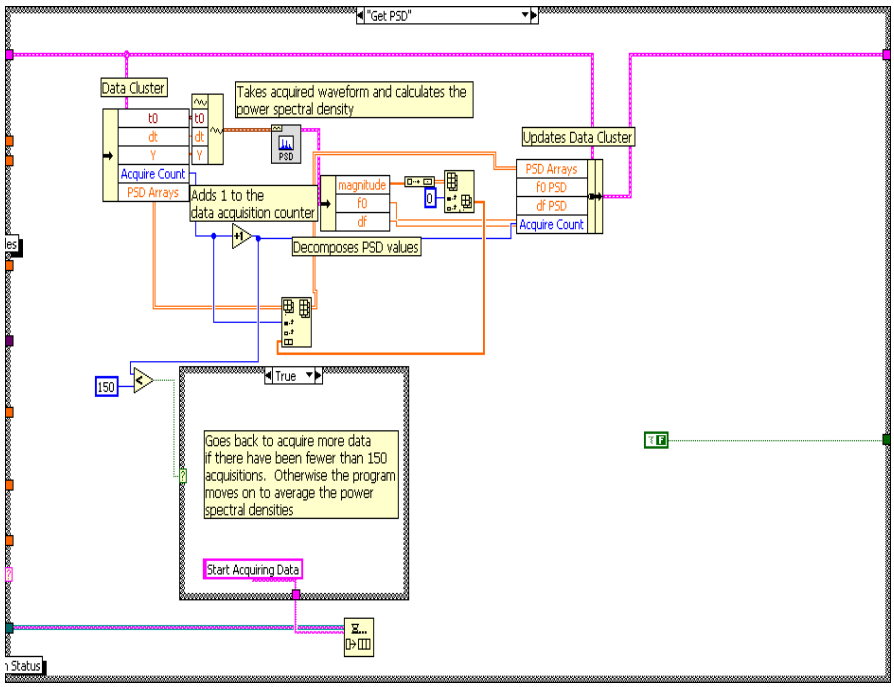

Once the number of acquisitions has been reached, the program then goes on to average all of the power spectral densities that were calculated. The "Average PSD" case repeats for the number of power spectral densities that were calculated. Every time the case is called, it extracts one density value from each of the compiled arrays such that the density values it extracts correspond to the same frequency from each array. It then averages all of the densities at that frequency and, over time, compiles an average power spectral density array giving the average power spectral density at each frequency. In this way, all of the power spectral densities are averaged together. The average power spectral density is then plotted and the program idles. The case for this averaging procedure is shown below.

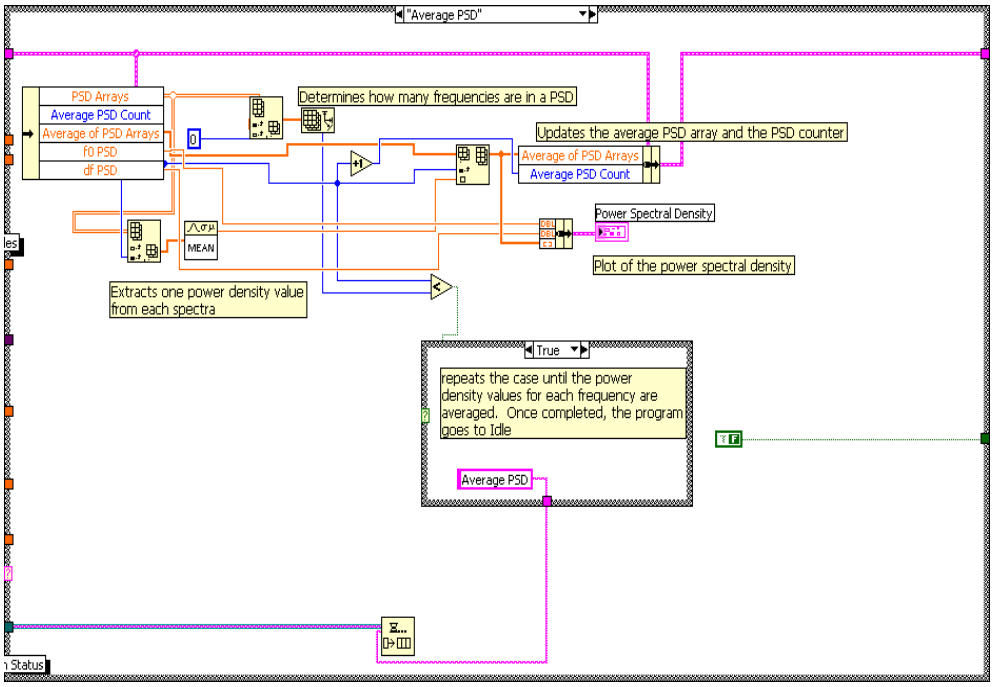

Once the average power spectral density is plotted, the user can search for the resonant peak and input into the program the start and end frequencies for the

peak. The program then can reduce the average power spectral density array to just this peak, and then curve fit the peak to a Lorentzian function. Below shows the case to reduce the power spectral density array to the user specified limits and the case to curve fit the peak to a Lorentzian function. Note that the panel to reduce the power spectral density also numerically calculates the area under the curve for the array in that range. This was done as another way to get the area under the curve, but was not typically utilized in final tip calibrations.

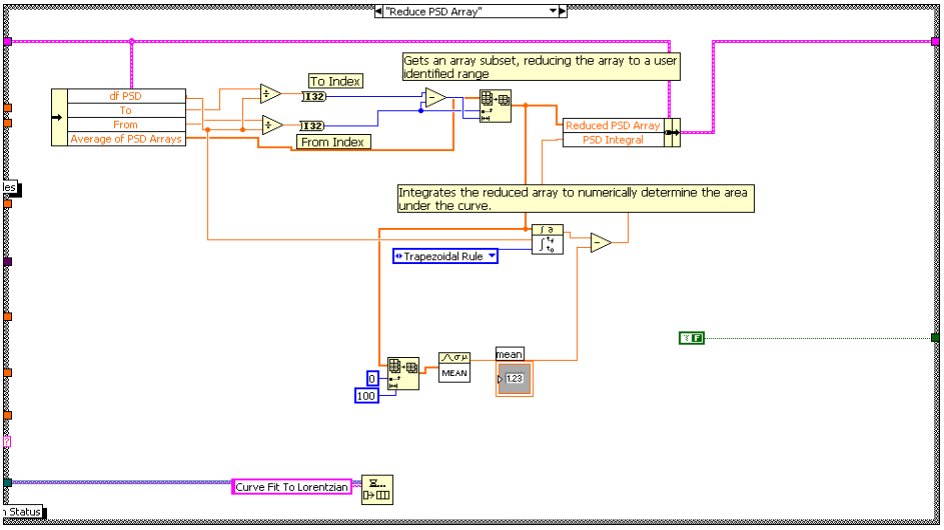

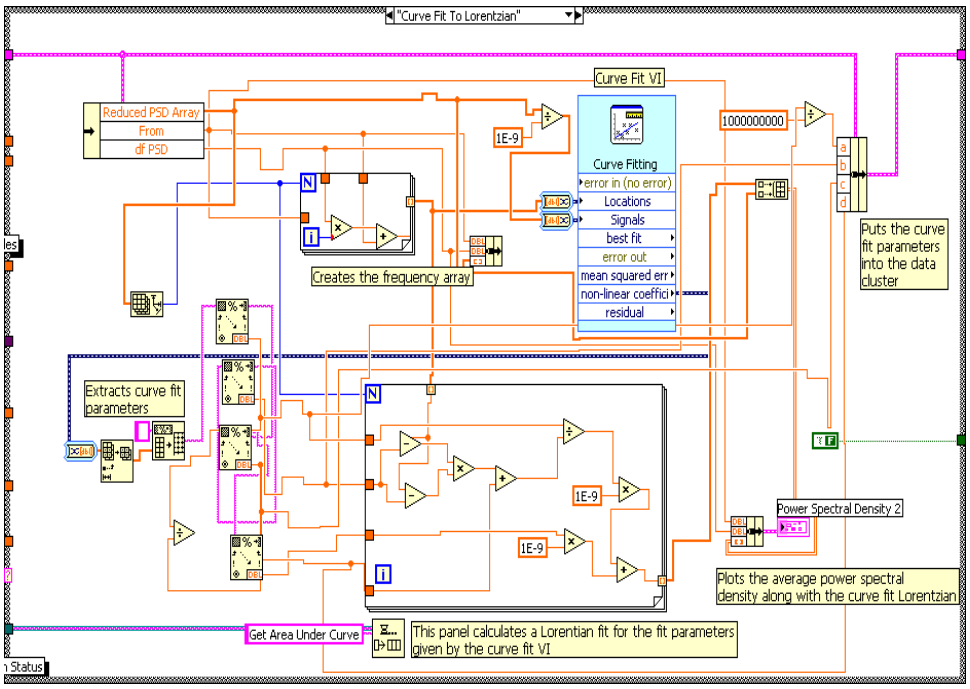

Another case calculates the area under the curve from the curve fit coefficients determined by the curve fit VI. Finally, the user can hit a button to calculate the spring constant. The case that calculates the spring constant from equation 3.1 is below.

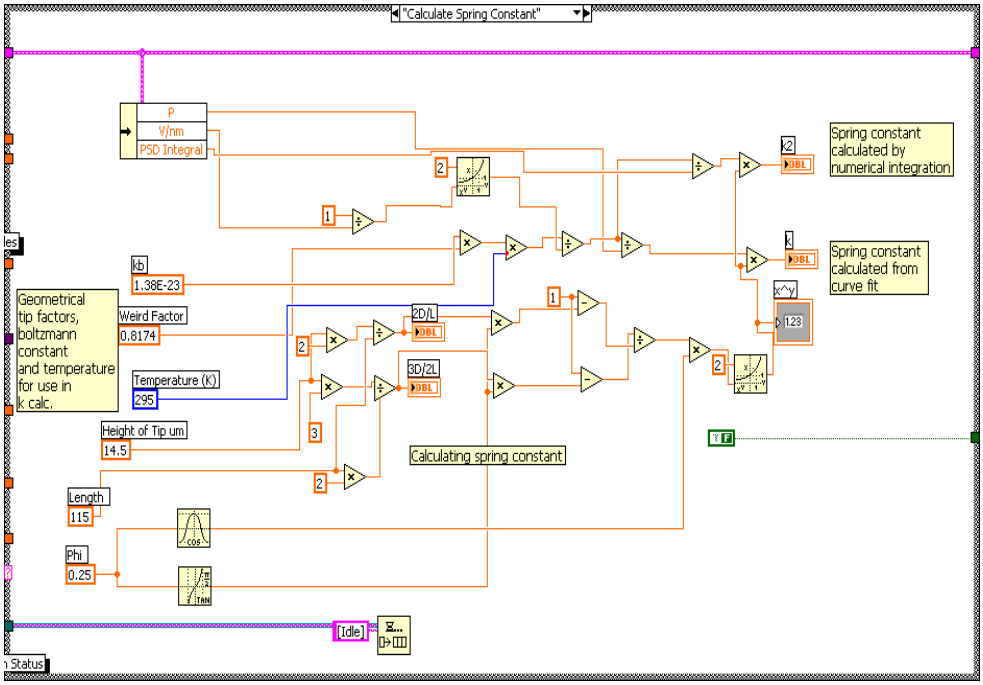

CAFM base-nucleoside data analysis program

The data analysis program for the CAFM DNA base-nucleoside experiment involves multiple steps. The two most important calculations involve calculating the adhesion force of the retraction and calculating the unstretched (F=0) current value. The case that calculates the adhesion force also converts all the deflection values into force values. The user inputs the spring constant and the piezo sensitivity. Another case calculates the retraction distance from the voltage on the piezo and the piezo sensitivity. Once the distance has been calculated the adhesion force can be calculated. The user identifies two points in the deflection contact region (straight line) between which the program finds the slope of the deflection-distance curve. This slope gives the deflection sensitivity of the cantilever in terms of V/nm. The minimum force value is also obtained either manually or automatically, and the deflection at F=0 is input manually by the user. The difference between the deflection at F=0 and the minimum deflection gives the adhesion deflection. This is then converted to force by dividing by the sensitivity to obtain a distance in nanometers and then multiplying by the spring constant to get the force. A similar process was completed on the entire deflection array to convert all the deflection data into force values, which was plotted against distance. The case that calculates all of this is shown below.

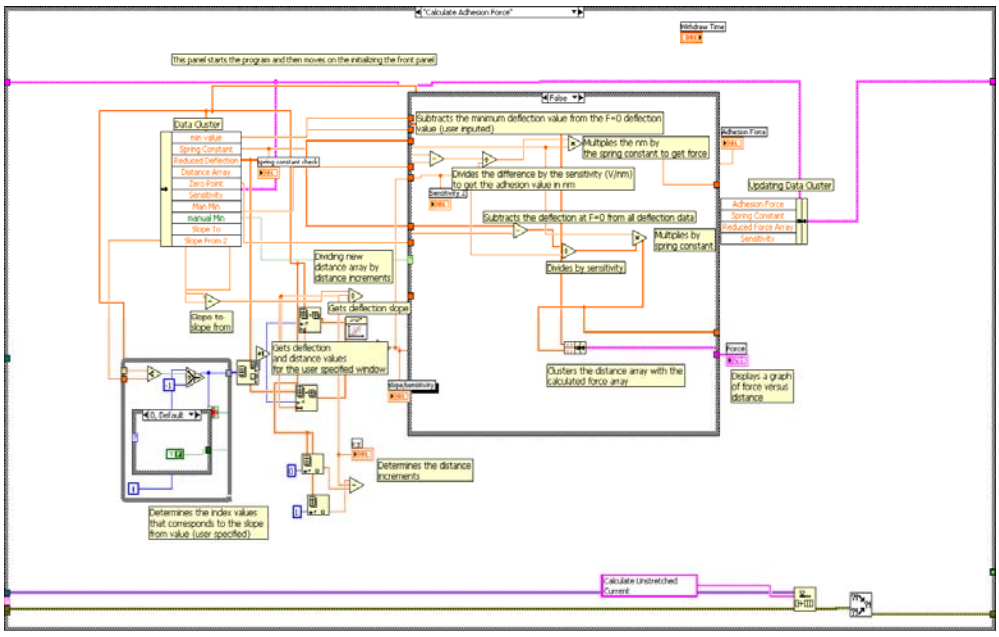

To get the value of the current when F=0, the force array was analyzed to determine the index of the F=0 value. Once this index was determined, it was utilized to extract the current value from the current array. The case that calculates the unstretched current is shown below.

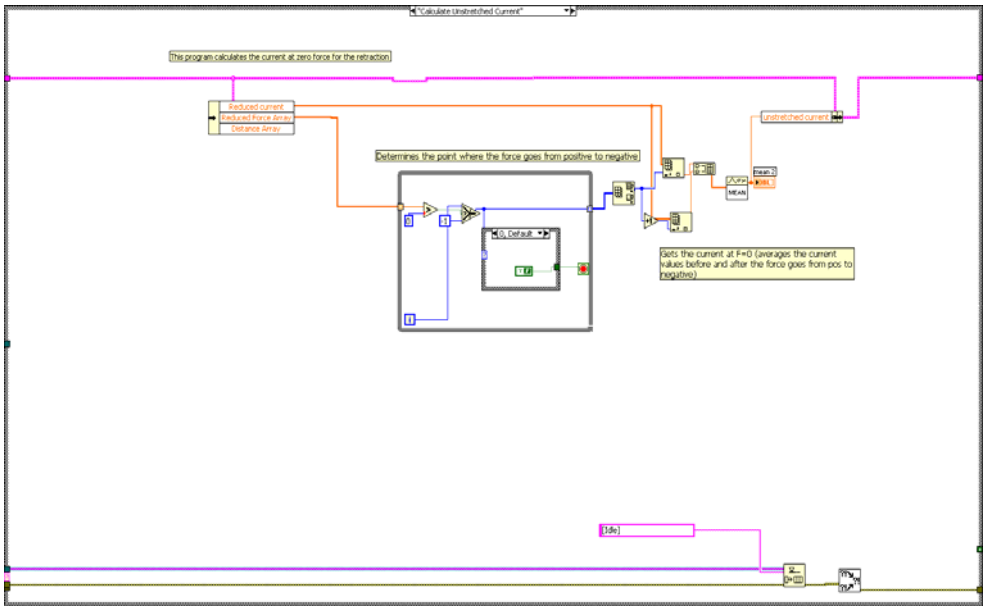

STM break junction experiment

The program to control the tip for the STM break junction experiment has two main components. One case of the program holds the tip under PID control. That case is shown below.

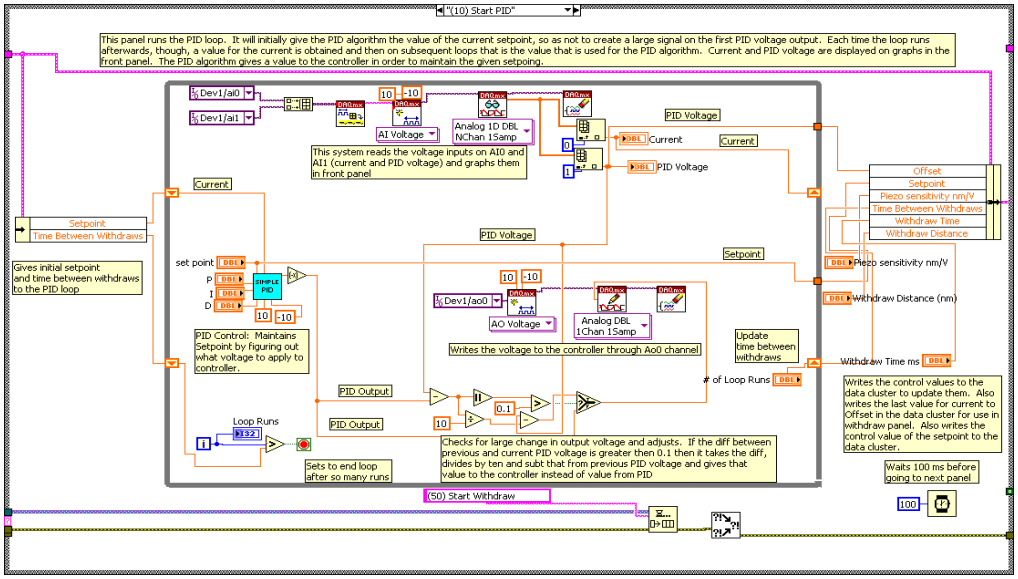

After running the PID loop for a set number of times, the program automatically goes to a case that withdraws and approaches the tip a set distance given a set time. The case that does this is shown below. Like the DNA nucleoside-base program, it utilizes a triangle wave function to produce the withdraw and approach of the STM tip through the scanner piezo voltage and then returns the tip to PID control.

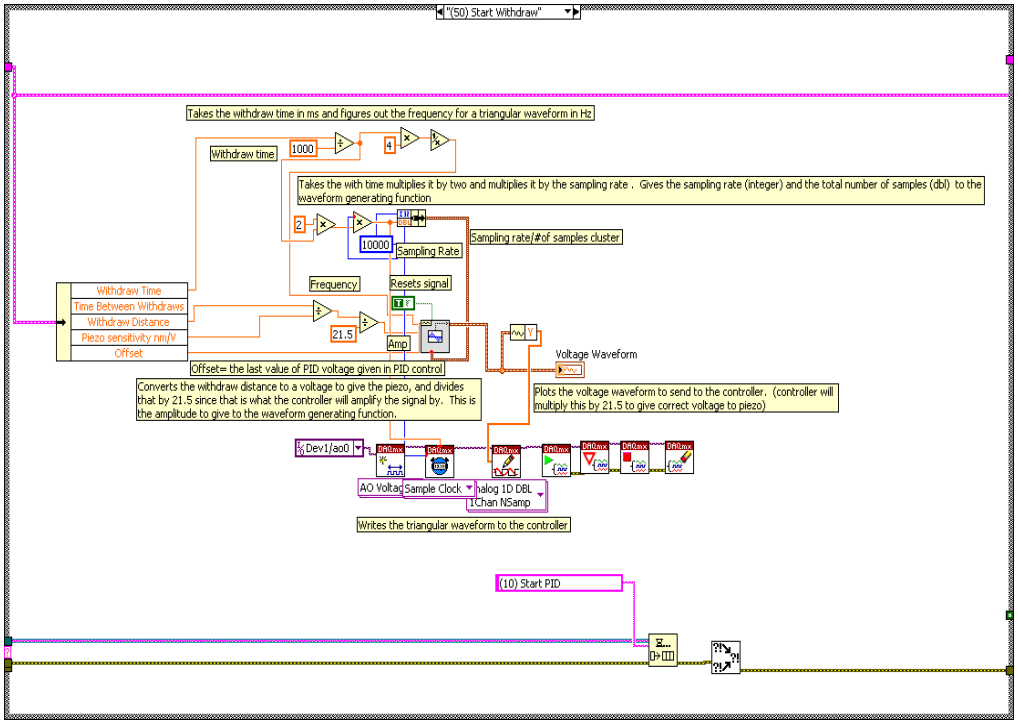

STM break junction data recording

The current withdraw curves, along with the shutter voltage, were recorded on a Tektronix oscilloscope and transferred through a labview program to an open binary file. Another text file recorded the number of points per curve along with the time increment between data points. The oscilloscope came with a labview program that was able to control and record directly from the oscilloscope. The signals were then decomposed and saved into the binary file. The case for this data transfer process is shown below.

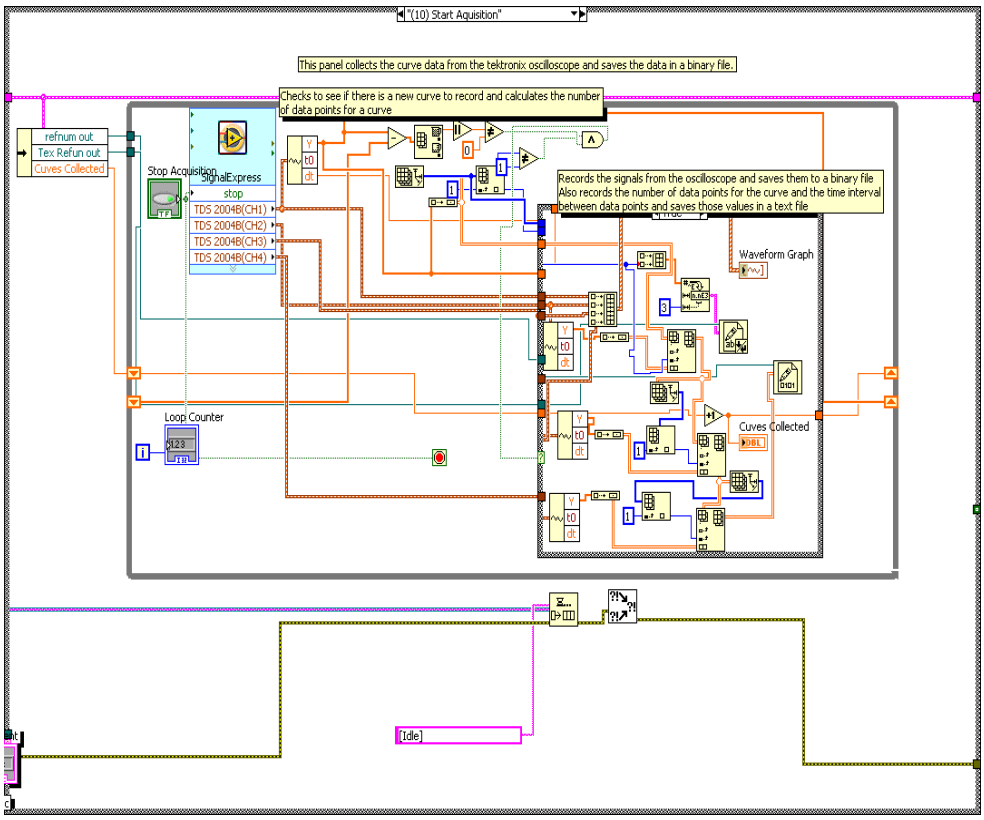

STM break junction "step" analysis

The STM break junction retraction curves were analyzed in order to determine where the current "steps" occurred. A histogram is first made for each curve. The user determines the length of a window to slide over each histogram and the program determines the maximum and minimum values in that window. If the difference between maximum and minimum is above a user controlled threshold, and if the maximum occurs somewhere in the middle of the window (not first or last value), then the current at the maximum is assigned a value of 1. This procedure is applied as the window is slid up the histogram array. The case that creates the single curve histogram and identifies "steps" is shown below.

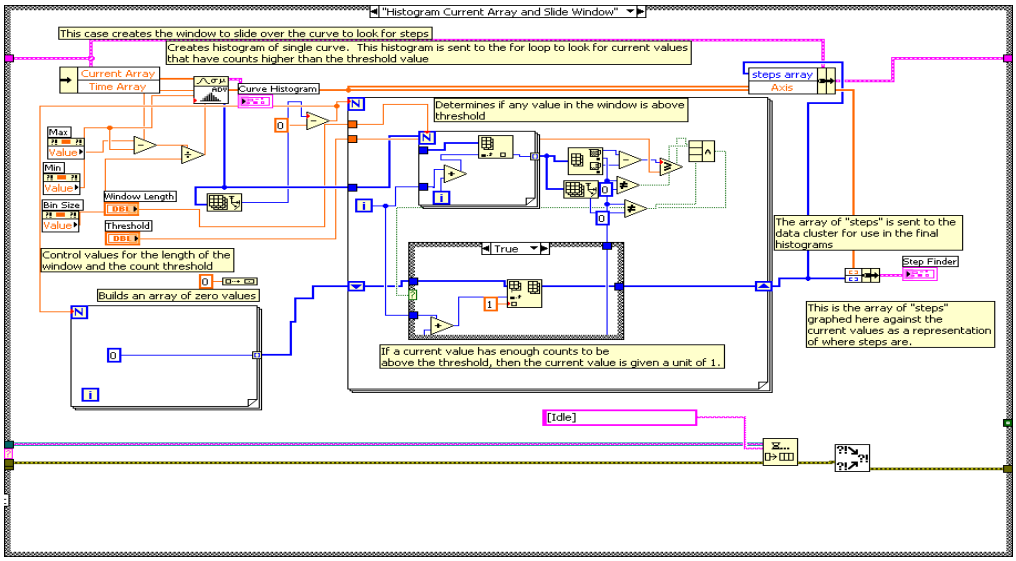

If the user decides to add the steps from a curve to a histogram he/she can tell the program to add the curve. The program then determines whether or not the illuminating laser was on during the particular tip retraction (determined from the voltage on the optical shutter) and then either adds it to the light-on histogram, or adds it to the light-off histogram. The case to add to the compiled light-off histogram is shown below.

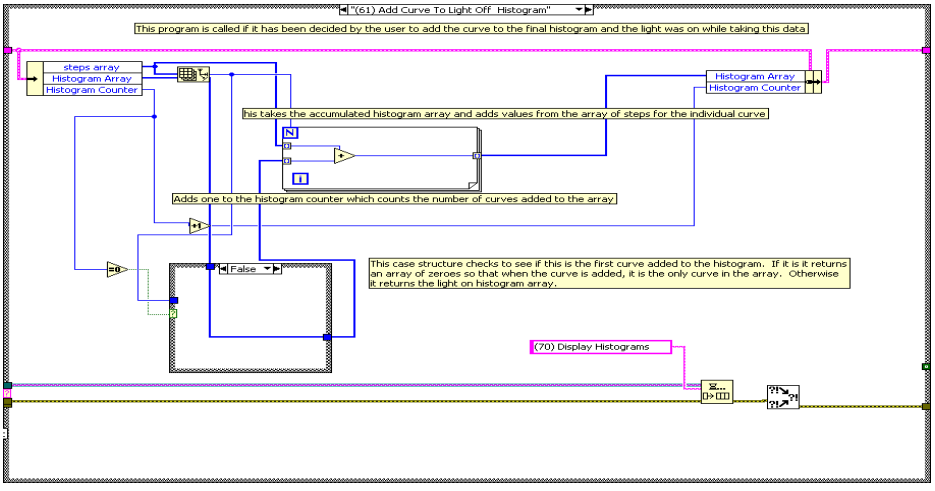

Acquire data for CAFM of dyad thin film program

The program to acquire data from the CAFM to study photocurrent effects in a dyad thin film was relatively simple. The program set up the number of channels to acquire and then acquired data for four channels at a sampling rate set by the user for a given time interval. The interval would repeat and that data would be compiled until the while loop that encompassed the acquisition VI was stopped. The case that acquires the data is below.

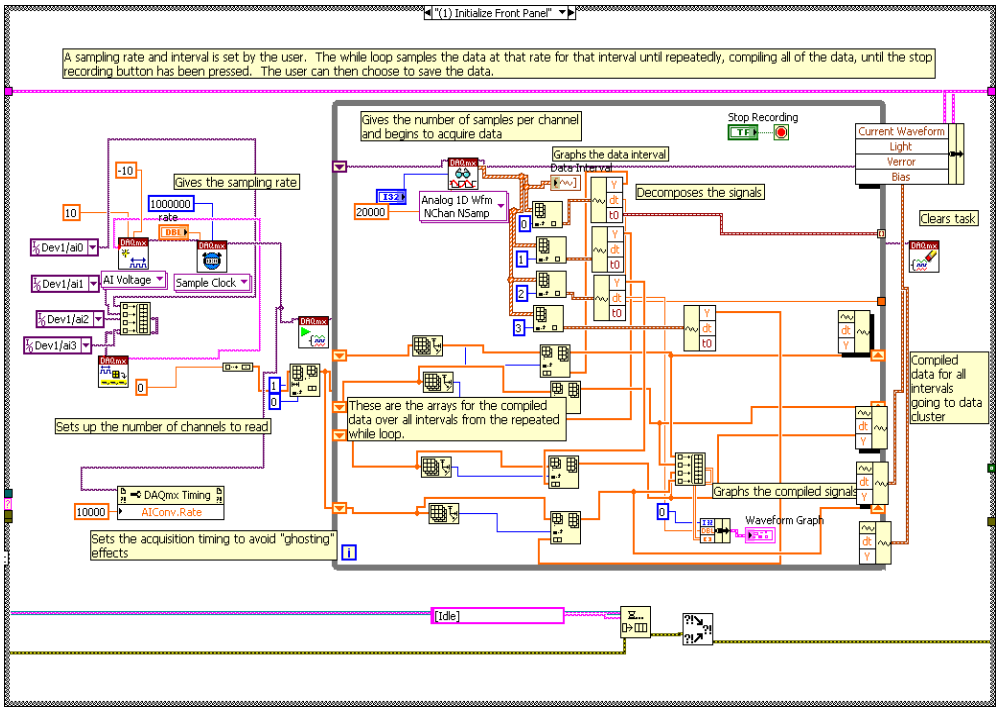

CAFM of dyad thin films data viewing program

The program to view the data acquired from the CAFM of dyad thin films was also relatively straightforward. The file where the data was saved was open

and the array was indexed in order to decompose the different signals. These signals were then graphed against a time axis. These signals changed depending upon what was connected to the data acquisition device, but the first signal was always current. The case that graphs the data is shown below.

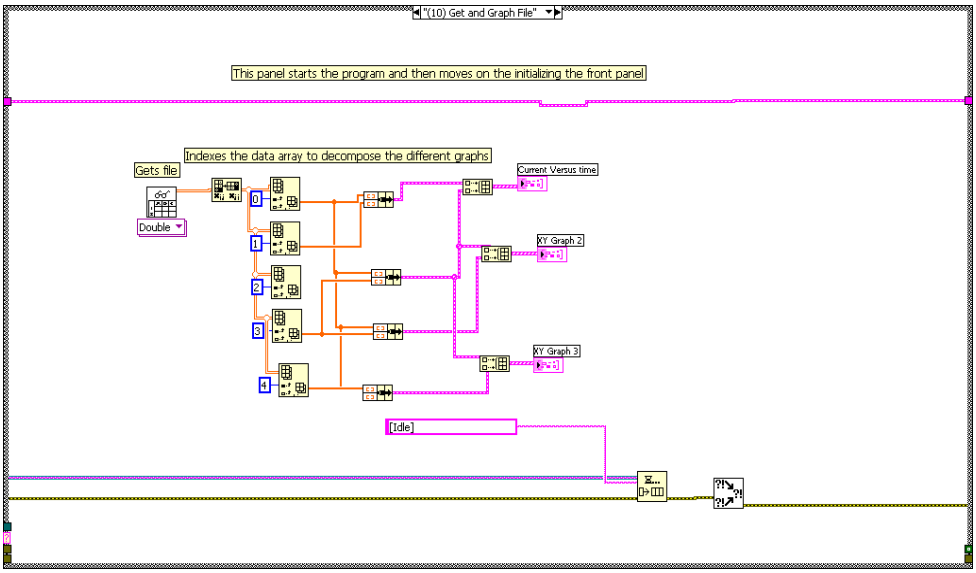

Mercury contact area analysis program

A picture was taken for every mercury contact in the mercury drop electrode experiment on the dyad thin films. A labview program was created in order to determine the size of the contact area. The program takes a picture file and converts it to an intensity graph. There are three cursors on the intensity graph that the user can adjust. The program takes the positions of these three cursors on the intensity graph and fits a circle to those three points, giving the radius of the circle in pixels. For every new mercury drop (not every new contact), the radius of the precision screw was determined through this method

and compared with the actual radius of the precision screw, measured with a micrometer. This radius could be used later to determine actual distances in the image Then pixel radius of every mercury contact was determined by placing the cursors around the edge of the mercury contact circle. The case that created the intensity graph and cursors and the case that calculated the radius of the circle are shown below.

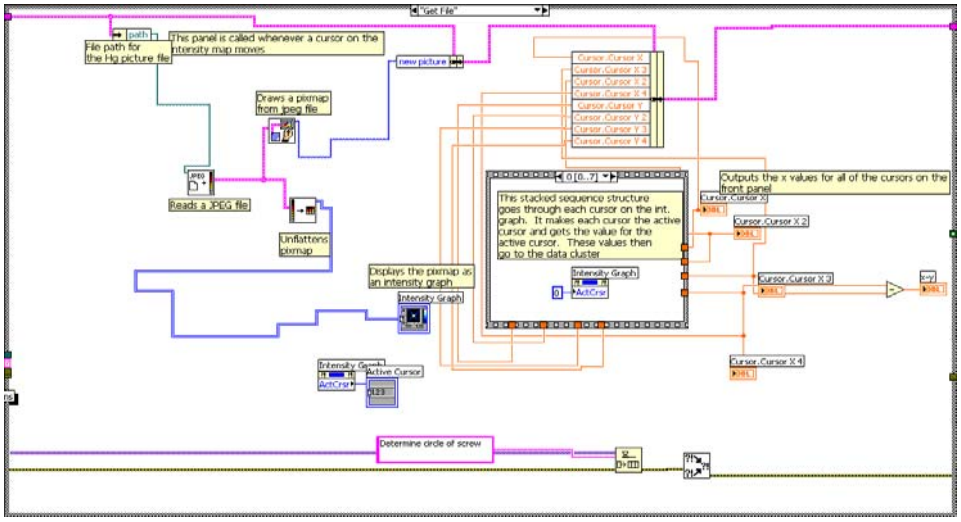

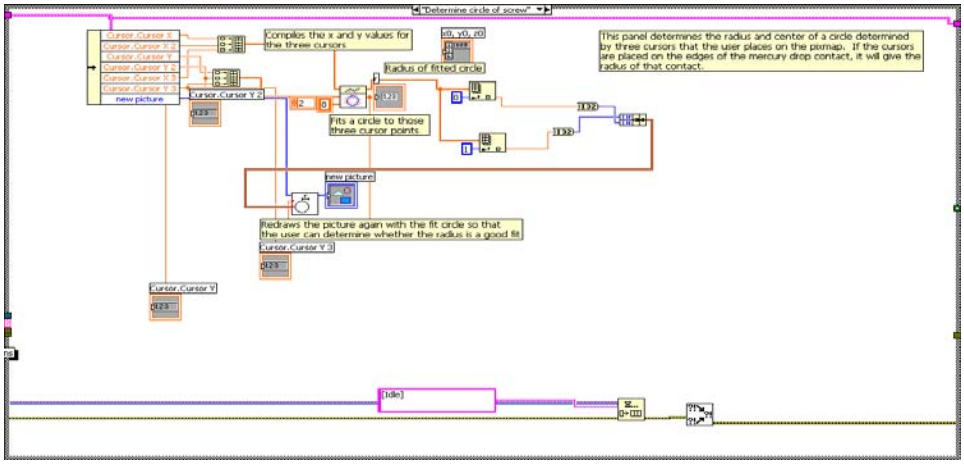

Mercury electrode results analysis program

The data from the mercury drop electrode apparatus was analyzed with another labview program. The user indicates a sample number and a spot number in the front panel of the program. The experimental data was saved in a particular way in order to recognize sample and spot numbers. For example, the photocurrent of sample 3 spot 2 would be saved as s3s2pc.txt. The program then used the sample number and spot number to open all files associated with that sample and spot number. The case that opens the file is shown below.

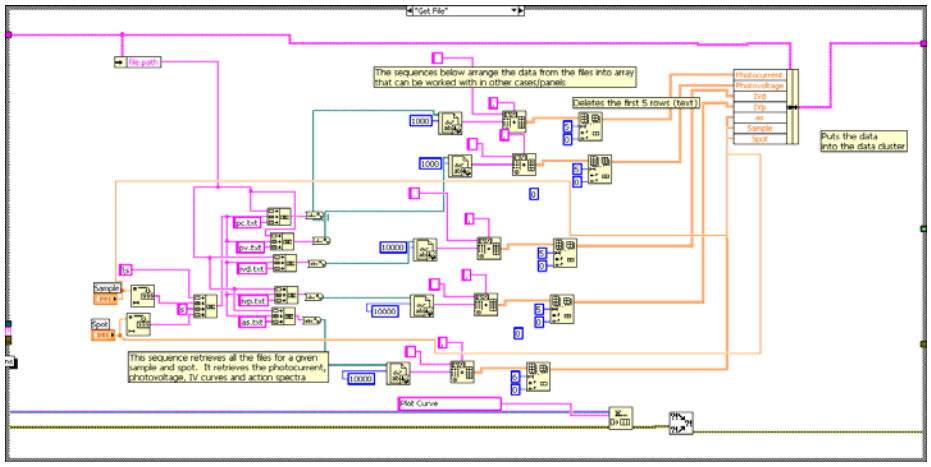

The different measurements were then analyzed. First, the photocurrent was analyzed by determining the difference in current before and after the light was turned on. In the same panel the average dark current was also determined, along with the standard deviation of the dark current. The case that analyzed the photocurrent is shown below. The photovoltage was similarly analyzed.

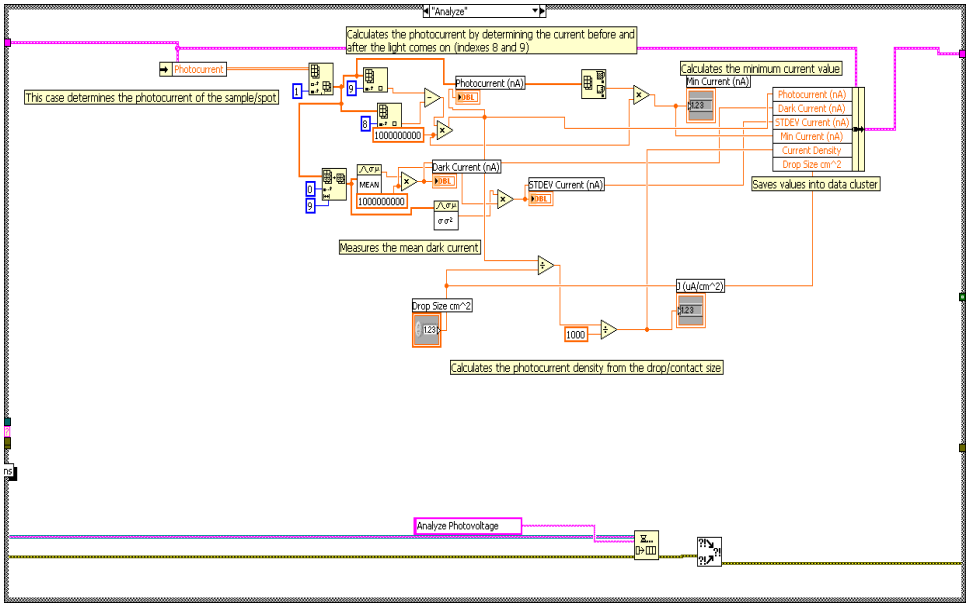

The action spectra was analyzed in a separate case to determine the peak photocurrent and the wavelength of the peak photocurrent. In another case, the IV curves were analyzed by determining the current values from 0 to 0.05 V. The conductivity was found by taking a linear fit to the values. Both the dark conductivity and the light conductivity were determined in this way. In the same case, the responsivity data for the photodiode, which was saved in a separate text file, was converted into a numeric array. This case is shown below.

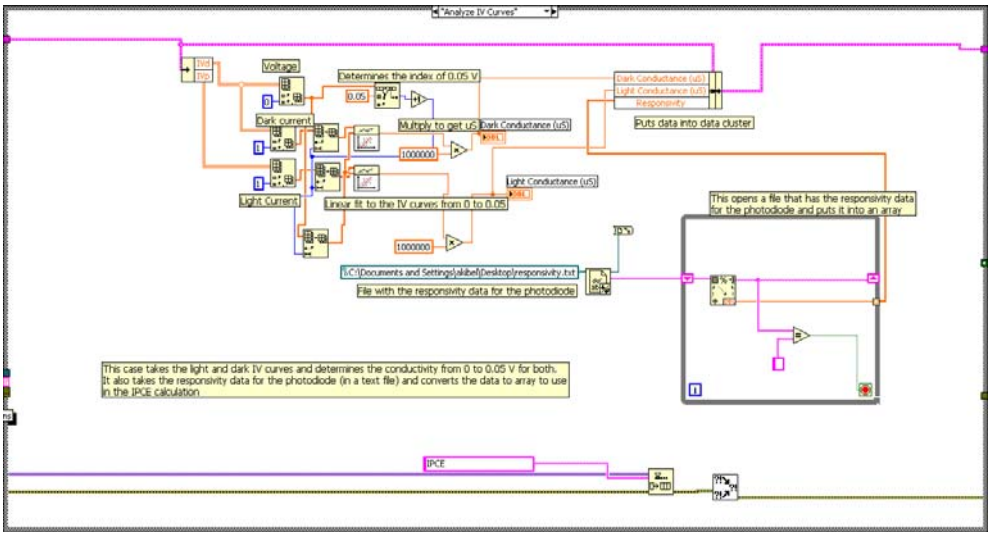

Finally, the IPCE was determined from the action spectra of the sample, the action spectra of the photodiode (opened and transferred to an array in another case) and the responsivity data. The responsivity values are given for every 10 nm of optical wavelength, whereas the action spectra values are every 5 nm. So values for the responsivity were interpolated to create an array of responsivity values for every 5 nm. Using equation 6.6, the IPCE is calculated in the case below.